



seit 1558

Friedrich-Schiller-Universität Jena

Physikalisch-Astronomischen Fakultät

**High-contrast Laser-driven Monoenergetic Proton Beams
and
Near-critical Density Plasma Diagnosis**

Ph.D. Dissertation

Mingyuan Shi

eingereicht von Dipl.-Phys. Mingyuan Shi

geboren am 03.03.1990 in Lanzhou, Gansu, China

Gutachter:

1. Prof. Dr. Matt Zepf

Physikalisch-Astronomische Fakultät
Friedrich-Schiller-Universität Jena &
Helmholtz-Institut Jena, Deutschland

2. Prof. Dr. Jörg Schreiber

Fakultät für Physik
Ludwig-Maximilians-Universität München &
Max-Planck-Institut für Quantenoptik, Deutschland

3. Prof. Dr. Jianhui Bin

Universität der Chinesischen Akademie der Wissenschaften &
Shanghai Institut für Optik und Feinmechanik, China

Dissertation

Friedrich-Schiller-Universität Jena

Tag der öffentlichen Verteidigung: 20.07.2023

Zusammenfassung

Mit der rapiden Entwicklung der Ultraintensitätslaser-Technologie hat die Laserleistung bereits das Petawatt-Niveau erreicht, und die Intensität hat sich auf 10^{22}W/cm^2 stark erhöht. Materie unter hochintensiven Laserfeldern zeigt zahlreiche attraktive Phänomene und bietet viele potenzielle Anwendungen. Als eine wesentliche Zweigstelle der Laser-Materie-Wechselwirkungen hat die Laserpartikelbeschleunigung zunehmend Aufmerksamkeit erregt. Aktuell können Protonenbeschleunigungsexperimente auf Basis von Petawatt-Lasersystemen einen Strahl von nahezu 100 MeV erzeugen. Allerdings bestehen nach wie vor signifikante Diskrepanzen zwischen Simulation und tatsächlichen experimentellen Ergebnissen. Des Weiteren unterscheiden sich selbst bei ähnlichen Lasersystemen und demselben Beschleunigungsmechanismus die experimentellen Ergebnisse in Laboren auf der ganzen Welt erheblich. Der grundlegende Grund dafür ist, dass feste Ziele sehr strenge Anforderungen an den Laserkontrast haben, um eine signifikante Ausdehnung zu vermeiden. Die Laserpartikelbeschleunigung verwendet ein dünnes Ziel mit einer Dicke von Mikrometern oder Nanometern, und der schwächere Vorimpuls an der Vorderseite des Hauptimpulses ionisiert das dünne Ziel schnell. Die anschließende Ausdehnung des Plasmas führt zu mehrdimensionalen Veränderungen in seiner maximalen Dichte und sogar seiner räumlichen Verteilung, was zu einer erheblichen Abweichung zwischen den experimentellen und simulierten Bedingungen führt. Die Dissertation beschreibt hauptsächlich die Wechselwirkung eines ultrahochintensiven Laserpulses mit Zielen nahe der Feststoffdichte. Der grundlegende physikalische Prozess, der der Beschleunigung von Protonen in starken Laserfeldern zugrunde liegt, wird durch zahlreiche Particle-in-Cell (PIC)-Simulationen analysiert. Jedoch bleiben Laserwechselwirkungen mit Mikrometerskala und nahezu kritischer Dichte herausfordernd für externe Untersuchungen. Um dieses Problem zu lösen, wird ein Mehrfarbenlaser als Probelicht eingeführt, μm die Entwicklung des dichten Plasmas, verursacht durch den Vorimpuls, mit dem vorherigen numerischen Modell zu messen und zu vergleichen.

In dieser Arbeit wird das Experiment am Jenaer Titanium: Sapphire 200 Terawatt Laser System (JETi200) durchgeführt, das sich in Jena, Deutschland, befindet. Mit seiner ausgezeichneten zeitlichen Kontrasteigenschaft kann das wenige Nanometer dicke freistehende Ziel einige Pikosekunden lang im festen Zustand verbleiben, bevor

der Hauptpeak eintrifft, wodurch die Ausdehnung des Ziels erheblich reduziert wird. Die resultierenden Protonenstrahlen zeigen charakteristische Merkmale hinsichtlich der Cut-off-Energie und der Verteilung des Energiespektrums. Die Protonenstrahlen im präsentierten Experiment zeigen einen mehr als 30 MeV monochromatischen Peak unter dem zirkular polarisierten Laser und die höchste Spitzenpartikelkinetikenergie pro Joule Laserenergie von etwa 20 MeV/J. Im Gegensatz zum zirkular polarisierten Anregungslaser zeigt die Cut-off-Energie bei Bestrahlung mit linear polarisiertem Licht eine schwache Abhängigkeit von der Dicke des Ziels. Darüber hinaus zeigt die Implementierung einer Transmissionlichtdiagnostik im Experiment, dass das Transmissionlicht des Hauptimpulses deutlich schwächer ist als in anderen ähnlichen Experimenten. Die Energie und das Energiespektrum der Protonen belegen, dass es möglich ist, In-vivo-Forschung und Protonenhauttherapie mit dem Laser auf Terawatt-Niveau durchzuführen.

Der Laserkontrast hat einen erheblichen Einfluss auf die Laserionenbeschleunigung, da ein niedriger Kontrast zu einer vorzeitigen Ausdehnung von dünnen Zielen führen kann. Die Entwicklung der vorzeitigen Ausdehnung, verursacht durch Vorimpulse, basiert hauptsächlich auf numerischen Berechnungen und Forschung. In dieser Arbeit führe ich jedoch eine umfassende experimentelle Untersuchung der Vorimpuls-induzierten Vorplasmarevolution durch, einschließlich der Messung der Zeit der Vorplasmarevolution und des Vergleichs mit vorherigen numerischen Modellen. Diese Untersuchung ist insbesondere für die neueste Generation von Laserionenbeschleunigern von Vorteil, da sie die genaue Quantifizierung der zeitlichen Kontrastanforderungen in der Ära der Petawatt-Laserantriebe ermöglicht.

Zusätzlich wurde eine ultradünne Zielherstellung- und Charakterisierungsplattform am Helmholtz Jena eingerichtet. Das Labor hat erfolgreich ultradünne Formvar-Ziele im Bereich von 8 nm bis 400 nm für lasergetriebene Teilchenbeschleunigung bereitgestellt. Die Eigenschaften und Parameter des Ziels werden im Detail untersucht, einschließlich der Messung der Schadensschwelle in Nanosekundenlaserfeldern für diese ultradünnen Ziele.

Bei einem Laser-System treten in der Regel unerwünschte Beugungseffekte während der Übertragung des Laserstrahls über lange Entfernungen und im Prozess der

Strahlentrennung auf, die die Fokusqualität beeinträchtigen und sogar das Verstärkungssystem schädigen können. Um dieses Problem zu lösen, wurde für das JETi200-System eine Reihe von gezahnten Blenden entwickelt, einschließlich unterschiedlicher Blendenformen und entsprechender Simulationen. Das gesamte Setup wurde bereits im Frontend des JETi200 installiert und kann in zukünftigen komplexen Mehrstrahl-Laserexperimenten hilfreich sein.

Abstract

With the rapid development of ultra-intensity laser technology, laser power has already reached the petawatt level, and the intensity has greatly increased to $10^{22}\text{W}/\text{cm}^2$. Matter under highly intense laser fields exhibits numerous attractive phenomena and offers many potential applications. As an essential branch of laser-matter interactions, laser particle acceleration has drawn increasing attention. Currently, proton acceleration experiments based on petawatt laser systems can generate a beam of nearly 100 MeV. However, significant discrepancies still exist between simulation and actual experimental results. Furthermore, even with similar laser systems and the same acceleration mechanism, experimental results in laboratories around the world still differ quite substantially. The fundamental reason is that solid targets have very strict requirements for laser contrast to avoid significant pre-expansion. Laser particle acceleration uses a thin target with a thickness of microns or nanometers. Even the weaker pre-pulse at the leading edge of the main pulse could quickly ionize the thin target. Subsequent plasma expansion induces multidimensional changes in its maximum density and even its spatial distribution, which leads to a significant difference between the experimental and simulated conditions. The dissertation mainly describes the interaction of an ultrahigh-intensity laser pulse with near-solid density targets. The fundamental physics process underlying the acceleration of protons in strong laser fields is analysed through numerous Particle-in-Cell (PIC) simulations. Furthermore, laser interactions with micron-scale, near-critical density plasmas remain challenging for external probing. To address this issue, a multi-colour laser is introduced as the probe light to measure and compare the evolution of the dense plasma caused by the pre-pulse with the previous numerical model.

In this dissertation, the experiments are conducted at the Jenaer Titanium: Sapphire 200 Terawatt Laser System (JETi200) located in Jena, Germany. With its excellent temporal contrast, the few-nanometer freestanding target can remain in a solid state for a few picoseconds before the main pulse arrives, greatly reducing the pre-expansion of the target. The resulting proton beams exhibit distinctive features in terms of cut-off energy and energy spectrum distribution. The proton beams in the presented experiment show a more than 30 MeV monoenergetic peak

under the circularly polarized laser, and the highest peak particle kinetic energy per Joule of laser energy is around $\sim 20\text{MeV}/\text{J}$. As opposed to the circularly polarized driving light, the cut-off energy shows weak dependence on the target thickness when irradiated with linearly polarized light. Moreover, the implementation of a transmission light diagnostic in the experiment indicates that the transmission light of the main pulse is significantly weaker than that in other similar experiments. The energy and energy spectrum of the protons provide the potential to conduct in vivo research and proton skin therapy using the Terawatt-level laser system.

Laser contrast significantly impacts laser-driven ion acceleration, as low contrast can lead to premature expansion of thin targets. The evolution of premature expansion, caused by pre-pulses, is primarily based on numerical calculations research. However, in this paper, I conduct a comprehensive experimental study of pre-pulse-induced pre-plasma evolution, including the measurement of pre-plasma evolution time and comparison with a previous numerical model. This investigation is especially beneficial for the latest generation of laser ion accelerators, as it enables the precise quantification of temporal contrast requirements in the Petawatt laser driver era.

In addition, an ultra-thin target fabrication and characterization platform has been established in Helmholtz Jena. The lab has successfully provided ultra-thin formvar targets ranging from 8 nm to 400 nm for laser-driven particle acceleration. The characteristics and parameters of the target are studied in detail, including the measurement of the damage threshold in nanosecond laser fields for these ultra-thin targets.

For a laser system, unwanted diffraction effects typically occur during long-distance laser beam transmission and the process of beam splitting, which can affect the focus quality and even harm the amplification system. To address this issue, a set of serrated apertures has been designed for the JETi200 system, including different aperture shapes and corresponding simulations. The whole setup has already been installed in the front end of the JETi200 and can be helpful in future complex multi-beam laser experiments.

Contents

1	Introduction and Motivation	1
2	Theoretical Background	5
2.1	Ultrashort Laser Pulses	5
2.2	Laser Interaction with Single Atoms	8
2.2.1	Multi-Photon Ionization (MPI)	8
2.2.2	Above-Threshold Ionization (ATI)	9
2.2.3	Tunneling Ionization (TI)	9
2.2.4	Barrier Suppression Ionization (BSI)	10
2.3	Laser-single Electron Interactions	11
2.3.1	Non-relativistic Regime	12
2.3.2	Relativistic Regime	14
2.4	Fundamentals of Plasma and Plasma Diagnosis	16
2.4.1	General Properties of Plasmas	16
2.4.2	Plasma Diagnostic Methods	18
2.5	Laser Plasma Acceleration Mechanisms	20
2.5.1	Target Normal Sheath Acceleration (TNSA)	20
2.5.2	Radiation Pressure Acceleration (RPA)	24
2.5.3	Relativistic Induced Transparency (RIT)	28
2.5.4	Coulomb Explosion Acceleration (CEA)	29
2.6	Enhanced Particle Acceleration Schemes	30
2.6.1	Optical Methods	30
2.6.2	Novel Target Methods	31
3	Experimental Description and Diagnostics	33
3.1	JETi200 Laser System	33
3.1.1	Laser Contrast	34
3.1.2	Plasma Mirror Energy Efficiency	37

3.2	Q-Smart Laser System	38
3.3	Diagnostic System	39
3.3.1	Streak Camera	39
3.3.2	Magnetic Spectrometer Design	41
3.4	Serrated Aperture Design	44
3.4.1	Simulation	45
3.4.2	Experiment	47
3.5	Summary	50
4	Ultra-thin Target Fabrication	51
4.1	Spin-coating Method	52
4.2	Characterisation of Thin Film	54
4.2.1	Thickness Measurement	54
4.2.2	Mass Concentration	54
4.2.3	The Effect of Rotation Speed	56
4.2.4	Thickness Fluctuation	56
4.2.5	Storage	57
4.3	Laser-induced Damage Threshold	58
4.4	Summary	60
5	Proton Acceleration with High Contrast Laser Pulses	61
5.1	Experimental setup	61
5.2	Proton Acceleration Based on Solid Targets	62
5.2.1	Target Thickness Effect in Proton Acceleration	62
5.2.2	Proton Energy Spectrum	65
5.2.3	Proton Energy Scaling	67
5.3	EPOCH 2D Simulation	67
5.3.1	Multi-species Target Parameters	68
5.3.2	Accelerating Electric Field and Ion Spatial Distribution	69
5.3.3	Divergence of Protons	72
5.3.4	Phase Space Distribution of Protons	73
5.3.5	Proton Energy over Time	74
5.4	Summary	76
6	Near-Critical Density Plasma Diagnosis	77
6.1	Numerical Calculation of Probe Light Transmittance	77

6.1.1	Theory	77
6.1.2	Non-uniform Plasma Density Profile	81
6.1.3	Probing Light Transmission in Near Critical Density Plasmas	82
6.2	Experiment	85
6.2.1	Experimental Setup	85
6.2.2	Experimental Results	86
6.2.3	Comparison of Experimental Results with Numerical Model	89
6.3	Summary	92
7	Summary Outlook	93
7.1	Summary	93
7.2	Outlook	95
	Bibliography	97
	Appendix: Multi-stage AI Filter	117
	Appendix Raw Proton Spectrum	119
	Appendix: Helmholtz and Fresnel equations	121
	Publications by the Author	125
	Acknowledgement	127
	Ehrenwörtliche Erklärung	131

Introduction and Motivation

” *What you learn from a life in science is the vastness of our ignorance.*

— David Eagleman

Over the past 30 years, laser-related research fields have witnessed remarkable development. In particular, the invention of chirped pulse amplification (CPA) technology in 1985 has greatly improved the focused intensity while reducing pulse duration to the femtosecond range and miniaturizing the laser system. The ultra-short pulse produced in extreme conditions benefits numerous and diverse fields, including laser physics, plasma physics, atomic and molecular physics, particle physics, biochemistry, and more. The continuous iteration of laser pulses to be shorter and stronger, like a key, has aroused the interest of scientific researchers and opened up a variety of physical phenomena. New laser-based technologies have become more and more mature. For non-relativistic ultra-short lasers, the laser field is already comparable to the external electric field of the atom, and the outer electrons start to oscillate with an amplitude of many Bohr radii under the laser field. With the reversal of the electric field, these electrons will be sent back to their parent ion, resulting in the emission of a single, high-frequency photon known as gas high harmonic generation (GHHG). In relativistic laser fields, electrons can be accelerated to relativistic velocities in just a few optical cycles, and the response of the electron provokes more physical phenomena. An LWFA-based free electron laser experiment constitutes a proof-of-principle demonstration of free-electron lasing using a laser wakefield accelerator[1]. However, the direct acceleration of heavier particles (e.g., protons or ions) to relativistic velocities within a few optical cycles remains challenging due to technical limitations and cost to date. Nevertheless, as a laser pulse-driven ion source, it essentially inherits the characteristics of the pulse, and it already demonstrated outstanding potential in beam duration, beam divergence, and acceleration gradient[2]. For example, the duration at the source is of the order of \sim ps, the high

number of protons in a single bunch ($10^{11} - 10^{13}$) and ultralow divergence[3, 4]. Based on these excellent properties, it has broad application prospects, including but not limited to fast ignitor, high-resolution charged-particle radiography[5] or radioisotope production[6].

Structure of the dissertation

The dissertation is structured as follows:

- ***Chapter 2:*** The theory of high-intensity laser-atom interaction is discussed. After that, we introduce the main properties of plasmas and related density diagnostic methods. Finally, we discuss the main mechanisms of laser particle acceleration.
- ***Chapter 3:*** In this chapter, we briefly introduce the large laser systems and instruments involved in the experiment and present the measurement results of related parameters.
- ***Chapter 4:*** First, we introduce the manufacturing method and related parameters of the ultrathin target in detail. Then, we demonstrate the characteristics of the ultrathin target that was fabricated in Jena. Finally, we measure the laser-induced damage threshold to ensure that the ultrathin target will not be broken by the probe light.
- ***Chapter 5:*** In this chapter, the experimental results of laser proton acceleration based on a high-contrast laser system are discussed. The experiments indicate that a monoenergetic proton beam can be generated with a planar multi-species target when using a high-contrast laser. Additionally, the proton energy spectrum and energy dependence are studied. EPOCH 2D are performed to explain the acceleration process of protons under ultra-intense laser fields.
- ***Chapter 6:*** The expanding plasma is irradiated by probing light of different colors to measure the transmittance and obtain the plasma density evolution

trend with time. The detection results are then corrected by solving the Helmholtz equation for the inhomogeneous plasma. Finally, the experimental results are compared with previous numerical model, demonstrating the superior ability of the numerical model to predict the plasma density evolution over time.

- **Chapter 7:** Provides a summary of the dissertation, and the prospects for future laser-based plasma accelerators are presented.

Theoretical Background

“If you want to have good ideas, you must have many ideas.

— Linus Pauling

With the development of ultra-fast and ultra-short pulse laser technology, the interaction between femtosecond lasers and matter has aroused great attention. Due to its extremely high electric field, almost all solid matter can be ionized in only a few optical cycles. The theoretical framework of the laser and matter ionization process is the cornerstone of strong-field physics. The primary subject of this chapter is the behaviour of atoms and electrons under intense femtosecond laser irradiation and the propagation of the laser in the produced plasma.

2.1 Ultrashort Laser Pulses

The starting point of electromagnetic wave propagation in space is Maxwell's equations. Maxwell's equations are a set of coupled partial differential equations, including Gauss's law, Gauss's law for magnetism, Maxwell–Faraday equation, and Ampère's circuital law. The equations will provide a mathematical model for electromagnetic waves and demonstrate how fluctuating electric and magnetic fields propagate in space. Maxwell equations¹ may be written as:

$$\textit{Gauss's law} \quad \nabla \cdot \mathbf{E} = \frac{\rho}{\epsilon_0}, \quad (2.1)$$

$$\textit{Gauss's law for magnetism} \quad \nabla \cdot \mathbf{B} = 0, \quad (2.2)$$

$$\textit{Maxwell – Faraday equation} \quad \nabla \times \mathbf{E} = -\frac{\partial \mathbf{B}}{\partial t}, \quad (2.3)$$

$$\textit{Ampère's circuital law} \quad \nabla \times \mathbf{B} = \mu_0 \left(\mathbf{J} + \epsilon_0 \frac{\partial \mathbf{E}}{\partial t} \right). \quad (2.4)$$

¹Note: Formulation in SI units convention

Here symbols in **bold** represent vector quantities, ε_0 is the permittivity of free space, μ_0 is the permeability of free space, ρ is the total electric charge density, \mathbf{J} is the total electric current density. Laser propagates in a vacuum without charges and currents, which means $\rho = 0$ and $\mathbf{J} = 0$ above. Defining $c = \frac{1}{\sqrt{\mu_0\varepsilon_0}}$, the equations above reduce to:

$$\nabla^2 \mathbf{E} - \frac{1}{c^2} \frac{\partial^2 \mathbf{E}}{\partial t^2} = 0, \quad (2.5)$$

$$\nabla^2 \mathbf{B} - \frac{1}{c^2} \frac{\partial^2 \mathbf{B}}{\partial t^2} = 0. \quad (2.6)$$

The above equations have the form of the standard wave equations in free space. The partial differential wave equation's most straightforward and most fundamental solution is a transverse plane wave. The laser as a transverse wave can be described by

$$\mathbf{E}(\mathbf{r}, t) = \mathbf{E}(\mathbf{r}, t) \cos(\mathbf{k} \cdot \mathbf{r} - \omega t + \phi(t)), \quad (2.7)$$

$$\mathbf{B}(\mathbf{r}, t) = \mathbf{B}(\mathbf{r}, t) \cos(\mathbf{k} \cdot \mathbf{r} - \omega t + \phi(t)), \quad (2.8)$$

where $\mathbf{E} = c\mathbf{B}$ are the time-dependent amplitude (envelope functions), \mathbf{k} is the wave number, ω is the angular frequency and ϕ is the phase. For the transverse plane wave, \mathbf{E} and \mathbf{B} lie on a plane and perpendicular to the propagation direction of the wave, \mathbf{E} and \mathbf{B} are also perpendicular to each other. The set of vectors constitutes a right-handed orthogonal set. In optics, the envelope of a laser is a smooth curve outlining its extremes for a gaussian pulse shape, which means the temporal envelope and transverse spatial profile of a laser beam are Gaussian functions profile, the field distribution in the focus ($z = 0$) can be written

$$E(\mathbf{r}, t) = E_0 e^{-4 \ln 2 \left(\frac{t}{\tau}\right)^2} e^{-\frac{(x^2+y^2)}{r^2}}, \quad (2.9)$$

where ω_0 is the beam waist, E_0 is the field amplitude in V/m, τ is the full width at half maximum (FWHM) of pulse duration, and r is the FWHM of focal spot size.

The energy carried by an electromagnetic wave is proportional to its amplitude squared. The intensity of the one pulse can be derived from the cycle-averaged Poynting vector, which means the intensity can be expressed as

$$I = \varepsilon_0 c^2 \langle |\mathbf{E} \times \mathbf{B}| \rangle = \frac{cn\varepsilon_0 E_0^2}{2}. \quad (2.10)$$

Here I is the average intensity in W/m^2 , n is the refractive index. The most important parameter describing the strength of a high-power laser is the dimensionless laser amplitude a_0 [7]. Assuming the motion equations of a free electron interacting with a monochromatic plane wave $A_0(kx - \omega t)$, A_0 is amplitude and $\mathbf{E} = -\frac{1}{c} \frac{\partial A_0}{\partial t}$, $\mathbf{B} = \nabla \times A_0$. The dimensionless laser amplitude governs the electrons in the regime,

$$a_0 = \frac{eE_0}{m_e c \omega} = \frac{eA_0}{m_e c^2}, \quad (2.11)$$

which indicates the essence of the dimensionless amplitude is $\frac{\text{Electron Kinetic Energy}}{\text{Electron Rest Energy}}$, the average energy gain of the electron in the laser field moving over a wavelength distance, divided by its rest energy[8]. When the $a_0 > 1$, the electrons in the laser field can be accelerated to the relativistic speed. A simpler expression is usually used in experiments,

$$a_0 = \rho \sqrt{\frac{I_0 \lambda^2}{10^{18} \text{W cm}^{-2} \mu\text{m}^2}}. \quad (2.12)$$

Here I_0 is the laser intensity and λ is the wavelength of the laser. ρ is 0.85 or 0.60, corresponding to linear or circular polarization, respectively. For electrons and protons, the corresponding values for $a_0 = 1$ are $I_0 \approx 10^{18} \text{W}/\text{cm}^2 (\mu\text{m}/\lambda)^2$ and $I_0 \approx 10^{24} \text{W}/\text{cm}^2 (\mu\text{m}/\lambda)^2$, respectively.

2.2 Laser Interaction with Single Atoms

As a laser begins to interact with matter, the behavior of natural atoms under intense laser fields plays a significant role in laser-plasma interactions. The Bohr model of the ground state of hydrogen can be used to derive the Bohr radius,

$$a = \frac{\hbar^2}{me^2} = 5.29 \times 10^{-11}m, \quad (2.13)$$

the corresponding electric field strength is

$$E_a = \frac{e}{4\pi\epsilon_0 a^2} = 5.1 \times 10^9 V/m. \quad (2.14)$$

From electric field strength, one can find the atomic unit of intensity (flux)

$$I_a = \frac{c\epsilon_0 E_a^2}{2} = 3.45 \times 10^{16} W/cm^2. \quad (2.15)$$

2.2.1 Multi-Photon Ionization (MPI)

As early as 1931, Göppert-Mayer[9] gave a theoretical prediction, but it was not until 1968 that P. Agostini[10] formally recommended "*Multi-Photon Ionization (MPI)*" in experiment. MPI refers to an electron in an atom or molecule that instantaneously absorbs the minimum number of photons required for its ionization. The electron transits through a series of short-lived (usually sub-femtosecond) virtual energy levels from a ground state to a continuous state. The laser must provide a sufficiently high photon density, and at this time, the laser electric field strength is weaker than the binding strength of electrons in atoms. The laser field is not enough to disturb the atomic Coulomb field. The essence of multiphoton ionization lies in the photon flux[11]

$$I = \frac{n\omega\hbar}{\Delta t \cdot A}, \quad (2.16)$$

where n is the number of photon, A is irradiation area. MPI occurs when the laser power density is generally on the order of $10^{12}W/cm^2$.

2.2.2 Above-Threshold Ionization (ATI)

If an atom or molecule is in an intense laser field and absorbs more photons than required to overcome its bound energy, the resulting kinetic energy of the ionized electron will be greater than the energy of one photon, $\hbar\omega$. The final kinetic energy of the electron can be expressed as

$$E_{kin} = (n + m)\hbar\omega - E_{ion}. \quad (2.17)$$

Here, E_{kin} is the final kinetic energy of the electron, n is the minimum number of photons required to overcome the binding energy, m is the excess absorbed, and E_{ion} is the ionization energy. The measured electron energy spectra typically consist of several distinct peaks beyond the ionization energy E_{ion} , with the energy difference between adjacent peaks being one photon energy $\hbar\omega$ [12, 13]. Unlike MPI, ATI deviates strongly from lowest-order perturbation theory, even at relatively low intensities of $10^{13}\text{W}/\text{cm}^2$ [14].

2.2.3 Tunneling Ionization (TI)

The height of the Coulomb barrier of atoms or molecules in the intense laser electric field will be reduced due to the suppression of the strong laser electric field vector. At this time, electrons will likely pass through the suppressed Coulomb barrier and become free. The principle of *Tunneling Ionization (TI)* was first proposed by Keldysh and Perelomov [15, 16]. TI is considered to be a quasi-static situation. The electron needs to have a tunneling time. That is, the laser cycle should be greater than the tunneling time, and the electron has a greater chance of tunneling out of the potential barrier. Keldysh introduces a Keldysh parameter, γ [17, 15], to the borderline between MPI and TI, given by

$$\gamma = \omega_L \sqrt{\frac{2E_{ion}}{I_L}} \sim \sqrt{\frac{E_{ion}}{\Phi_{pond}}}, \quad (2.18)$$

where

$$\Phi_{pond} = \frac{e^2 E_L^2}{4m\omega_L^2}. \quad (2.19)$$

As a rule of thumb, if $\gamma > 1$, the ionization process belongs to MPI; If $\gamma < 1$, TI is the main form of ionization, which depends on the strong laser field and wavelength. If $\gamma \approx 1$, two mechanisms exist simultaneously and compete.

2.2.4 Barrier Suppression Ionization (BSI)

As the laser intensity continues to increase, at certain laser intensity, its peak intensity can be approximated by the Coulomb barrier of atoms or even exceed the Coulomb barrier. The Coulomb barrier is suppressed at this time, and electrons can freely escape from the atom and become free electrons. This process is so-called *Barrier Suppression Ionization (BSI)*. The minimum laser intensity for BSI is

$$I_{BSI} = 4 \cdot 10^9 (E_{ion}[eV])^4 Z^{-2} W/cm^2. \quad (2.20)$$

Note that E_{ion} is the ionization potential of the ion, Z is the ion charge. The potential

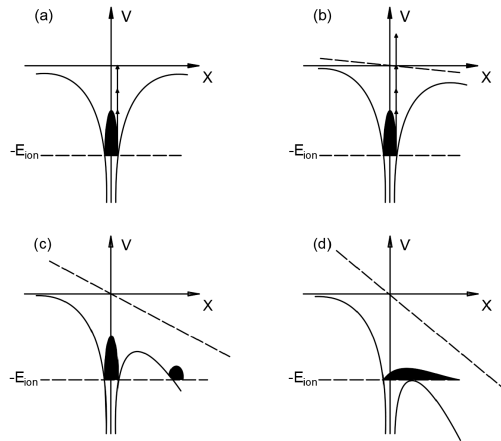


Fig. 2.1: Schematic picture of different ionization models. (a) Multi-Photon Ionization (MPI). (b) Above-Threshold Ionization (ATI). (c) Tunneling Ionization (TI). (d) Barrier Suppression Ionization (BSI).

energy curve of an atom under the interaction of an external field is shown in Fig. 2.1. Among them, (a) shows an ATI process, where the electrons are bound in the atomic potential wall, and the electron is released by absorbing multi-photons with minimal kinetic energy. For MPI, as shown in (b), the electrons absorb more photons than necessary to overcome the potential, leaving the mother atom with significant energy. When the external electric field of the laser continues to increase, the external field becomes comparable to the potential, and the potential energy

curve is depressed, as shown in (c). The ionization takes place via TI, and there is a high probability that electrons will pass through the barrier. The applied laser electric field is strong enough to exceed the Coulomb barrier, and BSI becomes dominant. At this point, the potential barrier is completely suppressed, and electrons can freely escape from atoms, becoming free electrons, as shown in (d).

In actual experiments, the interaction between the laser and matter is highly complex and involves all the ionization models mentioned above. From a time perspective, due to imperfect laser pulse compression, the pre-pulse appears on the ps-time scale with intensity $I = 10^{13} - 10^{15} \text{W/cm}^2$, and ATI plays a significant role before the main laser pulse arrives. From another space perspective, the laser energy concentrates on the airy disk in the focal plane, and field ionization processes dominate. However, the external lobes around the airy disk, involving ATI, can still ionize the target in the PW laser experiment.

2.3 Laser-single Electron Interactions

Electrons have a rapid response to electromagnetic fields due to their large charge-to-mass ratio. Therefore, understanding their movement in strong fields is indispensable for studying laser-driven particle acceleration. To start understanding laser-single electron interactions, it is helpful to consider the non-relativistic motion of an electron in a plane wave, which is an approximate calculation but can provide a general sense of the interaction. Although the electric and magnetic fields are real physical quantities, it is more convenient to use their complex representation in mathematics. Therefore, a plane wave propagating in the x-direction can be expressed as

$$\mathbf{E} = \mathbf{E}(x, t) = E_0 \hat{\boldsymbol{\epsilon}} e^{i(kx - \omega t)} \quad \text{and} \quad \mathbf{B} = \mathbf{B}(x, t) = \hat{\mathbf{x}} \times \mathbf{E}. \quad (2.21)$$

Here $\hat{\boldsymbol{\epsilon}}^2$ is the complex polarization vector and $k = \omega/c$. For linear polarization along y(z), $\hat{\boldsymbol{\epsilon}} = \hat{\mathbf{y}}(\hat{\mathbf{z}})$, while for circular polarization, $\hat{\boldsymbol{\epsilon}} = (\hat{\mathbf{y}} \pm i\hat{\mathbf{z}})/\sqrt{2}$ represents counterclockwise and clockwise directions, respectively.

²Note: 'hat' symbol indicates an unit vector

2.3.1 Non-relativistic Regime

The motion equations of an electron in a non-relativistic electromagnetic are

$$m_e \frac{d\mathbf{v}}{dt} = -e[\mathbf{E}(\mathbf{r}, t) + \frac{\mathbf{v}}{c} \times \mathbf{B}(\mathbf{r}, t)], \quad (2.22)$$

$$\frac{d\mathbf{r}}{dt} = \mathbf{v}. \quad (2.23)$$

Here, \mathbf{E} and \mathbf{B} represent the electric and magnetic field intensities, respectively, and c is the speed of light in vacuum. This equations of motion are applicable in both non-relativistic and relativistic dynamics. In non-relativistic electromagnetism, the dimensionless laser amplitude $a_0 \ll 1$, and the term $\mathbf{v} \times \mathbf{B}$ can be neglected due to the small magnitude of the velocity $|\mathbf{v}| \ll c$ in weak fields. As a result, the linear solution can be obtained immediately,

$$\mathbf{v} = -\frac{ie}{\omega m_e} \mathbf{E} \quad \text{and} \quad \mathbf{r} = -\frac{e}{\omega^2 m_e} \mathbf{E}. \quad (2.24)$$

Since there is no force acting in the longitudinal direction, the electric field is assumed to be constant at the electron's longitudinal direction. This assumption leads to a solution where the electron's trajectory is a straight line for linear polarization and a circle for circular polarization.

However, if a_0 is close to unity, the influence of magnetic force should be considered. Here we adopt the ‘‘perturbative’’ method introduced by Macchi[18] and write the electron velocity as $\mathbf{v} = \mathbf{v}_1 + \mathbf{v}_2$ where \mathbf{v}_1 and \mathbf{v}_2 are of order $\sim a_0$ and $\sim a_0^2$, respectively. The motion equation above is

$$m_e \frac{d(\mathbf{v}_1 + \mathbf{v}_2)}{dt} = -e[\mathbf{E}(\mathbf{r}, t) + \frac{(\mathbf{v}_1 + \mathbf{v}_2)}{c} \times \mathbf{B}(\mathbf{r}, t)]. \quad (2.25)$$

Simplify the above equation, one can obtain:

$$m_e \frac{d\mathbf{v}_1}{dt} = -e\mathbf{E}(\mathbf{r}, t), \quad (2.26)$$

$$m_e \frac{d\mathbf{v}_2}{dt} = -e\frac{\mathbf{v}_1}{c} \times \mathbf{B}(\mathbf{r}, t). \quad (2.27)$$

The equation 2.26 indicates the result is the linear solution.

For **linear** polarization along y , inserting the dimensionless laser amplitude a_0 and 2.21, 2.26 can be written as

$$\mathbf{v}_1 = \frac{eE_0}{m_e\omega} \hat{\mathbf{y}} \sin(\omega t), \quad (2.28)$$

$$y_1 = -a_0 \frac{c}{\omega} \cos(\omega t), \quad (2.29)$$

where the initial position of the electron is $x = 0$ to simplify the calculation. Inserting $\mathbf{B}(x = 0, t) = E_0 \hat{\mathbf{z}} \cos(\omega t)$ into 2.27, we can obtain

$$\frac{d\mathbf{v}_2}{dx} = -\hat{\mathbf{x}} \frac{e}{m_e c} (a_0 c \sin(\omega t)) (E_0 \cos(\omega t)) = -\hat{\mathbf{x}} \frac{a_0^2}{2} c \omega \sin(2\omega t). \quad (2.30)$$

The above suggests the electron oscillates along the x direction with frequency 2ω ,

$$v_2(t) = \frac{a_0^2 c}{4} \cos(2\omega t), \quad (2.31)$$

$$x_2(t) = -\frac{a_0^2 c}{8\omega} \sin(2\omega t). \quad (2.32)$$

Defining the dimensionless coordinates $X = \frac{\omega x}{ca_0}$ and $Y = \frac{\omega y}{ca_0}$, the trajectory of the electrons is similar to *figure-of-eight* curve, as shown in Fig.2.2,

$$16X^2 = Y^2(1 - Y^2). \quad (2.33)$$

For **circular** polarization, $\mathbf{v}_1 \times \mathbf{B}$ can be written

$$\mathbf{v}_1 \times \mathbf{B} \propto (-\hat{\mathbf{y}} \sin\omega t \pm \hat{\mathbf{z}} \cos\omega t) \times (\hat{\mathbf{z}} \cos\omega t \mp \hat{\mathbf{y}} \sin\omega t) = 0, \quad (2.34)$$

so that the trajectory of the electron is unaffected by $\mathbf{v}_1 \times \mathbf{B}$ in the first order of approximation.

Fig.2.2 illustrates two main features of an electron in a monochromatic plane wave. First, the electron oscillates along the x direction and the y direction, it follows two frequencies, 2ω and ω , respectively. Second, the electron's initial position coincides with its final position after one laser cycle, indicating that the electron cannot gain energy from a monochromatic plane wave.

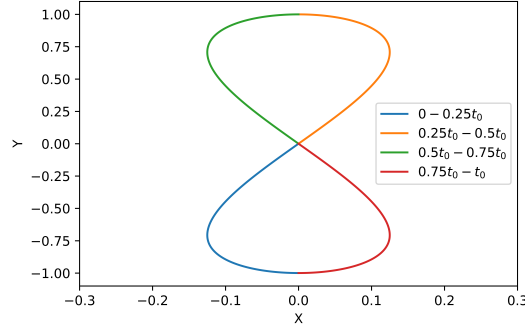


Fig. 2.2: The trajectory of an electron in a monochromatic plane wave. Each quarter period of one light cycle corresponds to different colors.

2.3.2 Relativistic Regime

When one electron moves in a relativistic field, the electron energy is described by the following equation,

$$\frac{d}{dt}(m_e \gamma c^2) = -e \mathbf{v} \cdot \mathbf{E}, \quad (2.35)$$

where $\gamma = \frac{1}{\sqrt{1-v^2/c^2}}$. Assuming that the EM plane wave propagates along x and its vector potential $\mathbf{A} = \mathbf{A}(x, t)$. From the references[18, 19], 2.35 yields the following relation

$$\frac{d}{dt}(\mathbf{p}_\perp - \frac{e}{c} \mathbf{A}) = 0. \quad (2.36)$$

Here \mathbf{p} is the momentum of the electron, and the subscript \perp refers to the vector components of momentum in the transverse y - z plane. The vector potential, \mathbf{A} , can be written as:

$$\mathbf{A} = A_0 [\hat{\mathbf{y}} \delta \cos \phi + \hat{\mathbf{z}} (1 - \delta^2)^{1/2} \sin \phi]. \quad (2.37)$$

Here $\phi = kx - \omega t$, δ is a polarization parameter. For $\delta = 1$ or 0 , the wave is linearly polarized along y or z axis, respectively, while for a circularly polarized wave, $\delta = \pm \frac{1}{\sqrt{2}}$. Other values of δ correspond to the wave with elliptical polarization. When combining the equation of motion with 2.37, ϕ must be considered a function of the particle position, $\phi = \phi[x(t), t]$. Since it will be convenient to use ϕ as the only variable we evaluate its derivative to time as

$$\frac{d\phi}{dt} = \frac{\partial \phi}{\partial t} + v_x \frac{\partial \phi}{\partial x} = -\omega + \frac{p_x}{m_e \gamma} k = -\omega + \frac{m_e c (\gamma - 1) \omega}{m_e \gamma c} = -\frac{\omega}{\gamma} \quad (2.38)$$

and

$$\mathbf{p} = m_e \gamma \frac{d\mathbf{r}}{dt} = m_e \gamma \frac{d\phi}{dt} \frac{d\mathbf{r}}{d\phi} = -m_e \omega \frac{d\mathbf{r}}{d\phi} \quad (2.39)$$

Finally, we get the following results with some simple algebra:

$$\mathbf{p}_\perp = (p_y, p_z) = \frac{eA_0}{c}(\delta \cos\phi, (1 - \delta^2)^{1/2} \sin\phi) \quad (2.40)$$

$$p_x = \frac{1}{2m_e c} \left(\frac{eA_0}{c}\right)^2 [(\delta \cos\phi)^2 + (1 - \delta^2) \sin^2\phi] \quad (2.41)$$

$$= \frac{1}{4m_e c} \left(\frac{eA_0}{c}\right)^2 [1 + (2\delta^2 - 1) \cos 2\phi] \quad (2.42)$$

where the term $\cos 2\phi$ means the frequency is 2ω and its cycle average, $\langle \cos 2\phi \rangle = 0$.

$$\langle p_x \rangle = \frac{1}{4m_e c} \left(\frac{eA_0}{c}\right)^2 = m_e c \frac{a_0^2}{4} = \text{constant}. \quad (2.43)$$

The above equation indicates that the electron has a constant drift in the x direction. The trajectory can integrate (1.40, 1.41) concerning ϕ , and normalizing the coordinates to $\frac{1}{k} = \frac{c}{\omega}$ and $\hat{\mathbf{r}} = k\mathbf{r}$. The trajectory of the electron can be given by:

$$\frac{\hat{x}}{a_0^2} = -\frac{1}{4} \left[\phi + \left(\frac{1}{2} - \delta^2\right) \sin 2\phi \right], \quad (2.44)$$

$$\frac{\hat{y}}{a_0} = -\delta \sin\phi, \quad (2.45)$$

$$\frac{\hat{z}}{a_0} = (1 - \delta^2)^{1/2} \cos\phi. \quad (2.46)$$

Corresponding trajectory diagram is shown in Fig.2.3.

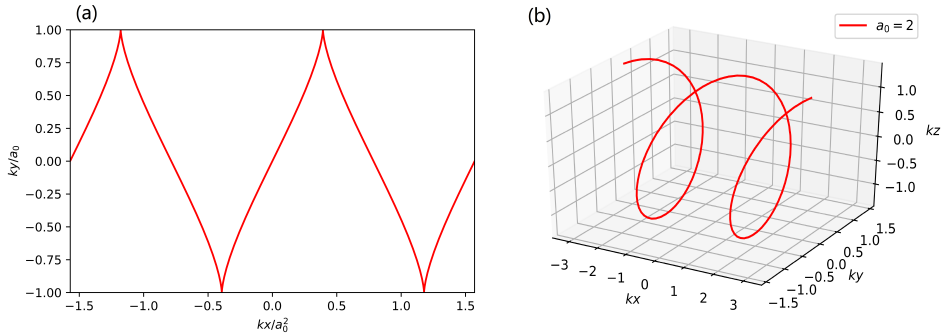


Fig. 2.3: (a) and (b) correspond to the trajectories of electrons in linearly and circularly polarized plane waves.

When comparing $a_0 = 0.5$ and $a_0 = 2$ in Fig.2.4, it is observed that the shape of the electron trajectory in a relativistic laser field approached a flat-top. This suggests

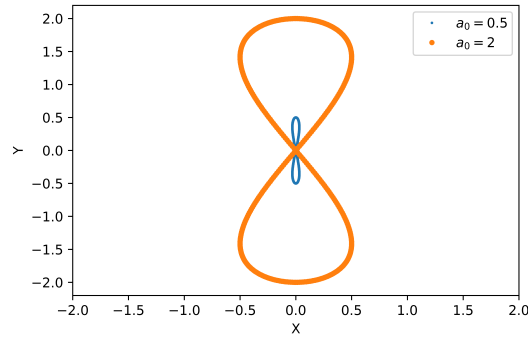


Fig. 2.4: Electron trajectories under different electromagnetic fields.

that the effect of polarization became less pronounced in the relativistic regime, as oscillations occurred in all directions of the electric field.

2.4 Fundamentals of Plasma and Plasma Diagnosis

2.4.1 General Properties of Plasmas

The essence of laser interactions with solid targets is that the laser interacts with plasma induced by the laser leading edge in the field of high-power laser research. Plasma, often referred to as ionized gas of sufficient size, displays characteristics such as good electrical and thermal conductivity, waveguide properties[20], and high energy carrying capacity, making it an excellent experimental carrier for high-energy physics. Plasma can be produced through electric discharge and photo-ionization processes in the laboratory, showing macroscopic neutrality and Coulomb force interactions on a microscopic level. In weakly ionized plasma, charge-neutral interactions dominate, while in fully ionized plasma, all particles are involved in multiple Coulomb interactions. However, not all media containing charged particles can be classified as plasma, certain conditions must be met for a plasma to exist. Macroscopic neutrality refers to the balance between the electrostatic potential among charged particles, and the thermal energy of particles inside, which tends to disturb electrical neutrality. The Debye length represents the physical scale at which mobile charge carriers, such as electrons, screen out electric fields in plasmas.

The Debye length, λ_D , is tightly related to the plasma temperature, and the electron number density according to

$$\lambda_D = \sqrt{\frac{\varepsilon_0 k / e^2}{n_e / T_e + \sum_j Z_j^2 n_j / T_i}}. \quad (2.47)$$

Where e is the charge of an electron, T_e and T_i are the temperatures of the electrons and ions, respectively. n_j is the density of atomic species j and Z is the atomic number. n_e is the density of electrons. The above equation is referred to as a non-isothermal plasma in which the temperatures of electrons and heavy species are different. While in a quasi-neutral cold plasma, the mobility of ions is negligible, the ion term is dropped, giving

$$\lambda_D = \sqrt{\frac{\varepsilon_0 k T_e}{n_e e^2}}. \quad (2.48)$$

The Debye length is a fundamental and crucial requirement for the existence of plasma. The physical dimension of any plasma must be larger than the corresponding Debye length. Otherwise, there is not sufficient space to form the collective plasma behavior, therefore

$$L \gg \lambda_D. \quad (2.49)$$

Here L is a characteristic dimension of the plasma. The number of electrons, N_D , inside a Debye sphere can be estimated from the minimum system size,

$$N_D = \frac{4}{3} \pi n_e \lambda_D^3. \quad (2.50)$$

When a plasma is disturbed from the equilibrium condition by a momentary force, the internal space charge field tends to restore the original charge neutrality. It is a collective motion characterized by an oscillation frequency called the plasma frequency, the quantity defined by

$$\omega_p = \sqrt{\frac{n_e e^2}{m_e \varepsilon_0}}. \quad (2.51)$$

The ion is much heavy than the electron, and the electrons oscillate collectively among the ions. However, the ions cannot follow the motion of these electrons in turn, so these collective oscillations are high-frequency oscillations. The Coulomb attraction provides the collective restoring force.

2.4.2 Plasma Diagnostic Methods

Plasma diagnosis relates to various methods, experimental instruments, and techniques used to measure plasma properties, including but not limited to plasma components' density, distribution function over energy, plasma spatial profiles, and dynamics. From the perspective of detection, it can be divided into the following categories, passive spectroscopy, active spectroscopy, invasive/non-invasive probe methods, and so on. Plasma is often accompanied by radiation emission. Passive spectroscopic methods are very straightforward and reliable for observing the radiation emitted by the plasma, such as Doppler shift/broadening of ions, Stark broadening, and Stark effect. These effects successfully determine the temperature, density, and even the local electric field of the plasma. On the contrary, active spectroscopic methods stimulate the plasma in some way and observe the emission of radiation, absorption of the stimulating light, or others results. For example, in the absorption spectroscopy method[21], a light source with a specific wavelength passes through the plasma, due to an inevitable transition of one of the species present in the plasma, some wavelengths of the light source are absorbed, and a range of information on the plasma that can be deduced from the transmission spectrum. This profile provides information not only for the plasma parameters but also for the absolute density of the species in the plasma. However, probe methods mainly consist of two types, namely invasive and non-invasive probe methods. For invasive probe methods, it usually places a small metal electrode in the plasma to directly determine the characteristics of the plasma. The whole system consists of a voltage source, a measuring probe, and a reference electrode, which usually measures the volt–ampere characteristics of the instrument. In contrast to the majority of other diagnostic methods mentioned above, the invasive probe method gives the plasma characteristics local values. The invasive probe methods are brutal to be applied to atmospheric plasmas due to severe perturbation by the electrical probes. In some scenarios (e.g., proton radiography), the metal electrode can be replaced by a proton beam, one high-quality proton beam produced by a proton source interact with the plasma due to the strong electric field and magnetic field in the plasma, the trajectory of the proton beam deflects. As a result, the intensity profile of the proton detection beam is measured by a screen after the interaction area. One can deduce the integrated magnetic field or electric field from the intensity profile. Whether it

is a metal electrode or a proton beam, it will inevitably affect the local plasma. To overcome this or at least reduce the influence of external measurements on plasma, non-invasive optical methods have been introduced. Microwave interferometry can determine the electron density of the plasma, and holographic interferometry examines the spatial distribution of the plasma and so on. A frequency-domain interferometer is used to investigate a femtosecond laser-produced plasma with subnanometer spatial resolution[22]. The technique can measure a probe pulse's amplitude and phase variations interacting with plasma. The duration of the probe pulse limits the temporal resolution, and the spatial resolution is limited by the optical imaging device. The above is just a basic introduction to plasma diagnosis, more extended reading can be found in *Ovsyannikov*[23].

One critical issue in plasma-based acceleration is determining the plasma parameters before and during the acceleration process. Various plasma densities are required based on the particles being accelerated. For Laser wakefield accelerators (LWFA), a critical plasma density of approximately 10^{19}W/cm^2 is necessary to generate quasi-monoenergetic electron beams at the GeV level. *Sävert et al.*[24] utilizes the few-femtosecond shadowgraphic snapshot method to extract the nonlinear evolution of the plasma wave in a laser wakefield accelerator with transverse synchronized few-cycle probe pulses. This method can directly measure the electron density distribution of the plasma and provide quantitative information about its size and shape. It can monitor the complete nonlinear evolution of the plasma wave during the acceleration process and provide a greater understanding of acceleration in the bubble regime, even for more complex acceleration geometries. However, measuring plasma under dense plasma conditions becomes more complicated. Shadowgrams were used by *Tatarakis et al.*[25] to investigate the high-intensity laser-generated fast electrons on a thick plastic target ($140 \mu\text{m} - 250 \mu\text{m}$). The probe is separated from the uncompressed main beam, and the frequency is doubled to green (527 nm). The probe is incident on the interaction area from the target side, and the front and back surfaces are in the field of view. The probe beam passes transversely across the target, and the shadowgraphic system is on the other side. When the local plasma exceeds the critical density, the probe is blocked, and a dark spot at the target surface is present. An unavoidable problem is a bright spot in the plasma center due to the second harmonic self-emission. A similar method employed in proton acceleration can be found in [26].

2.5 Laser Plasma Acceleration

Mechanisms

As laser-driven particle acceleration continues to develop, various acceleration mechanisms have been theoretically proposed. This section introduces the laser-driven ion acceleration mechanisms, which are essential for understanding and developing laser-driven ion sources. Several of these mechanisms have already been confirmed by significant experiments. However, in actual experiments, the acceleration process is often a combination of multiple mechanisms, particularly when considering the spatial distribution of the focus and laser temporal contrast.

2.5.1 Target Normal Sheath Acceleration (TNSA)

In most reported experiments, Target Normal Sheath Acceleration (TNSA) is one of the most widely recognized and dominant mechanisms for proton acceleration. The most successful description of proton acceleration was proposed by *Hatchett et al.*[27] and *Wilks et al.*[28]. TNSA relies on a few tens of microns thick solid target and a relativistic laser with an $a_0 > 1$. A high-intensity laser pulse generates fast electrons with electrical currents exceeding 10^5 A. These electrons propagate through the target, building a sheath region at the rear side with a size of around $10 \mu\text{m} - 100 \mu\text{m}$. In this sheath region, a space-charge electric field can reach the order of TV/m, accelerating ions in the direction perpendicular to the target surface. One of the significant features of TNSA is that the ion-emitting direction is independent of the laser incident direction and is always perpendicular to the emitting surface.

To better explain plasma expansion into a vacuum quantitatively and accurately, *Mora*[29] provides a detailed discussion of the process. The model consists of plasma, including cold and stationary ions, occupying half the space ($x < 0$), with a sharp boundary on the other side ($x > 0$) without any plasma. The electron density is described using the Boltzmann distribution,

$$n_e = n_{e0} \exp(q\Phi/k_B T_e). \quad (2.52)$$

Here, n_{e0} represents the unperturbed electron density, q is the charge, and T_e is the electron temperature. The electrostatic potential, denoted by Φ , satisfies the Poisson equation,

$$\epsilon_0 \frac{\partial^2 \Phi}{\partial x^2} = q(n_e - Zn_i). \quad (2.53)$$

Here, Z denotes the ion charge number, and $n_{e0} = Zn_{i0}$ represents the relationship between the unperturbed electron density and the ion density. Assuming that the electrons remain in equilibrium with the electrostatic potential Φ [30], the ion expansion into a vacuum can be described by a continuous motion equation,

$$\left(\frac{\partial}{\partial t} + v_i \frac{\partial}{\partial x}\right)n_i = -n_i \frac{\partial v_i}{\partial x}, \quad (2.54)$$

$$\left(\frac{\partial}{\partial t} + v_i \frac{\partial}{\partial x}\right)v_i = -(Zq/m_i) \frac{\partial \Phi}{\partial x}, \quad (2.55)$$

where v_i is the ion velocity. Assuming quasi-neutrality in the expanding plasma and $x + c_{st} > 0$, one self-similar expression is

$$E_{ss} = k_B T_e / qc_{st} = E_0 / \omega_{pi} t. \quad (2.56)$$

Here E_{ss} is the self-similar result, c_s is the ion sound velocity, and ω_{pi} is the plasma frequency. The self-similar solution predicts the ion front velocity and the electric field at the ion front,

$$v_{front} \simeq 2c_s \ln(\tau + \sqrt{\tau^2 + 1}), \quad (2.57)$$

$$E_{front} \simeq 2E_0 / (2e + \omega_{pi}^2 t^2)^{1/2}, \quad (2.58)$$

where e is the Euler's number, $\tau = \omega_{pi} t / \sqrt{2e}$ is the normalized acceleration time. The two crucial predictions of this model are the ions energy spectrum and the corresponding cut-off energy as follows, respectively,

$$dN/d\varepsilon = (n_{i0} c_{st} / \sqrt{2\varepsilon \varepsilon_0}) \exp(-\sqrt{2\varepsilon / \varepsilon_0}), \quad (2.59)$$

$$\varepsilon_{max} \simeq 2\varepsilon_0 [\ln(2\tau)]^2. \quad (2.60)$$

Here $\varepsilon_0 = Zk_B T_e$, and T_e is the temperature of the hot electrons driving the rear surface expansion. The self-similar model has no meaning if the initial Debye length is larger than the self-similar density scale length $c_s t$, and the acceleration time of the model is infinite, the energy keeps increasing over time in 2.59.

TNSA can be summarized as the follows. First, the TNSA model is an isothermal process, which means the electron temperature is assumed to be approximately equal to the ponderomotive potential[31],

$$T_e = \Phi_p = mc^2[\sqrt{1 + a_0^2} - 1] \simeq 511[\sqrt{1 + 0.73I_{18}\lambda_{um}^2} - 1] keV. \quad (2.61)$$

Here a_0 is the normalized amplitude of the laser field. Assuming that the relativistic laser is incident on the plasma in the normal direction, the dominant mechanism is $\mathbf{J} \times \mathbf{B}$ because the electric field is perpendicular to the density gradient of the plasma. Second, some research groups[32, 33] have calculated the plasma sheath radius, r , at the rear target surface by measuring the hot electrons from the front surface through the target of thickness l ,

$$r = r_0 + l \tan \theta, \quad (2.62)$$

where r_0 is the focal spot radius and θ is a fitting parameter by experiment. The plasma sheath radius is of the order of several to a few tens of degrees[32, 33]. Third, the acceleration time of ions has been found[29],

$$t_{acc} \approx 1.3\tau_{laser} \quad (2.63)$$

where τ_{laser} is the laser pulse duration. It has been examined by comparing experimental results with particle-in-cell (PIC) simulation[34]. The acceleration time limit makes sense. Because the TNSA model is based on the equilibrium hypothesis, which means the electrons' temperature distribution remains constant. But these electrons interact with ions and transform energy to the background ions by collision and the sheath field. As a result, the electron temperature and distribution will significantly change. Therefore, the isothermal approximation in TNSA is valid only for a limited period of time, typically on the order of the acceleration time[29, 35]. The last and most critical feature is that the energy spectrum of the TNSA mechanism results in an exponential spectrum, and the cut-off energy spectrum highly

depends on the driving electron temperature. These accelerated ions gain a certain amount of energy from the sheath electric field before escaping into the vacuum. The energy that the ions acquire depends on their initial position within the sheath and the local electric field strength. Due to the complex electric field in the sheath and the random positions of the ions within it, the resulting ion energies shows an exponential distribution. For heavy ion acceleration, a key step is to remove hydrocarbon contamination and water vapor from the target surface, as protons have the highest charge-to-mass ratio and the contamination layer is located on the target surface exposed to the highest field gradients, they are always accelerated first.

The exponential spectrum generally constitutes the main disadvantage of TNSA, which is not ideal for many applications. Some research groups tried to produce a quasi-monoenergetic ion beam. *Hegelich et al.*[36] heated a 20 μm palladium substrate to 600 k, the target was wholly dehydrogenized, but carbon atoms were still on the surface. Increasing the heating temperature to 1100 K, it caused the phase change of carbon and the formation of a monolayer or graphite on the palladium surface. By pre-processing, the target C^{5+} ions were accelerated to 3 MeV/u with a lower energy spread of 17 %. As for proton beams, *Schwoerer et al.*[37] demonstrated that quasi-monoenergetic proton beams can be generated by high-intensity relativistic laser irradiating microstructured targets, where PMMA dots with a size of 20 $\mu\text{m} \times 20 \mu\text{m}$ are located on the surface of a 5 μm thick titanium foil. The reproducible quasi-monoenergetic proton spectrum was dominated by a narrow band structure around 1.2 MeV with FWHM = 0.3 MeV. The above has described pre-processed or specially configured targets irradiated with high-intense laser pulses to acquire an ion beam or quasi-monoenergetic proton beam. Other monochromatization techniques, namely the phase rotation technique[38, 39] and the laser-driven microlens technique[40], have more complex instruments (e.g., RF cavity or permanent quadrupole magnets) and long transport system with relatively low transmission efficiency[41].

2.5.2 Radiation Pressure Acceleration (RPA)

As of today, the exponential energy spectrum and cut-off energy of particles produced by TNSA still cannot meet the requirements of tumor treatment, e.g., hundreds of megaelectron volts and a narrow-band spectrum. It is necessary to develop a new acceleration mechanism to improve energy conversion efficiency and decrease energy dissipation. When the laser intensity is greater than $10^{24}\text{W}/\text{cm}^2$ ($a_0 \sim 1836$), protons in the strong light field can be directly accelerated to relativistic energy. Nevertheless, this is still a challenge to overcome, considering the state-of-the-art laser technology. However, laser-plasma-based acceleration, because of the collective acceleration effect when the number of electrons is far greater than the number of ions in the electron cloud[42], requires only $10^{21}\text{W}/\text{cm}^2$ for protons to accelerate to relativistic speed. From the viewpoint of waves, Maxwell's theory of electromagnetism indicates that any electromagnetic wave carries momentum, which can be transferred to a non-transparent object it hits. In terms of photons, light irradiates an opaque target, and photons transfer their momentum to the body, causing a change in the energy of the scattered photon. With increasing laser intensity, the magnetic force term cannot be ignored anymore and drives electron oscillations along the density gradient of plasma. This effect is called relativistic $\mathbf{J} \times \mathbf{B}$ heating[43]. For relativistic lasers, the $\mathbf{J} \times \mathbf{B}$ component of the Lorentz force becomes comparable with the transverse motion associated with the electric field. Therefore, a significant longitudinal force generates along the laser propagation direction with 2ω oscillation frequency. It works for any polarization except circular polarization. Radiation Pressure Acceleration (RPA) can be further classified into two modes based on the initial target thickness: hole-boring RPA[44, 45, 46] for relatively thick targets and light-sail RPA[47, 48] for thin targets, respectively. Thick and thin here are relative terms to laser intensity, and their essence is whether the laser pulse can pass through the target body during the interaction.

1. Hole-Boring RPA (HB-RPA):

When a circular polarization laser interacts with overdense plasma, due to the ponderomotive force, the electrons are piled up in the front of the laser, forming a high-density thin electron spike. The electron spike is continuously pushed inward to the target inside and forms depressions on the surface. The thickness of the overdense plasma is larger than the penetration depth of the laser pulse. In other

words, the laser pulse duration is shorter than when the laser pulse penetrates plasma, and the laser pulse is perfectly reflected from the high-density electron layer. The process will continue without any limitations as long as the laser continues. This model is referred to as the conventional hole boring[49, 50]. However, the plasma is heated by the driving laser continuously, and the plasma starts to expand when the electron pressure exceeds the radiation pressure of the driving laser, leading to the plasma blowout to the front side. The plasma density limits for hole boring are given by[51]

$$a_0 n_c \leq n_e \leq 8Ra_0^2 n_c. \quad (2.64)$$

Here a_0 is the normalized laser field amplitude, n_c is the non-relativistic critical density, and R is the reflectivity at the transition time from the hole boring to the blowout.

The heavy ions lag behind the electron spike and are pulled by the rising charge-separation field between the ions and the electron spike. To better understand the characteristics of HB-RPA, it is important to compare the non-relativistic and relativistic expressions. *Robinson et al.*[46] compared the non-relativistic and relativistic expressions of HB-RPA, with the hole-boring velocity in the lab frame given by

$$v_b = \sqrt{\frac{I}{m_i n_i c}} = \sqrt{c^2 \Xi}, \quad (2.65)$$

where I is laser intensity, m_i and n_i are the ion mass and the ion density, respectively. Ξ defines a dimensionless pistoning parameter,

$$\Xi = \frac{I}{\rho c^3}, \quad (2.66)$$

where ρ is the mass density of the plasma. Finally, the energy of the ions is given by

$$\epsilon = \frac{2I}{n_i c} = 2m_i c^2 \Xi. \quad (2.67)$$

It reveals a key parameter: the energy of the ions depends on the plasma's mass density and laser intensity. Pulse duration does not affect the ion energy compared

with TNSA. For the relativistic theory of HB-RPA, the relativistically correct HB velocity is

$$\beta_b = \frac{\sqrt{\Xi}}{1 + \Xi}. \quad (2.68)$$

The energy of the ions is

$$\varepsilon = m_i c^2 \left[\frac{1 + \beta_b^2}{1 - \beta_b^2} - 1 \right]. \quad (2.69)$$

2.Light-Sail RPA (LS-RPA):

If a circular polarization laser interacts with thin over-density plasma, the electrons are piled up in the front of the laser as the process of the HB-RPA. When the compressed electron layer reaches the rear side of the target's initial position, leading to the whole target moving and the intense laser penetrating the target. The electron layer is driven forward by laser pulse while ions in the foil are accelerated by the positive charge separation field. This phenomenon is known as Light-Sail Radiation Pressure Acceleration (LS-RPA)[52, 53]. The obvious advantage is that the LS-RPA mechanism has high energy conversion efficiency and monoenergetic energy spectrum distribution[52, 53]. A key requirement is that the light pressure and space charge electrostatic force, E_{\parallel} , must be balanced, that is, the electron layer cannot be broken during acceleration[52]. Otherwise all electrons would be pushed out. There will be no balanced or stable acceleration. The balance condition can be expressed as[52]

$$a_L(1 + \eta)^{1/2} \sim \left(\frac{n_0 D}{n_c \lambda} \right). \quad (2.70)$$

Here, a_L is normalized laser field amplitude, η is the reflecting efficiency. D and n_0/n_c are target thickness and normalized target density, respectively. The balance condition can be written in a normalized form,

$$a_L < \left(\frac{2\pi D n_0}{n_c \lambda} \right). \quad (2.71)$$

LP-RPA shows a bright future. Higher transformation efficiency and narrow-band spectrum make nuclear reaction and cancer treatment possible. The conditions for

its realization are not harsh, and the energy spectrum of monoenergetic ions can be observed theoretically under different laser conditions[52, 54, 55]. But there are still some challenges, as follows

(1). Laser group velocity reducing

For a Gaussian pulse, the laser spot size evolves according to $r_s = r_0(1 + (z/Z_R)^2)^{1/2}$, where r_0 is the minimum radius at $z = 0$ and Z_R is the corresponding Rayleigh length. The axial group velocity of the laser pulse is reduced by $v_g \simeq c \cdot \cos(\theta) \simeq c(1 - \theta^2/2) < c$ [56], where $\theta = r_0/Z_R$ is the laser diffraction angle with respect to the laser propagation axis. The laser diverges rather quickly for the tightly focused laser pulses after passing through the focus. Hence, the axial group velocity is smaller than that of the laser vacuum speed. And, particles cannot be accelerated to a velocity larger than the group velocity of the laser [57]. Because the group velocity plays a major role in laser-driven electron acceleration[56], so naturally modify the RPA[58].

In relativistic mirror concept, when the laser is reflected by a mirror moving with a relativistic velocity, the frequency of the reflected laser pulse is decreased by $(1 - \beta^2)/(1 + \beta^2) \approx 1/4\gamma^2$ for $\gamma \gg 1$, here β is the mirror velocity and normalized to the light speed in the vacuum. γ is the mirror Lorentz factor[59]. The energy transferred to the relativistic mirror is $(1 - 1/4\gamma^2)\varepsilon_{\text{laser}}$ in the relativistic mirror model, where v is the mirror velocity and $\varepsilon_{\text{laser}}$ is the energy of the incident laser pulse. When considering the reduction in the laser group velocity, the maximum attainable energy of particles is less than the value estimated by the relativistic mirror concept. The energy gain in this situation is closely related to the difference between the instantaneous group velocity, v_g , and the relativistic mirror velocity, v , which is approximately given by $\Delta\varepsilon \approx 2\gamma^2\beta(\beta_g - \beta)\varepsilon_{\text{laser}}$ [57]. Where $\beta_g = v_g/c$ and $v_g < c$ is the laser pulse group velocity as mentioned above.

(2). Transverse target expansion

Apart from the laser group velocity reduction, another problem arises when a small f-number focusing mirror (e.g., f/1) is used in the experiment. The intensity distribution near the focus undergoes a dramatic change in the transverse direction due to the significant divergence angle. Furthermore, the beam diverges rapidly after passing through the focal point, causing the thin foil to expand transversely and reduce the areal density of the foil. Thus making the target transparent for radiation and reducing the effectiveness of acceleration. As a result, the RPA process

is terminated prematurely [57].

(3). Rayleigh-Taylor type instability

A similar phenomenon in the astrophysical, Rayleigh-Taylor type instability usually occurs at the interface of two materials with different densities. For the sake of Rayleigh-Taylor type instability, the compressed thin plasma foil is torn into clumps in the interface and significantly broadens the energy spectrum of the accelerated ions [60, 61]. The instability perturbation is proportional to the time t and $t^{1/3}$ in the non-relativistic and ultra-relativistic limits, respectively. Especially in the ultra-relativistic limit, the perturbation develops faster with decreasing laser pressure and increasing ion mass [61].

2.5.3 Relativistic Induced Transparency (RIT)

Building high-power lasers ($I > 10^{23} \text{W/cm}^2$) and developing pre-pulse cleaning techniques remain challenges. In contrast, the so-called Breakout afterburner (BOA) mechanism predicts in simulation that it is the potential to achieve hundreds of MeV-level energy ions with laser intensities of $I \approx 10^{21} \text{W/cm}^2$ [62, 63]. The BOA mechanism is based on an ultra-thin target, comparable in size to the skin depth within the target. When the prepulse and the leading edge of the laser ionize the initial solid target, the hot electron plasma expands and the plasma density decreases. Relativistically induced plasma transparency, superpositioned with the above factors, causes the laser to penetrate the plasma. As a result, the resulting longitudinal acceleration electric field is significantly enhanced ($\approx 10^{13} \text{V/m}$) and co-moves with the ions. Further simulation research has shown that BOA is sometimes coupled as a post-accelerator for TNSA, further accelerating the ions. Finally, ions could be accelerated to several hundreds of MeV in PIC simulation as a quasi-monoenergetic bunch [64].

A related experiment during the same period confirmed that the thin foil becomes relativistically transparent during the laser-target interaction leading to strong volumetric heating of the volume electrons. Consequently, the increased electrostatic fields enhance acceleration and the maximum energy of C^{6+} ions up to 15 MeV/u [65]. Considering the ions accelerated by the longer laser pulse, 540 fs FWHM, PIC simu-

lation, and related experiments indicate the ions dramatically accelerate until the electron density reduces to the non-relativistic critical density in the expanding target. The ions are mainly accelerated to the highest energy by the peak intensity of the laser pulse[66, 67].

2.5.4 Coulomb Explosion Acceleration (CEA)

A double-layer target consisting front heavy ions and rear light ions can also produce quasi-monoenergetic ions in theory[68]. The incident laser pulse partially ionizes heavy ions and expels the electrons from the thin target. The remaining ions' background and the electrons create the quasi-static electric field in space, which leads to the light ions can be efficiently accelerated due to the Coulomb explosion. The optimum target parameter is no longer the thickness but the electron areal density[69]

$$\sigma = \frac{n_e l}{n_{cr} \lambda}, \quad (2.72)$$

where n_e and n_{cr} are the electron density and the corresponding critical density. l and λ are the target thickness and wavelength, respectively. According to the 2D PIC simulation[69], the optimum dimensionless areal density, σ_{opt} is

$$\sigma_{opt} \approx (3 + 0.4a) n_{cr} \lambda, \quad (2.73)$$

where a is the dimensionless amplitude. When the $\sigma < \sigma_{opt}$, the laser pulse energy is transmitted through the plasma slab. On the contrary, if $\sigma > \sigma_{opt}$, most of the laser pulse is reflected from the plasma slab. In both cases, a stable and effective Coulomb acceleration field in the rear of the plasma cannot be established. If assuming all electrons are expelled, the Coulomb acceleration field created by the remaining ion layer is

$$E = 2\pi e Z_i n_i l = \pi \sigma \frac{m_e c \omega}{e}. \quad (2.74)$$

If taking the focal spot size as the transverse size of the strong electric field, the energy of an ion with charge eZ_a and accelerated by the field can be estimated as

$$\varepsilon_{max} = 2\pi n_0 Z_a Z_i e^2 l r. \quad (2.75)$$

Here, r is the focal radius, and eZ_i is the average ion electric charge in the foil. The second light ions layer's thickness should be thin enough to form a narrow energy spectrum of the accelerated light ions[68].

Several research groups have investigated the interaction between laser-induced Coulomb explosions and clusters[70, 71, 72, 73]. The ion energy scaling for the cluster exhibits some differences. The energy of the accelerated ions depends on their original position, but the highest energy ions mainly originate from the surface of the cluster. The energy of the ions is inversely proportional to the cluster density, but linearly proportional to the laser power.

2.6 Enhanced Particle Acceleration Schemes

Optimizing energy spectrum and energy is an ongoing process. While various acceleration schemes have been proposed, some novel schemes based on optical or novel target methods has also emerged as needed. In this section, we will provide a brief overview of various technical solutions.

2.6.1 Optical Methods

Increasing the laser intensity and optimizing parameters are fundamental practices, as high-power lasers are used for particle acceleration. However, the material damage threshold limits the intensity of the laser. To enhance the laser intensity, one must increase the size of the optical element. Laser pulses must travel in vacuum after being compressed by a compressor. Using large-size, high-quality, precision optics

in the system results in high construction costs and post-maintenance expenses. To overcome these limitations, a series of new plasma-based optical elements[74, 75] or novel concepts[76, 77] have been proposed to allow manipulation of unprecedented laser intensities. Among them, the plasma mirror[78, 79] is the most mature and practical solution. The proposition and successful application of the plasma mirror in experiments have significantly improved the contrast of the laser. The laser temporal contrast mainly affects the isolation of the ion spectrum[80]. Some optimization schemes are based on existing laser systems, such as double pulses[81, 82] or a two-stage acceleration process[83]. These schemes significantly improve the cut-off energy of protons and the laser-proton energy conversion efficiency.

2.6.2 Novel Target Methods

Another technical path is to deposit more laser energy into the plasma by the optimize absorption through careful target design. In principle, the aforementioned acceleration mechanisms are based on micrometer or nanometer flat targets. Some exotic targets with unique geometries have been proposed, for example, the flap-top cone targets[84], the double-layer composite target[85], and the PMMA hollow spheres[86]. Owing to the particular geometric design that guides the super hot electrons to the flat top of the cone, the maximum energy of the proton beam produced by the flat-top cone target scheme is more than 2.4 times that of ordinary flat targets[84]. Similar maximum energy enhancements have also been observed using nanowire targets due to a stronger hot electron yield, both in density and temperature[87]. By combining the underdense plasma layer with a nanometer-thin foil, the energy of C^{6+} up to 50 MeV/u, which is attributed to the ejected carbon ions acquire the acceleration by the enhanced sheath field established by the super-ponderomotive electron flow[85]. For the mass-limited targets, the lateral diffusion of hot electrons at the target edge can be limited by reducing the transverse target size, producing proton spectra with a reproducible monoenergetic peak[37, 88, 89]. In addition to these experiments, some ideas for improving the energy of accelerated protons are proposed and indicated by PIC simulations[90, 91, 92]. These optimization schemes will be implemented successively in the near future.

Experimental Description and Diagnostics

“ *Nothing in life is to be feared, it is only to be understood. Now is the time to understand more, so that we may fear less.*

— Marie Curie

This chapter mainly focuses on the laser infrastructure and detectors involved in the experiment. Firstly, it introduces the technical routes of the high-power femtosecond laser system and the single longitudinal mode nanosecond laser system. Then, a brief introduction is provided for the diagnostic system used in the experiment. Finally, the serrated aperture is discussed, including the relevant simulation results.

3.1 JETi200 Laser System

The Jenaer Titanium:Sapphire 200 Terawatt (JETi200) laser system is based on a Ti:sapphire gain medium and is passively mode-locked, achieving peak power levels of up to 300 TW. The laser pulses have an energy of 7.5 J before compressor and a duration of 17 fs. In order to investigate high harmonics generation from solid surfaces and ultra-thin foils particle acceleration schemes, the temporal intensity contrast of the laser pulses must be high enough to suppress any pre-plasma generation before the main pulse arrives at the target. The whole laser system is equipped with a double chirped pulse amplification (CPA) scheme. The seed pulse is first amplified to 1 mJ and compressed to 30 fs. Then, nonlinear optical processes, namely cross-polarized wave (XPW) generation, are utilized to broaden the spectrum of the laser pulses and increase the temporal contrast. After that, the pulses are temporally stretched and further amplified in the second CPA stage. The

spectral is transform-limited with a width of more than 100 nm, and the energy is around 7.5 J. Finally, the stretched pulse is once again compressed to 17 fs in the main compressor. The amplified spontaneous emission (ASE) level is around 10^{-11} and the pre-pulse level is below 10^{-8} . To further improve the temporal contrast, a self-built plasma mirror (PM) is used to suppress ASE and pre-pulse, which can achieve a final ASE level of below 10^{-13} and a pre-pulse level below 10^{-10} before the main pulse at 10 ps. An adaptive mirror is installed after the plasma mirror chamber to pre-compensate accumulated wavefront aberrations caused by the laser chain and beamline. Using a glass substrate off-axis parabolic (OAP) mirror, the laser pulse can be focused to intensities greater than $10^{21} \text{W}/\text{cm}^2$ with a $1.7 \mu\text{m}$ FWHM. Fig.3.1 shows the high-dynamic range distribution of the focal spot with the optimized wavefront and the unoptimized wavefront. The FWHM of the focus contains 45% energy after wavefront optimization.

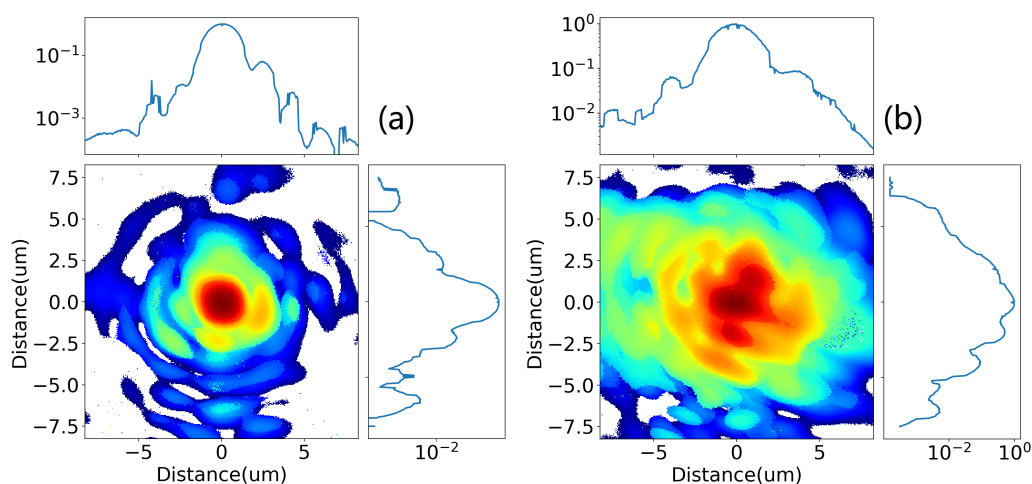


Fig. 3.1: High-dynamic range distribution of the focal spot with log scaling. (a) is the focal spot after the wavefront optimization. (b) is the focal spot before the wavefront optimization. The RMS values of the wavefront are 0.04λ and 0.2λ , respectively.

3.1.1 Laser Contrast

The successful application of CPA has opened the door for high-energy, ultrashort laser experiments, one of the important parameters is laser contrast. The temporal contrast of a laser system is a crucial parameter for high-power laser systems. Otherwise, the target is destroyed, and a pre-plasma is formed before the main

pulse arrives, significantly changing the essence of the interaction[93]. The reasons that affect temporal contrast mainly include amplified spontaneous emission (ASE), pre-pulses, and coherent contrast (exponential shoulder before the main pulse). Fig.3.2 shows the typical temporal distribution of laser intensity.

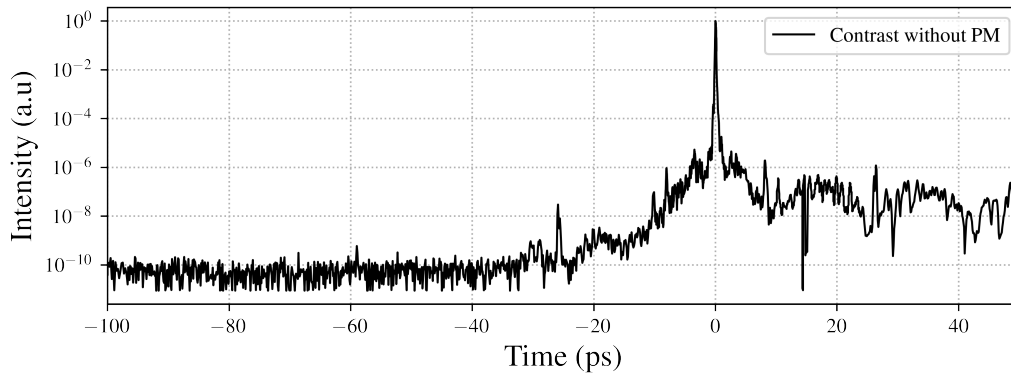


Fig. 3.2: The JETi200 contrast was measured within a hundred picoseconds by the Sequoia third-order cross-correlator.

Amplified Spontaneous Emission (ASE):

ASE mainly constitutes the nanosecond-scale pedestal before the main pulse, and it mainly originates from cavities present at the front end of a laser system. When the ASE and the main pulse are extracted at the same time, the worst thing is that the ASE will be amplified in the subsequent amplifier chain. The ASE can be controlled by a fast Pockels cell and reduced to a few ns level. Otherwise, the spectrum of the main pulse will be cut. The ASE level usually cannot directly destroy the target due to its low intensity. The drawback of the presence of ASE is that the energy of the ASE can even be comparable to that of the main pulse due to its nanosecond-scale duration[94]. It acts as a parasite stealing a significant fraction of the energy from the amplification chains. In the JETi200 laser system, the ASE is very low and reaches $\sim 10^{-11}$ level.

Pre-pulse:

The pre-pulse in the temporal intensity chain is many orders of magnitude weaker than the peak of the main pulse, but it can trigger pre-plasma formation directly if not properly suppressed. The resulting pre-plasma can effectively absorb more energy from the ASE through collisional absorption, which can cause serious damage to the target. The pre-pulse can be caused by various factors such as leakage/reflected pulses from previous round trips, imperfect compressor recompression, mirror post pulses to pre-pulses in the amplifier, and higher order phase distortions induced by

the amplifier.

Coherent contrast:

Coherent contrast appears as an exponentially-rising pedestal within a few tens of picoseconds before the main pulse. It is impossible to separate it from the main pulse; in other words, it is a part of the main pulse peak. In contrast to ASE and pre-pulses, the coherent contrast carries a large amount of energy and can easily lead to pre-plasma denting. Moreover, the actual pulse is not a perfect Gaussian distribution due to the existence of coherent contrast. Scattering from the diffraction gratings in the stretcher is the main source of the coherent contrast, and replacing the lower-quality gratings resulted in an order-of-magnitude improvement in the coherent contrast [95]. Fig. 3.3 shows the typical coherent contrast in the JETi200 system, and the coherent contrast is reduced by two orders of magnitude at -150 fs.

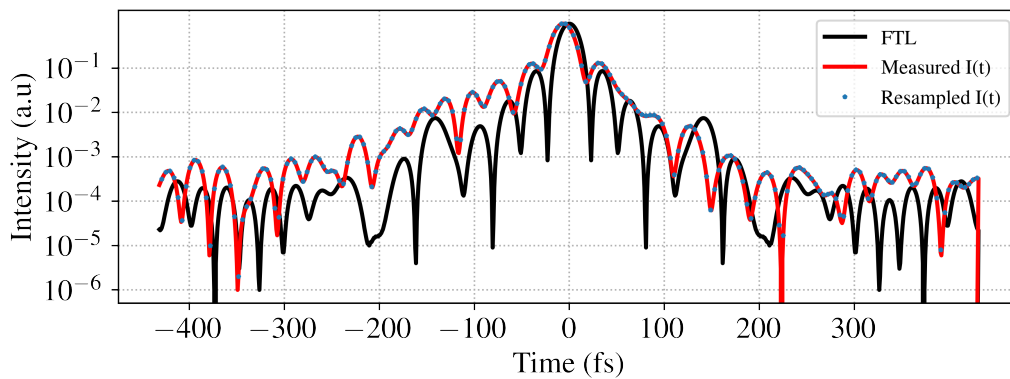


Fig. 3.3: The JETi200 contrast was measured within several hundred femtoseconds by the Wizzler. High-contrast lasers can reduce pre-expansion of the solid target and target deformation in the hundreds of femtoseconds before the main pulse peak arrives.

In the field of ultra-intense lasers, laser pulses with intensities exceeding $10^{22}\text{W}/\text{cm}^2$ have been generated[96]. However, the damage threshold of common solids is only $10^{12}\text{W}/\text{cm}^2$. Therefore, it is necessary to improve the temporal contrast as much as possible. Cross-polarized wave (XPW)[97, 98] and Optical Parametric Chirped Pulse Amplification (OPCPA) technologies have been well-established for the ASE and pre-pulse suppression of ultrashort pulses in high-energy laser systems. However, regarding coherent contrast research and optimization, there are still few related studies.

3.1.2 Plasma Mirror Energy Efficiency

Various methods have been presented above to improve temporal contrast before pulse compression without causing any damage to components. An alternative approach is the plasma mirror (PM) operated after the pulse compressor. The PM is a device for suppressing the ASE and pre-pulses of high-energy ultrashort pulses[78, 99, 100]. The PM operates based on the ultrafast ionization of the incident laser. One laser pulse is focused on a flat glass substrate positioned before the real focus. The relatively low intensity at this position prevents the ASE and pre-pulses from triggering surface plasma, and most of their energy passes through the transparent glass substrate. When the exponentially-rising pedestal appears within a few tens of picoseconds before the main pulse, an immediate increase in energy is sufficient to ionize the substrate and form an overdense plasma in a few cycles. Subsequent main pulse and post-pulse are reflected off specularly. The produced

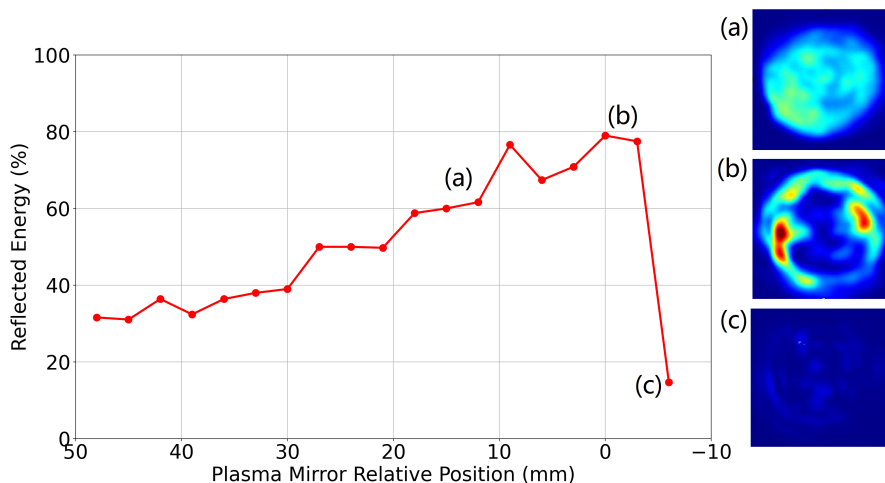


Fig. 3.4: Reflected energy as a function of the relative positions of PM. (a) - (c) show different near-field distributions in different PM positions. (c) is the position that PM is near the focal point.

overdense plasma remains a flat, metal-like mirror with good optical quality and high reflectivity to the later main pulse. Reflections of the ASE and pre-pulses are mainly determined by Fresnel reflectivity before the plasma shutter is formed. To reduce the reflection of the unwanted ASE and pre-pulses, the glass surface is generally coated with an anti-reflection (AR) film. The incident light is generally S polarization (parallel to the glass). For P polarization, the electrons inside the overdense plasma will be drawn out and pushed back during reflection, emitting high-order harmonic

radiation. If the incident laser is circularly polarized, the outgoing beam will change to elliptically polarized due to the different absorption rates between S- and P-polarization. Fig.3.4 shows the measured plasma energy efficiency in JETi200, (a) - (c) show the laser near-field profile after the plasma mirror reflection. (c) is the case when the PM is close to the focal point. If the PM position is too close to the focus, premature plasma expansion leads to an inhomogeneous intensity distribution in the reflected beam. On our system, plasma mirror energy efficiency is around 65% with S-polarization.

3.2 Q-Smart Laser System

The Q-Smart laser system is a compact pulsed Nd: YAG laser equipped with a single longitudinal mode module. The laser is used to detect the pre-plasma evolution in the experiment. The repetition rate is 10 Hz, and the maximum output energy is more than 240 mJ at the fundamental wavelength. The pulse duration is about 6 ns, long enough to detect ps-ns scale plasma expansion processes. It is equipped with two frequency-doubling crystals, 532 nm and 355 nm, respectively, and can detect different plasma critical densities. An outstanding feature is that the Single Longitudinal Mode (SLM) module makes the laser output extremely stable in time, reducing the laser's spectral bandwidth to 0.005 cm^{-1} ($5.66 \times 10^{-4} \text{ nm}$), increasing the coherence length, and providing a smooth temporal profile without mode beating. For a multi-mode laser, there are many laser modes in the resonators, leading to the competition and beating of the various modes for stored energy of the active medium, which are not repeatable from shot to shot. From a spectral perspective, each longitudinal laser mode has a slightly different wavelength (e.g., $\Delta\lambda \approx 10^{-4} \text{ nm}$ for adjacent modes), which when overlapped in time interferes with other modes, producing a strongly modulated pattern. Such pulses consist of many uncontrollable and periodic spikes. However, when an ultra-narrow seed is injected into the resonator of the multi-mode laser, in that case, the wavelength of the seed dominates, and other wavelengths are significantly suppressed because the strong injected seed takes all the energy from the gain medium. This type of laser is called an SLM laser, and its most obvious performance characteristic is that the output profile is

very smooth in time. Fig.3.5 is the intensity-time distribution of SLM laser pulse measured by streak camera.

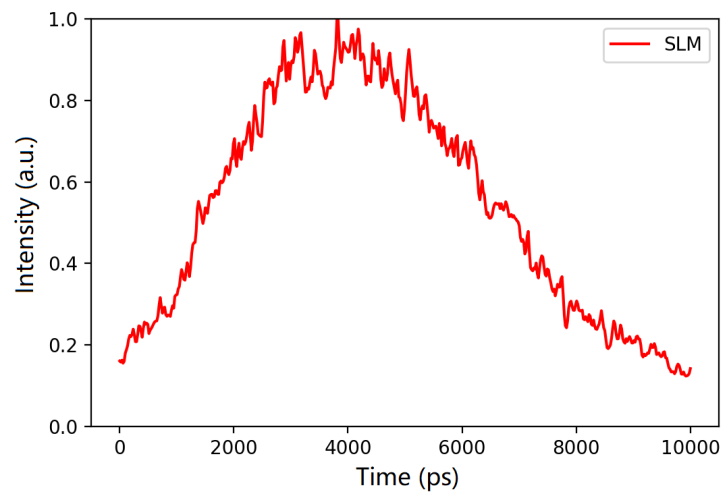


Fig. 3.5: Streak camera with a 10 ns sweeping time was used to measure the pulse intensity-time distribution, the time resolution was about 100 ps.

3.3 Diagnostic System

3.3.1 Streak Camera

Streak Camera (SC) is an ultra-fast instrument for measuring the variation of light intensity with time. Typically, its time resolution is on the order of picoseconds, and the fastest time resolution has broken through to the femtosecond level[101]. Additionally, based on streak cameras, one can increase the detection rate to 70 trillion frames per second[102]. The basic principle of the camera is shown in Fig.3.6. The light to be measured passes through a slit and forms a 1D image on the photocathode of the streak tube. The photocathode converts the light information into electrons by the photoelectric effect. Then these electrons are accelerated by the accelerating electrode, flying to a Micro-Channel Plate (MCP). High-speed and high-voltage are applied to the sweep electrode to deflect these electrons in the vertical direction during the drift process. Electrons hit the MCP at different positions. The MCP amplifies the incoming electrons and directs them to the phosphor screen,

where they are converted back into light. The whole streak tube is a vacuum tube that includes the photocathode, accelerating electrode, sweep electrode, MCP, and phosphor screen. Finally, a normal CCD records the light information from the rear end of the streak tube.

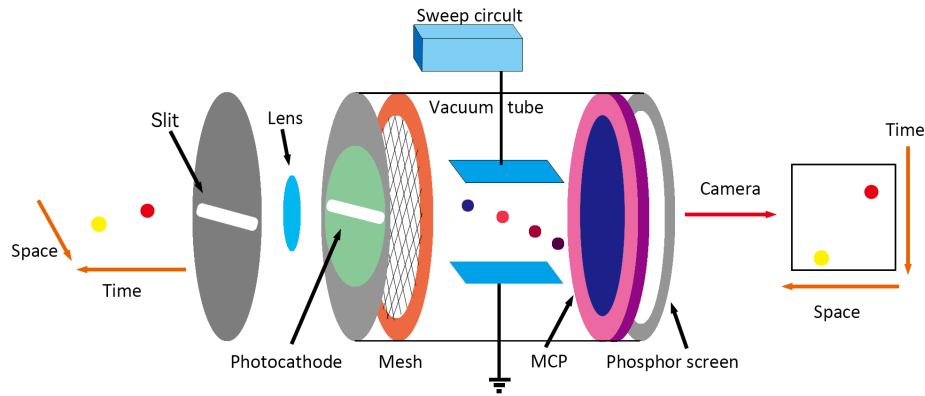


Fig. 3.6: The light pulse is focused onto the photocathode of the streak tube through the slit, where it is converted into electrons proportional to its intensity. These electrons are accelerated and conducted toward the phosphor screen while a high-speed voltage, synchronized with the incident light, is applied. The electrons are rapidly swept from top to bottom and hit the phosphor screen to produce an optical image. Finally, the camera outputs an image.

SC has many outstanding advantages as an ultrafast detector, including a very high dynamic range, relatively wide detection wavelength range, and excellent time resolution. The slit size of the SC, the sweeping speed, and the number of MCPs mainly dominate the time resolution of the streak tubes. Space charge effects in the photocathode-to-mesh region and the postanode electron drift region become significant, causing the electron pulse broadening even for a subpicosecond electron pulse[103]. Our streak camera is the HAMAMATSU C5680, equipped with an ORCA-Flash 4.0 C13440-20CU digital CMOS camera. Fig.3.7 shows the response curve of the SC to a 25 fs laser pulse under various sweeping times. Here, the slit size is about 40 μm , and the MCP gain is 30.

The time resolution of the streak camera can be evaluated by the output signal (FWHM) of the incident pulse light when the pulse light is short enough for the time resolution of the SC. Assuming the time resolution of the SC is T_s , the FWHM of the

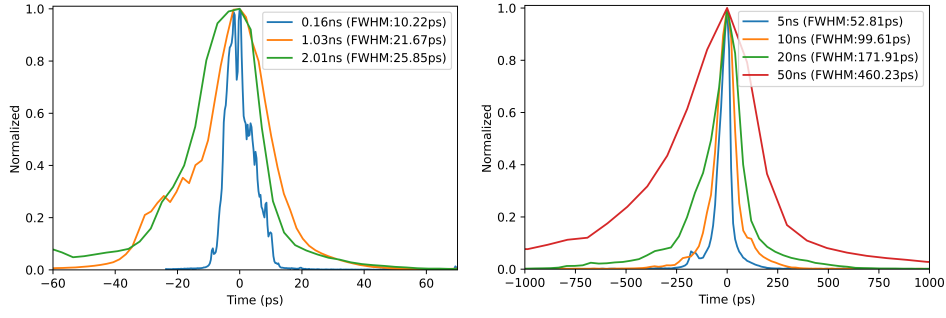


Fig. 3.7: The response curves of the streak camera to a 25 fs laser was measured at various sweeping times using a 40 μm slit. The sweeping time of the streak camera ranges from 0.16 ns to 50 ns, with the FWHM of the corresponding output image enclosed in brackets.

incident light is T_p , and T is the FWHM of the output image from the streak camera. The time resolution is as follows¹:

$$T = \left(T_s^2 + T_p^2 \right)^{1/2}. \quad (3.1)$$

Considering the ultrashort pulses used here, the temporal resolution of the streak camera is $T_s \approx T$. The commonly used sweeping times in the experiment are 1 ns and 2 ns, the corresponding time resolutions are 21 ps and 26 ps, respectively.

3.3.2 Magnetic Spectrometer Design

Within the framework of the project, a magnetic spectrometer was designed to diagnose the energy spectrum of charged particles. In principle, a magnetic field is the most effective way to change the direction of particles. A magnetic field of 1 Tesla and an electric field of 300 MV/m have the same bending power, but the latter is not feasible in a vacuum. The breakdown field strength of the vacuum is only 20 - 40 MV/m, depending on the electrode shape. If a particle with charge q and mass m moving with a velocity \mathbf{v} in a magnetic field \mathbf{B} experiences the Lorentz force, $\mathbf{F} = q(\mathbf{v} \times \mathbf{B})$. The velocity components are written as the time derivative of the positional components, and the Lorentz force can be written as a second-order ordinary differential equation (ODE):

$$\frac{d\mathbf{r}}{dt} = \mathbf{v} \quad (3.2)$$

¹Instruction manual for universal streak camera C5680

$$\frac{d^2 \mathbf{r}}{dt^2} = \frac{q}{m} \left(\frac{d\mathbf{r}}{dt} \times \mathbf{B} \right) \quad (3.3)$$

where the left-hand side of the equation is Newton's second law, where $\frac{d^2 \mathbf{r}}{dt^2}$ is the acceleration of the particle written as the second derivative of the position with respect to time. The magnetic force is always perpendicular to both the magnetic field vector \mathbf{B} and the velocity component \mathbf{v} that is perpendicular to the magnetic field vector \mathbf{B} (following the right-hand rule):

$$\mathbf{v} \times \mathbf{B} = (v_y B_z - v_z B_y) \mathbf{i}_x + (v_z B_x - v_x B_z) \mathbf{i}_y + (v_x B_y - v_y B_x) \mathbf{i}_z \quad (3.4)$$

By decomposing the vectors, the above formulas can be reduced into three sets of two first order ODE's:

$$\begin{aligned} \frac{dx}{dt} &= v_x \\ \frac{dv_x}{dt} &= \frac{q}{m} (v_y B_z - v_z B_y) \\ \\ \frac{dy}{dt} &= v_y \\ \frac{dv_y}{dt} &= \frac{q}{m} (v_z B_x - v_x B_z) \end{aligned} \quad (3.5)$$

$$\begin{aligned} \frac{dz}{dt} &= v_z \\ \frac{dv_z}{dt} &= \frac{q}{m} (v_x B_y - v_y B_x) \end{aligned}$$

Tracking the trajectory of charged particles involves an integration process. Numerical methods such as the Euler and the Runge-Kutta methods can be used to find approximate solutions for the second-order ordinary differential equation (ODE) that describes the motion of charged particles in a magnetic field. However, for scientific purposes, the Euler method is less accurate than more complex methods such as the Runge-Kutta method, even when using the same step size. This is because Euler's method is unstable and prone to overshooting, which are known issues. The Runge-Kutta method is one of the most widely used numerical methods for solving ODEs. It is considered reasonably efficient in terms of computation time, and its fourth-order approximation provides decent accuracy.

To design the magnetic spectrometer, a program was written using the fourth-order Runge-Kutta computational method to track the trajectory of charged particles in an

inhomogeneous magnetic field. The program varies the time step so that each ion moves a fixed distance in a single step, typically one grid unit. The local magnetic field is calibrated at each step, and Ansys is used to calculate the magnetic field distribution. The charged particle trajectory tracking program mainly consists of three parts. Namely, particle source, 4th Runge-Kutta solver, and statistics module. The program considers particle 3D velocities, positions in space, and relativistic corrections, which can simulate the entire trajectory of the charged particle from the particle source to the image plate. Particle source is based on the Monte Carlo method and can simulate particles with different speeds, positions, and exit angles. The magnetic field is an external input based on the results of Ansys. The magnet model is shown in Fig.3.8.

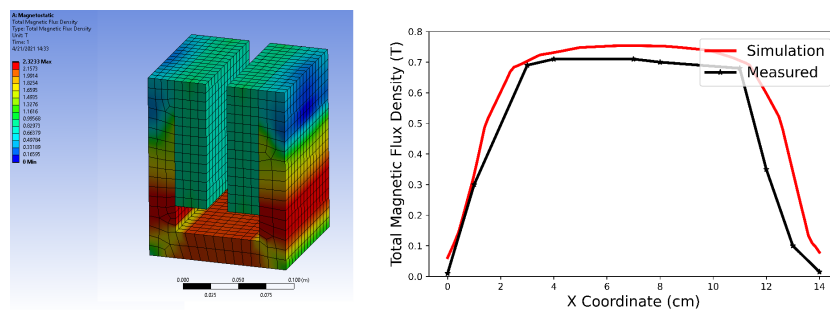


Fig. 3.8: The magnet model used by Ansys is shown on the left, while the comparison between the simulated and measured magnetic field distribution along the gap is presented on the right. The magnetic field distribution, including the fringe effect, was measured using a Hall sensor.

The spectrometer is designed to measure both ions and electrons simultaneously. The magnet slit is located 90 cm away from the laser interaction point and is only 1 mm high and 2 cm wide, resulting in a collection angle of approximately 24 mrad. A pair of neodymium magnets deflect the energetic ions and electrons. Two imaging plates are positioned behind and above the deflection magnet to collect the positive ions and negative electrons, respectively, with distances of 33 cm and 7.5 cm. The spectrometer can detect proton energies as low as 2.0 MeV and electron energies as low as 5.0 MeV. Fig.3.9 illustrates the trajectory of particles with different energies.

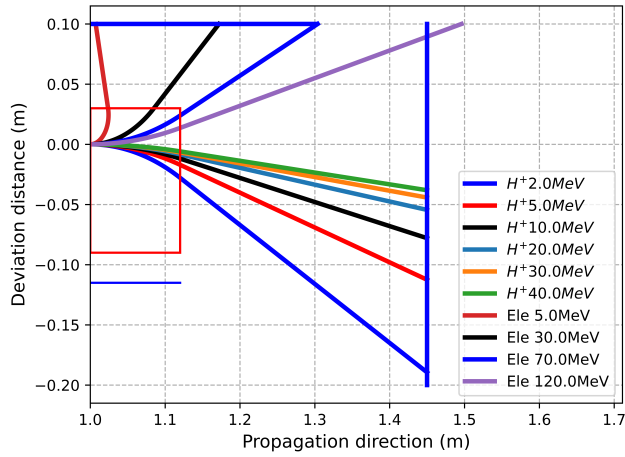


Fig. 3.9: The trajectories of protons and electrons with different energies after passing through the deflection magnet. The magnet is indicated by a red box, and the actual size of the imaging plate is represented by horizontal and vertical blue lines.

3.4 Serrated Aperture Design

One of the essential requirements for laser systems in the particle acceleration research field is ultra-high power and the best achievable focus quality. The beamline of the Terawatt laser system is usually several tens of meters long. However, the beam propagation length of Petawatt systems can reach hundreds of meters. Long-distance beam transmission, such as in a long multipass amplification path, can lead to unwanted diffraction effects that harm the amplification system and finally affect the focus quality. To overcome this issue, a serrated aperture system was proposed for the Nova laser system in 1978[104], and since then, it has been widely used in ultra-high power, ultra-short laser systems, especially in the femtosecond time domain. The introduction of serrated aperture systems does not cause significant space-time phase distortions into the femtosecond pulse, which could alter the pulse shape and duration [105, 106, 107]. In practical experiments, the serrated aperture system can precisely shape the beam edge and has the ability to split a large-sized beam into multiple beams to meet the experiment requirements. The serrated aperture system has been incorporated into the JETi200 laser system. The serrated aperture is installed in the front end of the laser system, where laser pulse energy levels are in the millijoule range. The spatial filter (including a pinhole) is installed in a vacuum pipe, avoiding filament formation caused by laser focusing in

the atmosphere. In this section, different shapes of serrated apertures are presented, including corresponding simulation and experimental results.

3.4.1 Simulation

A serrated aperture system mainly consists of a serrated aperture and a spatial filter (including a pinhole), as shown in Fig.3.10. A serrated aperture is a round or "2D" shapes with a serrated shape on the edge. It is fabricated from a thin stainless steel sheet. The sawtooth aperture imprints a periodic sawtooth pattern on the beam to modify the transmittance at the edge of the beam. The spatial filter is usually designed as a Kepler telescope with a pinhole in its common focal point. The telescope allows changing of the beam size. At the same time, the pinhole filters unwanted high spatial frequencies induced by the serrated aperture. These high spatial frequencies leave the average transmission function and maybe damage the end optical elements. To quickly determine the output of a serrated aperture

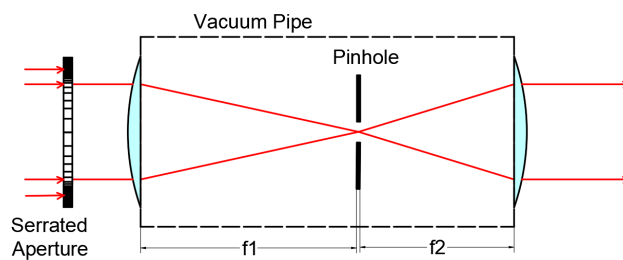


Fig. 3.10: A schematic of a serrated aperture system, consisting of a serrated aperture and a spatial filter, is presented. The spatial filter is located in a vacuum.

system, the entire system can be modeled using the following calculations[104]: First, the periodic serration pattern is imprinted on the beam, and a Fraunhofer diffraction calculation (Fourier transform) is performed for the beam just after the aperture. Next, the Fourier transform (far-field beam distribution) is multiplied by the spatial pinhole filtering function. However, the cleanup cannot be perfect since each spatial component is focused on a spot with a finite size. Finally, a second Fraunhofer diffraction calculation (inverse Fourier transform) is carried out to calculate the filtered beam at the output plane. These three calculations can estimate the dependence of the beam shape at the output plane of the serrated aperture system. However, they cannot provide additional amplitude-phase correction of

the input beam profile. Another method based on the solution of the parabolic equation gives the full phase and amplitude front of the beam at the spatial filter output, which makes it possible to determine the dependence of the phase and amplitude beam profile at the output [107]. Here, the serrated aperture system is

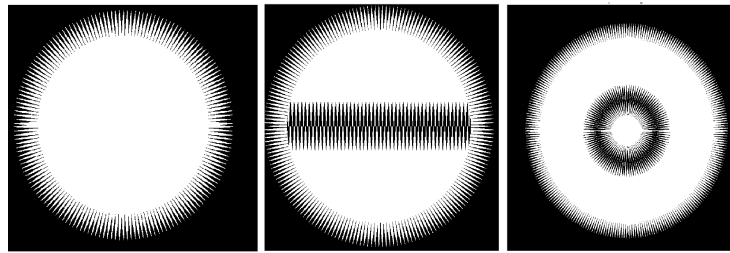


Fig. 3.11: Three different types of serrated apertures were modeled in the simulation.

modeled as mentioned above. It quickly determines the required parameters through the simulation. According to actual demand in JETi200 and further experimental requirements, three different shapes are designed, namely single ring, 2D, and double-ring, as shown in Fig.3.11. These serrated aperture models imprint various patterns on the beam to modify the transmittance at the edge of the beam, which is the operating principle of the serrated aperture. Here, the transmission function is super-Gaussian. The serrated aperture is 10 mm in diameter, and the height of each tooth is 0.6 mm or 0.8 mm. The tooth height-to-period ratio is a constant number six. The bad teeth are set in the horizontal direction on purpose to evaluate the influence of the wrong teeth on the results. It does not affect the final extraction of results in the vertical direction.

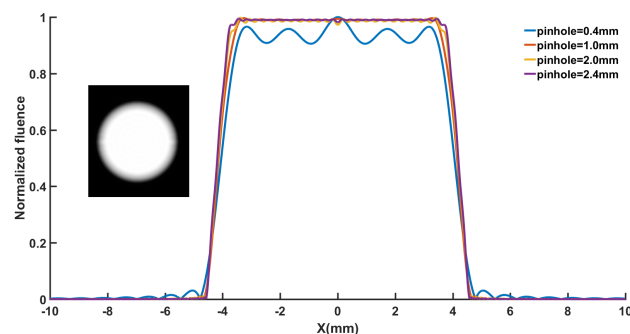


Fig. 3.12: Comparison of single ring aperture with different pinhole sizes. Inset for 2D light profile.

Consider the pinhole size to filter out the unwanted periodic component of the serration pattern in the beam. Here, five different pinhole sizes are chosen to

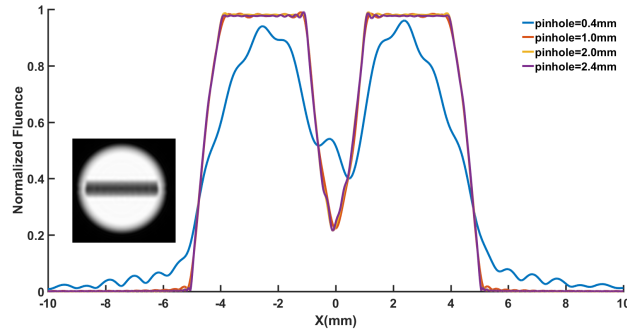


Fig. 3.13: Comparison of 2D aperture with different pinhole sizes. Due to the diffraction effect of light, the beam cannot be completely blocked. Inset for 2D light profile.

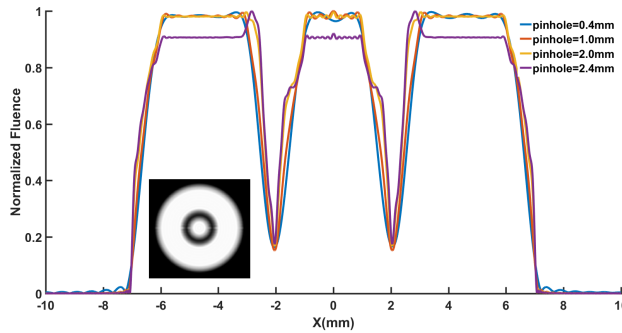


Fig. 3.14: Comparing different pinhole sizes for double-ring aperture. Due to the diffraction effect of light, the beam cannot be completely blocked. Inset for 2D light profile.

compare their influence on the results, as shown in Fig. 3.12 to 3.14. A lineout through the center of beam distribution and the edge profile shape is super-Gaussian. The results indicate that if the pinhole is too small, e.g., 0.4 mm, there are some diffraction ripples on the beam center. Conversely, a relatively large pinhole (e.g., 2.0 mm or larger) cannot remove the serration pattern from the edge of the beam.

3.4.2 Experiment

Fig. 3.15 shows a photograph of the serrated aperture utilized in the JETi200 laser system. The serrated aperture with a single ring and 2D shape is made by a thin stainless steel sheet, while the two-rings shape can be fabricated by metal deposition techniques in the future. A HeNe laser performs the testing work with a 632.8 nm central wavelength.

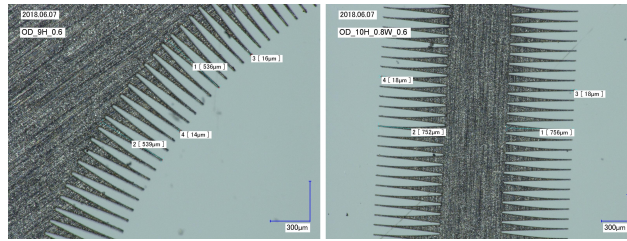


Fig. 3.15: A photograph of the JETi200 laser system’s serrated aperture is presented, with a cutting accuracy resolution of approximately 10 μm . The right image shows the central section of the 2D aperture.

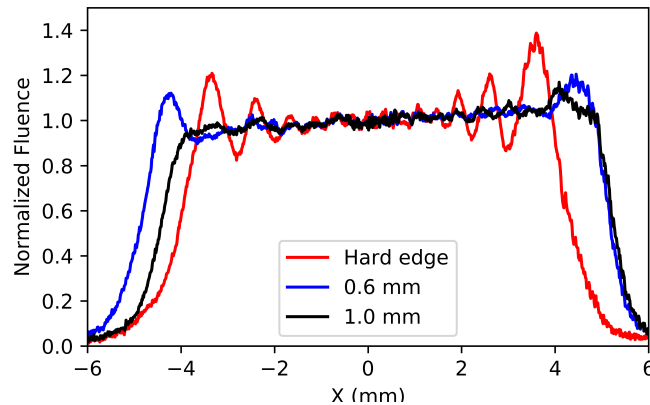


Fig. 3.16: Intensity profiles of the beam after passing through the serrated aperture system. In comparison, a hard edge causes significant ripples on the beam.

The experimental results in Fig. 3.16 to Fig. 3.18 compare the main parameters of the serrated aperture, i.e., the sawtooth height and pinhole size. Fig. 3.16 shows the result of a single ring shape, indicating that the hard-edge aperture cuts the beam and causes noticeable ripples. However, the serrated aperture can significantly reduce the ripples. The higher the sawtooth, the better the suppression of ripples, but it causes more energy loss.

As one of the serrated aperture’s apparent advantages, it does not introduce significant space–time phase[107]. 2D shape aperture, as shown in Fig. 3.17, can be used to separate the beam for pump-probe or multi-stage ions acceleration schemes. Here the height of the outedge sawtooth is fixed at 0.6 mm, only changing the width of the central rod and the height of the sawtooth on the rod. A wider rod can more significantly reduce the light intensity between the two parts, but it will not drop to zero due to the diffraction of light. Similar to a single ring shape, a higher sawtooth will result in greater energy loss but with the tradeoff of yielding improved effects.

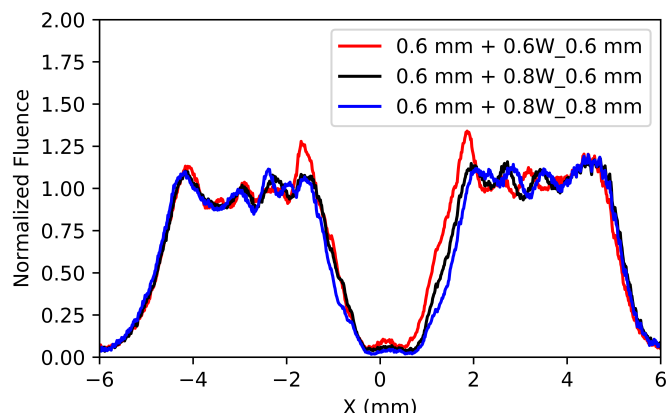


Fig. 3.17: After passing through the 2D shaped aperture, the intensity distribution was measured experimentally. The legend denotes the height of the outer sawtooth, the width of the central rod, and the height of the sawtooth on the rod, respectively.

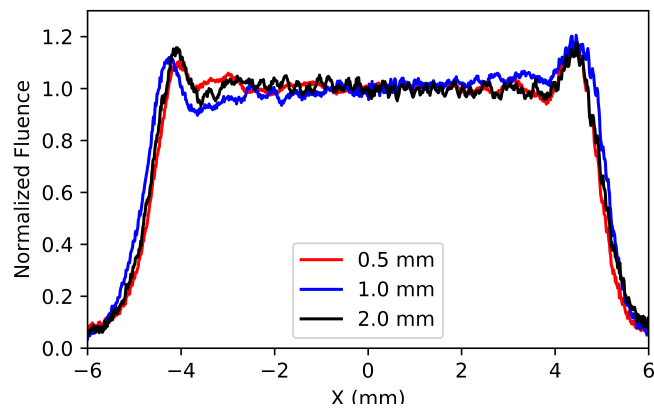


Fig. 3.18: Comparing the pinhole of different sizes, there is no obvious difference.

Fig. 3.18 demonstrates that the intensity profile remains almost unchanged for a reasonable pinhole size. However, it's worth noting that if the pinhole is too large, it loses its filtering effect, whereas if it's too small, focusing alignment becomes a challenge in vacuum pipes.

3.5 Summary

This chapter mainly introduces the experimental facilities and detectors. First, it discusses the JETi200 temporal contrast and the plasma mirror efficiency. High-contrast laser pulses are critical for laser ion acceleration. Then, single longitudinal mode laser and streak camera are briefly introduced. And the temporal resolution of the streak camera was measured. Finally, the design and measurement results of the magnetic spectrometer and serrated aperture are presented.

Ultra-thin Target Fabrication

” *A real scientist solves problems, not wails that they are unsolvable.*

— Anne McCaffrey

As shown in Chapter 5, nm-scale targets are significantly important for efficient proton acceleration. Fabricating nanometer-thin foils with well-controlled thickness and uniform surface requires advanced production techniques. Most of the experiments and simulations conducted so far have required an ultra-thin target, including plasma-based particle sources[67] and advanced high-order harmonic generation sources[108]. Various target fabrication methods have been established in recent years based on experimental demand and material science. Among these methods, diamond-like-carbon (DLC) foils are commonly mentioned in experiments and simulations due to their superior stability, endurance, and achievable minimum thickness (3 nm -5 nm)[109, 110]. One standard method for fabricating DLC foils is filtered cathodic vacuum arc deposition (FCVA), which is widely used for composite films, depositing metallic and protective coatings. For high-Z materials, such as gold foils, physical vapor deposition (PVD) can produce ultra-thin high-Z targets as low as 5 nm. In addition to FCVA and PVD, spin-coating is a common method for producing thin plastic foils in a wide range of applications. The fabrication process is relatively simple compared to FCVA and can produce target thicknesses from 5 nm to 600 nm. To investigate laser-driven particle sources in our institute/university and meet various experiment demands, we have established a target laboratory. Considering our experimental requirements, spin-coating is the most suitable method for us. This method can fabricate formvar with a relatively large thickness range and maintain highly uniform thickness quality. Formvar films are a kind of multi-species material having a wide range of applications in the industry, mainly used as electrical insulation for magnet wire and film grids for transmission electron microscopy (TEM)[111].

4.1 Spin-coating Method

Spin-coating method, due to its simple fabrication process and highly uniform surface widely used in different target laboratories[109, 112]. The production process mainly includes three steps:

1. Solution Preparation:

In the target laboratory, formvar powder or poly(vinyl) formal (#CAS 9003-33-2) is dissolved in 1,2-dichloroethane. The formvar molecular structure, as reported by Sigma-Aldrich company, is $[C_3H_6O_2]_n$ with a reported density of 1.23 g/ml [113]. 1,2-dichloroethane is a chlorinated hydrocarbon - a colorless liquid with a chloroform-like odor that is highly volatile and toxic, flammable, and possibly carcinogenic. All steps of the formvar solution preparation process are performed in the chemical hood. To obtain various thicknesses, we have tested several solutions of formvar with different mass concentrations. The formvar powder must fully dissolve in the solvent; otherwise, solid formvar particles may appear in the final thin target.

2. Film Fabrication:

For film fabrication, standard microscope glass slide serve as substrates, and it is placed on the spin-coater, which has variable revolutions up to 12000 rpm. A small amount of a specific solution is dropped on a rotation microscope glass slide and homogeneously spreads over a larger area through centrifugal forces. Evaporation of the solvent leaves a nanometer-thin solid film on the glass substrate.

3. Assembly and Mounting:

The adsorption force of the thin film with the glass slide is less than its buoyancy in water, so the nanometer target can easily be transported from the glass slide to the final target holder plate through the floating process. First, use a paper cutter to scratch each edge of the glass slide to detach the thin target from the glass slide. Otherwise, the nanometer target will be destroyed during the floating process. Then, slowly dip the glass slide into distilled water, as shown in Fig.4.1. Finally, a thin film is detached from the glass substrate and floats on the water surface. To take out the thin target, the target holder is moved up, emptying the water between the target holder and the thin film, as shown in Fig.4.1. Due to the liquidity of water, it is hard to take out the whole thin film due to its transparency. Some parts will be destroyed, especially for a thin film of less than 20 nm. One cross method, as shown in Fig.4.1,

can increase the thin film's survival probability. By leaving a small part of the film on the substrate through the connection between the film and substrate, the film's position on the water surface can be controlled. Even if one cannot see the thin film, one can still obtain a relatively complete thin film. In our laboratory, a 10 nm target can reach a size of 20 mm × 40 mm on the final target holder plate. Finally, the film

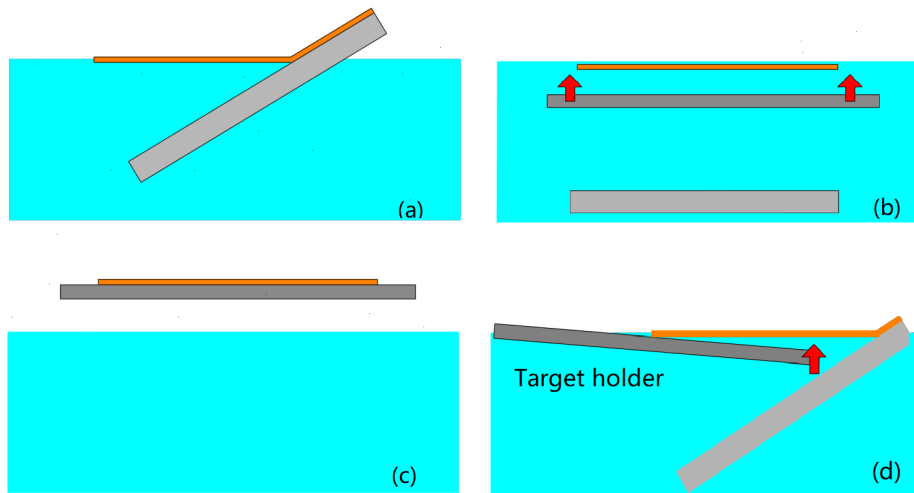


Fig. 4.1: (a) - (d) show the process of transferring a thin target from a glass plate to a target holder.

attaches to the holder and covers the holes of the target holder free-standing, as can be seen in Fig.4.2. Two sizes of target holders are used in practice for relatively thin film (less than 20 nm). The holes of the holder are 500 μm in diameter. A thick film attaches to the holder with a 1000 μm hole in diameter.

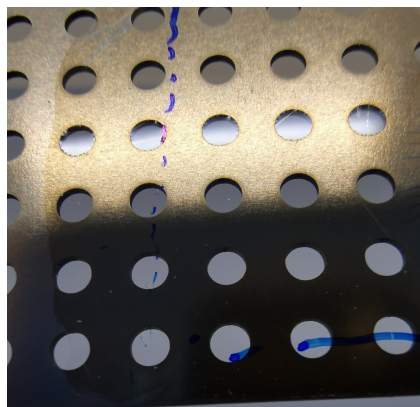


Fig. 4.2: A 30 nm film is on the target holder.

4.2 Characterisation of Thin Film

4.2.1 Thickness Measurement

A confocal microscope is used to characterize the thickness of thin films with various mass concentrations. In order to better characterize the thickness, measurements are taken at five different positions, with each position being measured at six distinct points, as shown in Fig.4.3. The five positions are separated by ~ 1.5 cm, and the 6 points are several microns apart. A total of 30 measurements are performed for each film. An example of a confocal microscope scan on a 9 nm formvar thin film is shown in Fig.4.4.

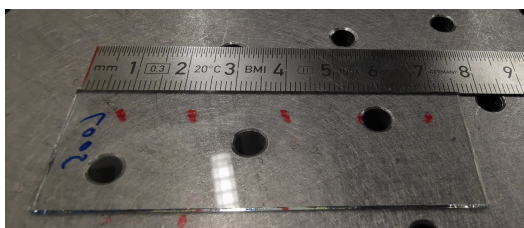


Fig. 4.3: The red points show the five positions that were measured.

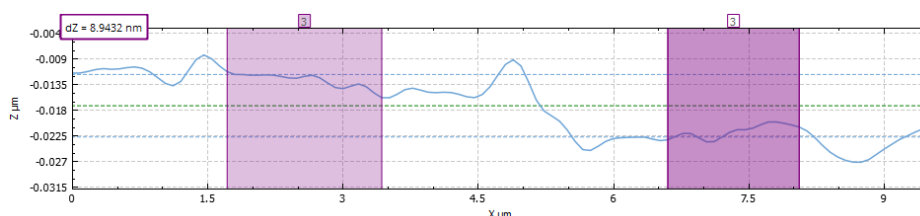


Fig. 4.4: A confocal microscope scan of 9 nm formvar film on a glass slide.

4.2.2 Mass Concentration

In chemistry, the mass concentration ρ is defined as the mass of a constituent m divided by the volume of the mixture V [114]. Mass concentration controls the final thickness of the thin film at a specific rotating speed. The thickness of the target against mass concentration as shown in Fig. 4.5. Table 4.1 summarizes the measured

average thicknesses and standard deviations of formvar. By fitting the curve, the following formula can be obtained:

$$\rho = 2.90^{-8}x^3 - 4.03^{-5}x^2 + 0.03x + 0.21.$$

Here, x (nm) is the expected thickness, and ρ (%) is the corresponding mass concentration, namely $\rho = \frac{m[\text{g}]}{V[\text{ml}^3]} \times 100\%$. Through this formula, the corresponding mass concentration can be calculated.

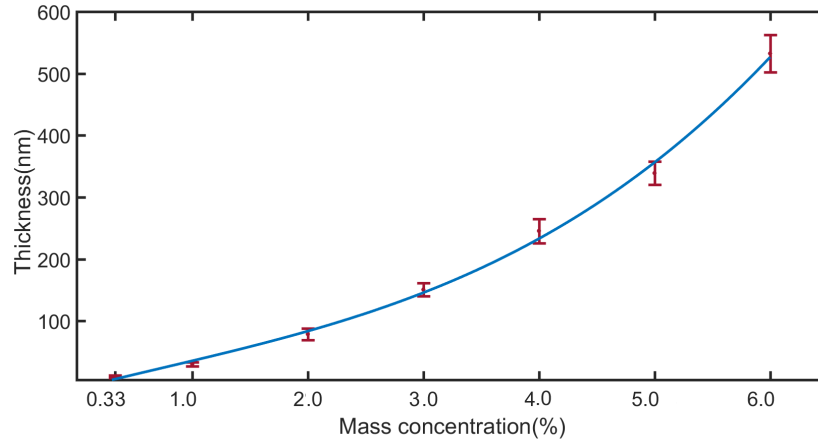


Fig. 4.5: The mass concentration of a substance directly affects the thickness of the resulting film.

Mass Concentration (%)	Liquid Volume (ul)	Rotation Speed (rpm)	Thickness (nm)	Standard Deviation
0.33	75	10000	10	1.97-2.05
0.5	75	10000	15	1.52-2.82
1	75	10000	32	3.16-4.00
2	140	10000	78	9.17-11.73
3	140	10000	150	10.42-15.16
4	160	10000	250	19.61-23.41
5	200	10000	340	14.35-26.15
6	200	10000	532	30.33-39.10

Tab. 4.1: For mass concentrations ranging from 0.33% to 6%, the average thicknesses and standard deviations of formvar were calculated. For thick targets, more liquid is required to make the target. Otherwise, the edges of the target will tear. But it will not affect the quality of the center part of the target.

4.2.3 The Effect of Rotation Speed

In addition to mass concentration, the rotation speed of the spin-coater is another crucial parameter affecting the film's thickness and quality. As shown in Fig.4.6 (a) and (b), at a mass concentration of 5%, the film's thickness produced at 6000 rpm and 8000 rpm fluctuates greatly compared to 10000 rpm and 12000 rpm. In actual experiments, thickness fluctuations can cause significant data fluctuations. Fig.4.6 (b) indicates that the effect becomes saturated when the speed reaches a certain threshold, which was over 10000 rpm in our case. Under a certain mass concentration, the faster the rotation speed, the thinner the film produced. When the size of the glass slide is not changed, the effective area ratio compared with the initial film size is reduced, leading to a reduction in the standard deviation of thickness across the film.

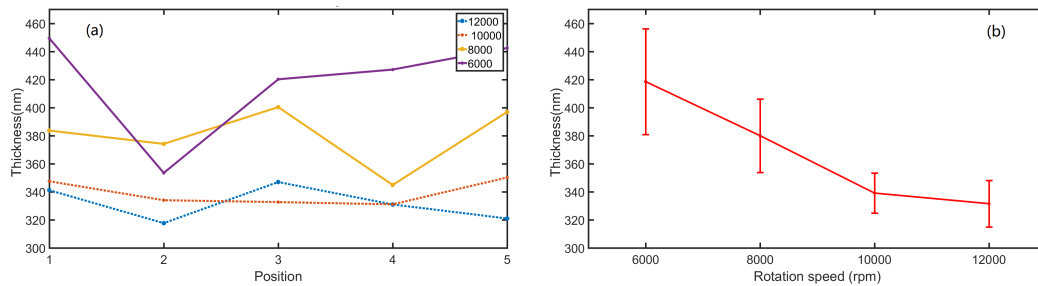


Fig. 4.6: (a) The forming thickness of the 5% solution varies significantly at different positions and speeds, with more significant fluctuations observed at lower speeds. (b) As the rotation speed increases, the thickness fluctuation gradually decreases until it reaches a saturation point.

4.2.4 Thickness Fluctuation

The microscope glass slide is 23 mm \times 50 mm. Usually, more than 80% thin films can be transported to the target holder by the floating process. It is necessary to determine the film thickness variable along the long side. As mentioned above, five positions are measured, and each position includes six measuring points. The result indicates, as shown in Fig.4.7, the thickness of the film is very uniform at different positions. For variable thickness, from 10 nm to 400 nm, the measurement is repeated multiple times and consistent results are obtained.

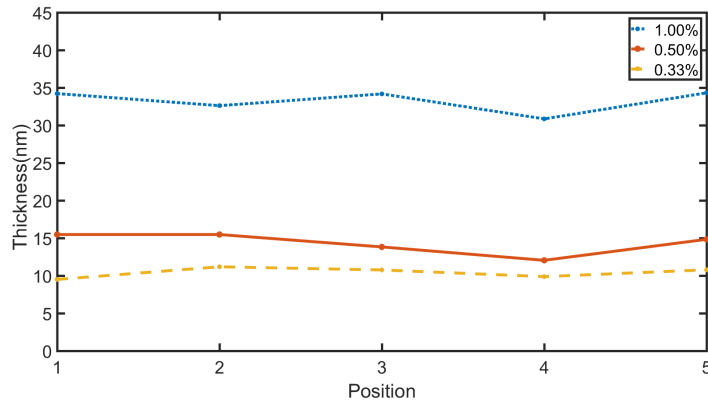


Fig. 4.7: Five distinct positions are measured for each thin film to compare its thickness fluctuation.

4.2.5 Storage

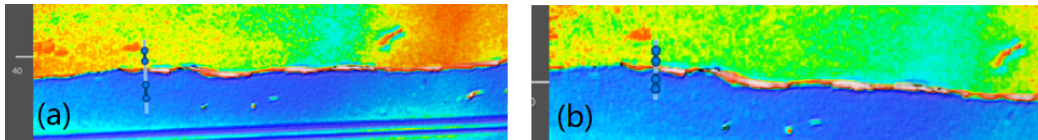


Fig. 4.8: To reduce measurement error, measure the same position on different days. (a) first day and (b) eighth day.

Storage is an interesting aspect of a thin film. The storage environment will cause slight changes in thickness. To compare their changes, the two films on the glass substrate are placed in different environments, $\sim 10^{-1}$ Pa vacuum and atmospheric environment. I tracked the changes in these films for two weeks. In order to reduce the measurement error, the following aspects are considered: First, as mentioned above, 30 points are measured in different areas each time, and the average value is obtained. One difference is the positions of these 30 measuring points are the same on different measurement days, as shown in Fig.4.8. Second, complete the measurement of the vacuum storage film within half an hour to reduce the impact of moisture adsorption in the air and then put it back into the vacuum. Fig.4.9 shows that the thin film stored in a vacuum is more stable than that stored in the atmospheric environment. It is worth noting that there is an unusual fluctuation on the eighth day in the thin film stored in the atmospheric environment. It had been raining for 48 hours before that day. This is because humid weather will cause more water vapor to be absorbed onto the target surface.

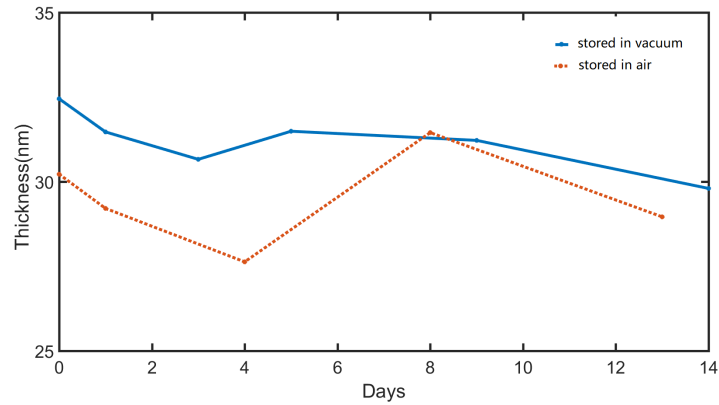


Fig. 4.9: The two films on the glass substrate are placed in different environments to compare their changes in 14 days. The wet weather leads to more water molecules being absorbed onto the target surface.

4.3 Laser-induced Damage Threshold

Laser-induced damage threshold (LIDT) for a material dramatically depends on the laser parameters used. Continuous wave (CW) lasers typically cause damage due to thermal effects, where the material absorbs the laser’s energy and causes the surface to melt. Pulsed lasers with a duration longer than $1 \mu\text{s}$ can be treated as CW lasers for LIDT discussions [115]. However, pulsed lasers (with a duration of $10^{-9} < \tau < 10^{-7}$ s) often cannot continuously heat the material to damage it. Instead, they generate a strong electric field that can cause dielectric breakdown of the material. For ultra-short pulses ($\tau < 10^{-9}$ s), various mechanisms such as multiphoton avalanche ionization become the main damage mechanism [116]. While the diamond-like carbon (DLC) film has been extensively studied [117, 118], including LIDT of DLC, research on formvar thin film is still scarce.

In this section, the damage threshold of the formvar thin film is investigated under irradiation with a 1064 nm wavelength and a 5 ns pulse duration. The parameters of the laser systems used in this study are summarized in Table 4.2. Two films, with 10 nm and 100 nm thicknesses, are subjected to single-pulse and multipulse (100 pulses, 10 Hz, 532 nm) irradiation, respectively. In the experiment, a thin target is irradiated with a single pulse or multiple pulses at various energy levels. The thin film is then examined under a microscope for any visible damage, with this process being repeated until damage is observed. The experiment is repeated 10 times at

Gain medium	Nd:YAG
Repetition rate (Hz)	1 - 15
Pulse duration (ns)	5
Wavelength and Energy (mJ)	
1064 nm	28
532 nm	12
355 nm	4
Energy Stability (shot-to-shot)	
1064 nm	±2.0%
532 nm	±3.0%
355 nm	±4.0%

Tab. 4.2: Summary of the Minilite laser systems used for LIDT measurement.

each energy fluence. The results, shown in Figs. 4.10 and 4.11, indicate different LIDTs for the two thicknesses under both single-pulse and multi-pulse conditions. Compared with the 10 nm film, the 100 nm film can endure relatively high energy fluence under both irradiation conditions. However, it is worth noting that LIDT decreases with increasing numbers of irradiations, with no exceptions for the 10 nm and 100 nm films.

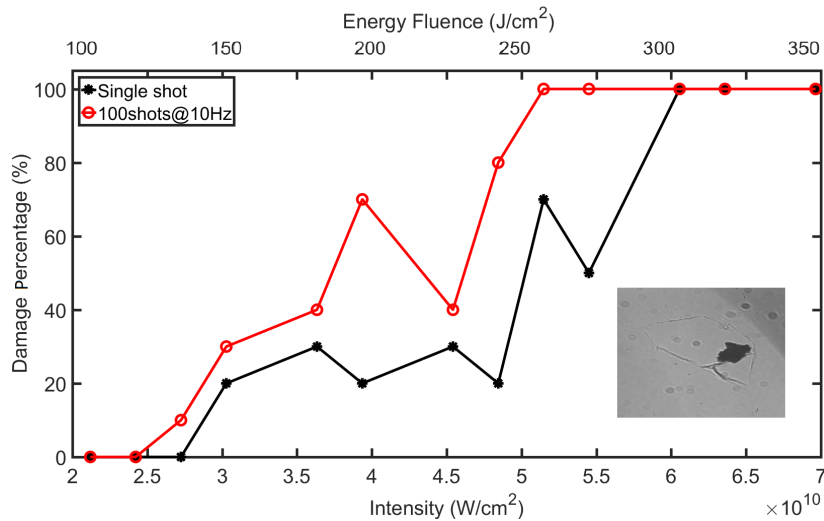


Fig. 4.10: The laser-induced damage threshold for 10 nm formvar. The inside picture indicates the destroyed hole on the surface.

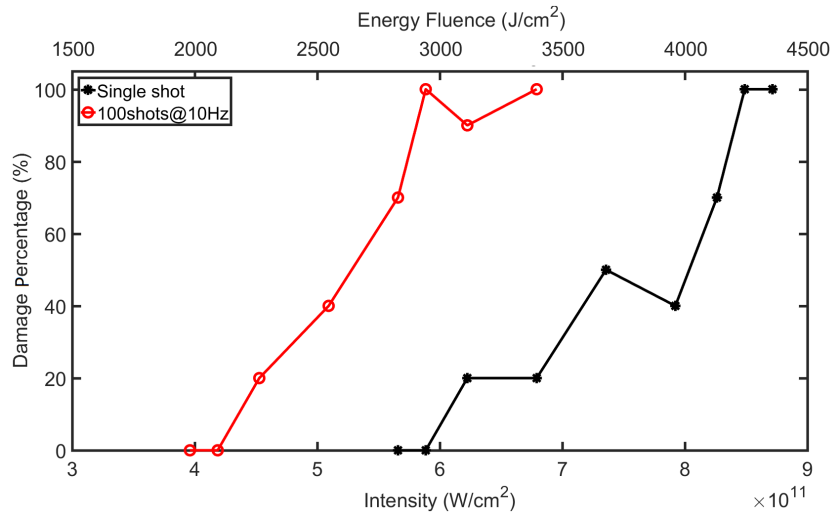


Fig. 4.11: The laser-induced damage threshold for 100 nm formvar.

4.4 Summary

A platform for fabricating and characterizing ultra-thin targets has been established at Helmholtz Jena. This platform has successfully produced formvar targets with thicknesses ranging from 8 nm to 400 nm, which are utilized in laser-driven particle acceleration experiment. Detailed investigations into the characteristics and parameters of the targets have been carried out, including assessing their damage threshold in nanosecond laser fields. The determination of the damage threshold can provide a reference for Chapter 6 near-critical density plasma diagnosis, helping to prevent the probe light from damaging thin targets.

Proton Acceleration with High Contrast Laser Pulses

“ *What you learn from a life in science is the vastness of our ignorance.*

— David Eagleman

This chapter presents the experimental results of laser-driven proton acceleration based on solid targets. In Sec.5.1, the experimental setup is introduced. In Sec.5.2, the dependence of the accelerated protons energy on the target thickness is investigated experimentally. Solid targets with various thicknesses are irradiated by lasers with either circular or linear polarization. Two-dimensional (2D) simulations aiming to explain the data obtained from the experiment are shown in Sec.5.3.

5.1 Experimental setup

The experimental results described in the dissertation were obtained at the JETi200 laser system. The specific parameters of the laser system are described in Section 3. The basic setup of a proton acceleration experiment is shown in Fig. 5.1. The main pulse is focused by a $f = 180\text{mm}(f/1.5)$ silver-coated off-axis parabolic (OAP) mirror. The main focal spot has a FWHM of $1.7 \mu\text{m}$ and an FWHM intensity of $2 \times 10^{21}\text{W}/\text{cm}^2$. The main pulse normal incidents the target, while a CCD positioned in front of the frosted glass records the transmitted light. The laser-accelerated protons pass through a small gap in frosted glass, and then they are deflected by a magnet based on their energy before being recorded by IP. The magnet is 90 cm away from the target, the magnet slit is 1.0 mm high and 2.0 cm wide. The solid angle of the magnetic spectrometer is about 0.40 msr. A multi-stage Al filter is placed before the IP to determine the energy range of the protons. For a detailed description of the multi-stage Al filter, see the Appendix:Multi-stage Al Filter.

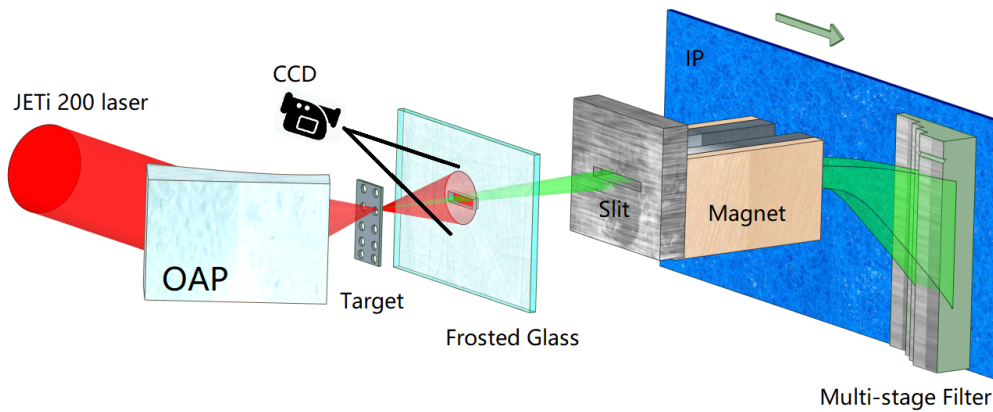


Fig. 5.1: One OAP focuses the main pulse on the target. The CCD records the transmitted light, while a magnet deflects the proton beam based on its energy before the IP records the proton data. The magnet is 90 cm away from the target. The magnet slit is 1.0 mm high and 2.0 cm wide. The IP is 33 cm away from the magnet. A multi-stage Al filter is placed before the IP to ensure that the proton signal is not interfered by heavy ions. The introduction and configuration of the multi-stage filter can be seen in Appendix: Multi-stage Al Filter.

5.2 Proton Acceleration Based on Solid Targets

5.2.1 Target Thickness Effect in Proton Acceleration

The Radiation Pressure Acceleration (RPA) mechanism holds great potential in producing efficient[119], monoenergetic proton beams, particularly in the Light Sail (LS) RPA regime. When a linearly polarized laser is incident normally on the target, electrons are driven by the $\mathbf{v} \times \mathbf{B}$ force with a frequency of 2ω (where ω is the driving laser frequency). The resulting electron oscillation across the laser-plasma boundary creates thermal electrons through the absorption of additional laser energy. However, research indicates that circular polarization achieves more efficient acceleration at a broader range of laser intensities. According to the RPA model[120], to optimize ion energies, an appropriate target thickness is crucial, balancing laser light pressure and electrostatic forces from charge separation. If the foil target is thinner than the

optimal thickness, all electrons will be expelled by light pressure and scatter in only a few cycles, terminating the acceleration process. For a circularly polarized laser pulse with a normalized amplitude of a_0 interacting with a thin foil of density n_0 and thickness L , ion energies are optimized when the foil thickness is according to [120]

$$L \approx \frac{a_0 n_{crit}}{\pi n_0} \lambda. \quad (5.1)$$

To determine this optimal thickness for the JETi200 laser system, we conducted ex-

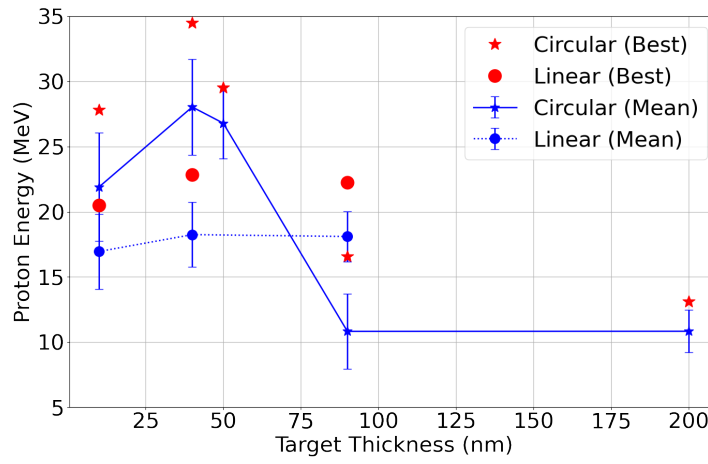


Fig. 5.2: The target thickness scan with circular and linear polarization laser. The mean value and the best data are shown for each thickness.

periments using various formvar targets at a laser intensity of around $2 \times 10^{21} \text{ W/cm}^2$. Results demonstrate a strong dependence of the proton beam's cut-off energy on the target thickness, as shown in Fig. 5.2. In the circular polarization case, the optimal thickness of 40 nm produces a mean cut-off energy of over 25 MeV, with the best case achieving 34 MeV. The mean and optimal energies are significantly reduced for thinner or thicker targets. In the linear polarization laser, the energy of the proton beams exhibits a weak dependence on thickness. The mean energy of the proton beams generated from various thicknesses is around 18 MeV. Notably, the proton beam energy produced from the 90 nm target is significantly higher than that achieved under circular polarization beams. For the transmission light, as shown in Fig.5.3, the 10 nm target exhibits almost doubles the transmission light of the 40 nm target, indicating that it is too thin to remain opaque to the driving laser. This results in premature dissociation of the target, with part of the driven light

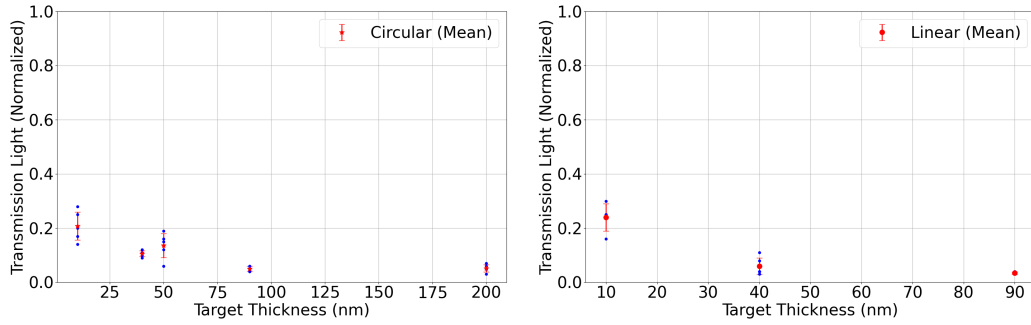


Fig. 5.3: The transmission light was measured for the circular and linear polarization light. The mean value and some data points are shown.

leaking through the target and failing to effectively accelerate the protons in the plasma. In contrast, targets of 90 nm and 200 nm thickness are too thick, with the electrostatic force from charge separation becoming dominant over light pressure, causing more driving light to reflect. While thicker targets can accelerate more ions, the ion energies achieved are relatively low.

Experimental result suggests that an optimal target thickness exists for circularly polarized driving light, which can enhance the conversion efficiency of laser light and boost the energy of protons. However, there is no noticeable distinction in the range of 10 nm - 100 nm for lasers driven by linearly polarized light. For linearly polarized light, the laser initially converts the energy into electrons. Subsequently, hot electrons generate a sheath field on the rear side. If the target thickness, denoted as L , and the laser pulse duration, denoted as t_p , satisfy the relation $2L < ct_p$, relativistic electrons number accumulate through recirculation between the front and rear surfaces of the target[121]. Stochastic heating causes an increase in electron temperature beyond the ponderomotive scaling in the multi-ps time scale[122]. These recirculated electrons transfer their energy to the ions, and the electron temperature is closely related to the energy of the ions. Experimental finding demonstrates that when a linearly polarized laser irradiates thin targets below 100 nm, there is no significant difference in electron temperature[123]. Hence, in thin target experiments with target thickness ranging from 10 nm to 90 nm, no apparent thickness dependence was observed.

5.2.2 Proton Energy Spectrum

In the previous section, the target thickness effect has been investigated. Next, the proton spectrum of the various thickness targets is shown in Fig.5.4. Fig.5.4 is typical proton spectra produced in experiments with circularly polarized lasers. In most cases, targets smaller than 90 nm can produce monoenergetic proton beams.

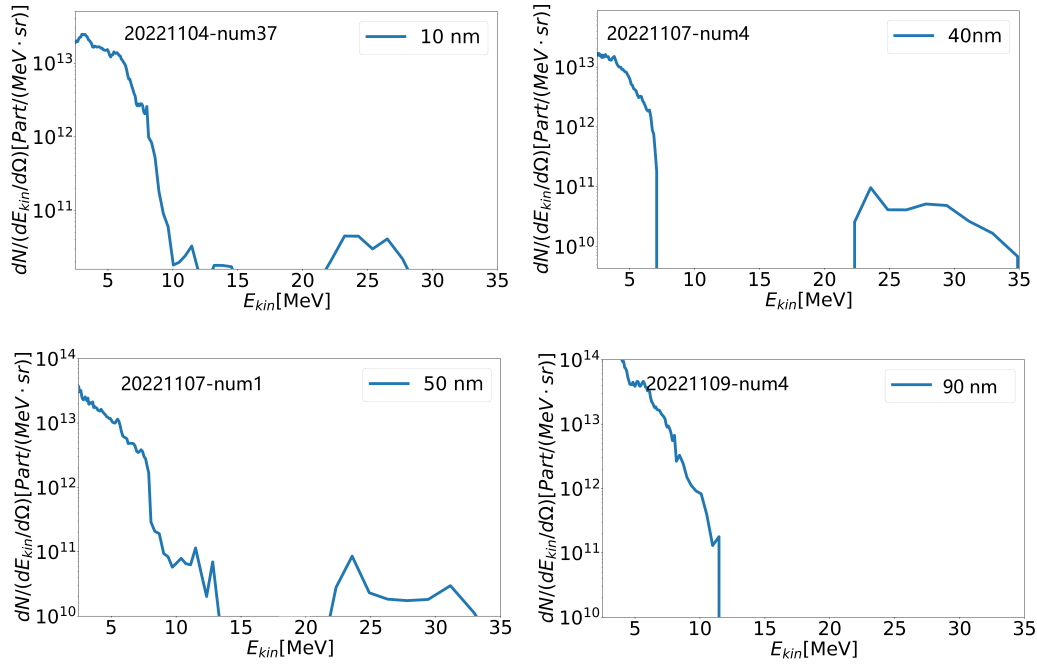


Fig. 5.4: When the circular polarization shoots the various thickness targets, distinct energy spectral distributions are observed. 10 nm - 50 nm targets display a monoenergetic proton peak in their spectrum. The raw energy spectrum can be seen in Appendix: Raw Proton Spectrum.

In the case of thin targets, e.g., the thickness is thinner than 90 nm, the energy spectrum comprises of two parts - a linear decay of low-energy protons and a monoenergetic proton spectra of high-energy protons, indicating a mixture of different acceleration mechanisms. Low-energy protons can be eliminated using mass-limited targets as shown in previous experiments[37, 86], as they are mainly produced outside the $1/e^2$ diameter of the focal spot. The monoenergetic peak is believed to be the result of the RPA mechanism. In the RAP mechanism, the ponderomotive force of the laser pushes the electrons forward, but the ions leave behind due to heavy mass. When the space-charge electric field between the electrons layer and

ions can balance the ponderomotive force. These ions are trapped and move together with the electron layer. The laser ponderomotive force longitudinally accelerated the electron layer and the ion layer at the same time, which resulted in monoenergetic ion production[124]. However, for the 90 nm thick target, the spectrum exhibits a relatively low cut-off energy with a linear shape. Despite having the same parameters as other experiments[123], both the cut-off energy and energy spectrum have significantly improved, resulting in the doubling of cut-off energy and formation of a monoenergetic peak. These are mainly due to the enhancement of coherent laser contrast, which significantly suppresses thin target expansion and deformation within hundreds of femtoseconds. In contrast, the proton spectrum driven by linearly

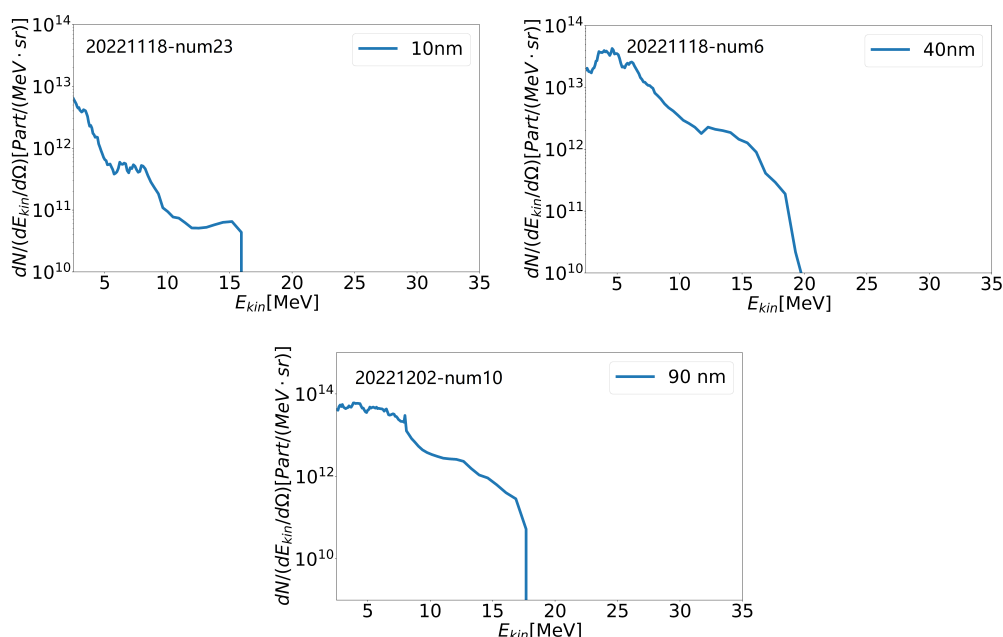


Fig. 5.5: Linear polarization laser shoots the different thickness targets. The energy spectrum presents a complete absence of the monoenergetic peak compared to circularly polarized lasers, with an linear decay emerging as the dominant feature. The raw energy spectrum can be seen in Appendix: Raw Proton Spectrum.

polarized light is relatively mediocre, as shown in Fig.5.5. The energy spectrum of the proton beam for different targets exhibits consistent linear tendencies, and no monoenergetic peak appears. It is worth noting that the number of protons varies with the target thickness. For thin targets below 100 nm, the energy of electrons under linearly polarized laser irradiation is similar[123], and hot electrons transfer energy to ions, but thick targets have more ions, resulting in a high number of low-energy ions.

5.2.3 Proton Energy Scaling

Energy scaling study is a meaningful step to evaluate the laser parameters needed to produce high-quality, high-energy proton beams. Numerous scaling studies have already been conducted across various facilities, ranging from table-top lasers to large-scale single-pulse laser facilities[125, 126, 127, 34]. In the experiment the scaling of the maximum proton energy with laser intensity was measured, as shown in Fig.5.6. Here, 40 nm and 90 nm targets were irradiated by the circularly and linearly polarized laser beams, respectively. For the circularly polarized laser beam, the 40 nm shows a faster linear scaling with laser intensity, $E \propto I$. It is faster than the other similar experiment $E \propto I^{0.6}$ [128, 129]. However, the 90 nm has slow scaling, $E \propto I^{0.5}$ in the experiment. 40nm and 90nm have similar scaling under linearly polarized laser irradiation. It is worth note when the laser intensity is greater than 10^{21}W/cm^2 , monoenergetic protons can be produced in a 40 nm target with circular polarization irradiation.

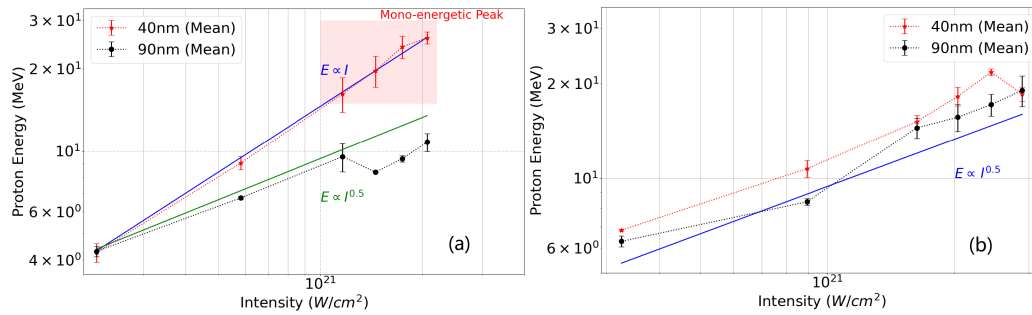


Fig. 5.6: The scaling of maximum proton energy is presented with respect to laser intensity. (a) is the results of circularly polarized laser and (b) is the results of linearly polarized laser. The 40 nm and 90 nm targets are illuminated by each driving light, respectively. The typical raw energy spectrum can be seen in Appendix: Raw Proton Spectrum.

5.3 EPOCH 2D Simulation

EPOCH is a widely used plasma physics simulation code that employs the Particle-in-Cell (PIC) method[130]. In this method, a small number of pseudoparticles are used

to represent the physical particles in the plasma, which are then separated into small grids in space. The electric and magnetic fields that drive these pseudoparticles are calculated within each grid, and the resulting forces on the pseudoparticles are utilized to update their positions and velocities. A finite difference time domain technique is used to compute the motion of these pseudoparticles, with a fixed spatial resolution. EPOCH is a mature program that describes the physical interaction process between ultrashort pulses and plasmas within hundreds of femtoseconds. In this section, EPOCH 2D was performed to explain the acceleration process of ions under ultra-intense laser fields.

5.3.1 Multi-species Target Parameters

In order to explore the physical process of the laser-plasma interaction, 40 nm and 90 nm are examined by the EPOCH 2D. The formvar molecular structure is $[C_3H_6O_2]_n$, and the density is 1.23g/ml. In the simulation, the Formvar target is composed of carbon, hydrogen and oxygen atoms according to its composition, as summarized in Table 5.1.

Nuclides	Mass number	Number of molecular	Molecular weight
H	1	6	6
C	12	3	36
O	16	2	32
Total Weight (A)	74.08		

Tab. 5.1: Target composition calculation for the Formvar $[C_3H_6O_2]_n$

$$N_{[C_3H_6O_2]} = \frac{\rho}{A \times 1.66 \times 10^{-27}} = 1.00 \times 10^{28} m^{-3} \quad (5.2)$$

According to the equation 5.2, the density of the formvar molecular $[\text{C}_3\text{H}_6\text{O}_2]_n$ is around $1.00 \times 10^{28} \text{m}^{-3}$. The corresponding density of each atom is

$$n_H = 6.00 \times 10^{28} \text{m}^{-3}, \quad (5.3)$$

$$n_C = 3.00 \times 10^{28} \text{m}^{-3}, \quad (5.4)$$

$$n_O = 2.00 \times 10^{28} \text{m}^{-3}, \quad (5.5)$$

and

$$\begin{aligned} n_{electron} &= 4.00 \times 10^{29} \text{m}^{-3} \\ &= 230 \times n_{c800nm}. \end{aligned} \quad (5.6)$$

Here, n_{c800nm} is the plasma critical density of the 800 nm wavelength.

5.3.2 Accelerating Electric Field and Ion Spatial Distribution

EPOCH performed simulations. The grid with a resolution of $\Delta x = 2 \text{nm}$ and $\Delta y = 10 \text{nm}$, using an idealized 30 fs, 800 nm driving laser to irradiate flat foils of 40 nm and 90 nm thickness at normal incidence. The x range is from $-20 \mu\text{m}$ to $50 \mu\text{m}$ and the y range is from $-10 \mu\text{m}$ to $10 \mu\text{m}$. The target is initially located at $x = 0 \mu\text{m}$, and the width of the target is $20 \mu\text{m}$. The laser intensity is $a_0 = 25$ for the circular polarization laser beams. The resulting changes in the accelerating electric field and spatial distribution of ions over time were displayed in Fig. 5.7 to Fig. 5.9. The left y-axes show the average ion density for H^+ , C^{6+} , O^{8+} , and electrons, respectively, averaged within the FWHM of the focus. The right y-axes depict the cycle-averaged longitudinal electric field E_x . $T = 0 \text{fs}$ corresponds to the time that the peak of the pulse arrives at the target.

1. Leading edge of the main pulse arrives the target ($T = -20 \text{fs}$):

Fig.5.7 shows the charged particles and the acceleration field distribution in space. a) and b) is the results of 40 nm and 90 nm target, respectively. When the leading edge of the main pulse arrives, it overcomes the thermal pressure from the hot plasma and exerts radiation pressure. The leading edge of the main pulse compresses the plasma front surface. At the same time, the laser reflects from the overdense plasma, creating a standing wave that enhances the local electric field and steepens the

plasma front. Although all particles are pushed forward, the laser cannot penetrate the overdense plasma, accelerating ions through the Hole-Boring RPA (HB-RPA) mechanism at the interaction surface and TNSA at the rear side of the target. The electrostatic field efficiently accelerates protons to a significant speed, whereas heavy ions experience minimal acceleration. The protons quickly separate from the heavy ions in the 40 nm target and modulate the accelerating electric field, as shown in Fig. 5.7 a). By contrast, the acceleration process in the 90 nm target cannot separate the protons from the heavy ions due to more ions. The accelerating electric field is related to the acceleration process of ions. In the 40 nm target, the ponderomotive force of the laser combined with the space charge electric field form a bunching field at the foil front surface and attenuation towards the rear side of the target. For the 90 nm target, the massive ions shield the bunching field at the foil front surface, and there is an electrostatic field at the rear side of the target formed by the hot electrons.

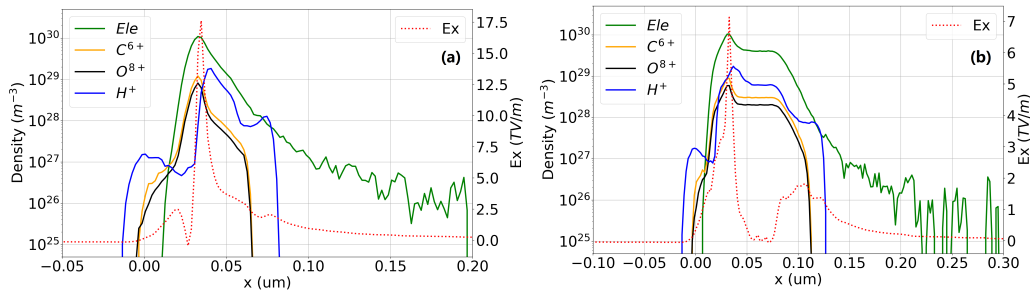


Fig. 5.7: When $T = -20$ fs, the leading edge of the main pulse reaches the target. When the laser drives the plasma, it compresses and accelerates all ions. For the 40 nm target (a), the proton beam is separated from the heavy ions during acceleration and modulates the accelerating electric field. However, for the 90 nm target (b), the protons and heavy ions mix together during acceleration.

2. Main pulse peak arrives the target ($T = 0.0$ fs):

Then the main pulse peak directly interacts with the compressed plasma. For the 40 nm target, the inner protons pile up and are further accelerated and separated from the heavy ions (The gap is between 0.1 μm and 0.2 μm in Fig. 5.8 b). Since the proton beam velocity is faster than the heavy ion beams (C^{6+} and O^{8+}). These heavy ions fill the gap, forming a buffer to protect the proton bunch from the Rayleigh-Taylor-like (RT) instability that could degrade the proton beam acceleration[131]. And the multispecies target helps to stabilize RPA of the protons so that a more pronounced spectral peak can be achieved[132]. The bunching field peak is near

the front edge of the proton bunch, and the bunching field decays along the laser propagation direction, the relatively low-energy protons feel a stronger accelerating electric field. The acceleration mechanism at this stage is mainly attributed to the Light-Sail RPA (LS-RPA). But for the 90 nm target, protons still cannot be entirely separated from heavy ions, and the debunching field rides on the proton beam. The violent fluctuation of the acceleration gradient in space will cause the disorder of the proton bunch and the broadening of the proton energy spectrum.

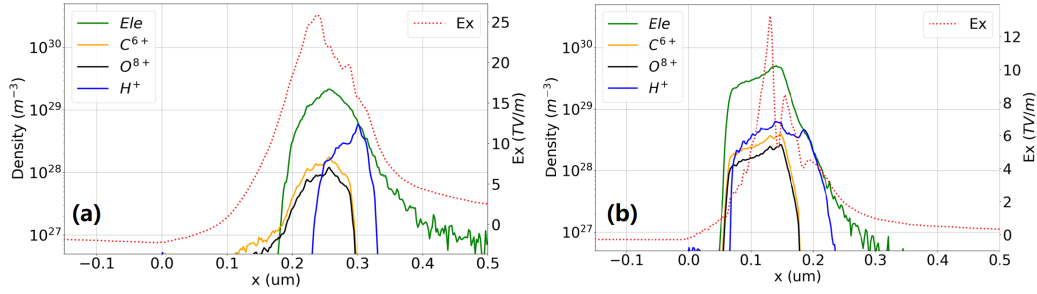


Fig. 5.8: The main pulse peak arrives at the target ($T = 0.0$ fs) and interacts directly with the compressed plasma. In the case of the 40 nm target (a), the protons are separated further from the heavy ions. However, in the 90 nm target (b), the protons mix with the heavy ions. The accelerating electric field exhibits significant fluctuations that lead to broadening of the proton beam.

3. Driving laser light away from the interaction region ($T = 40.0$ fs):

When the driving laser is completely reflected and no longer directly accelerates the ions at $T = 40.0$ fs, as shown in Fig.5.9, the local electrons and ions dominate the E_x -field peak. For the 40 nm target, heavy ions located behind the protons provide Coulomb repulsion, which stabilizes proton acceleration. The polarity reversal location occurs at the proton beam's front edge ($x = 1.7 \mu\text{m}$) and out of the proton bunch. However, for a 90 nm target, this polarity reversal point is inside the proton bunch, causing positive and negative particles to oscillate around the polarity reversal point. Low and medium energy protons cannot form stable acceleration due to spatially disordered accelerating electric field. But for protons near the cutoff energy, the heavy ions sit behind them. The Coulomb repulsion provides further acceleration, similar to the protons in the 40 nm target case.

In summary, through the study of the spatial distribution of the component ions and the accelerating electric field during the acceleration process, the protons can be quickly separated from the heavy ions when the target thickness is optimal. Heavy

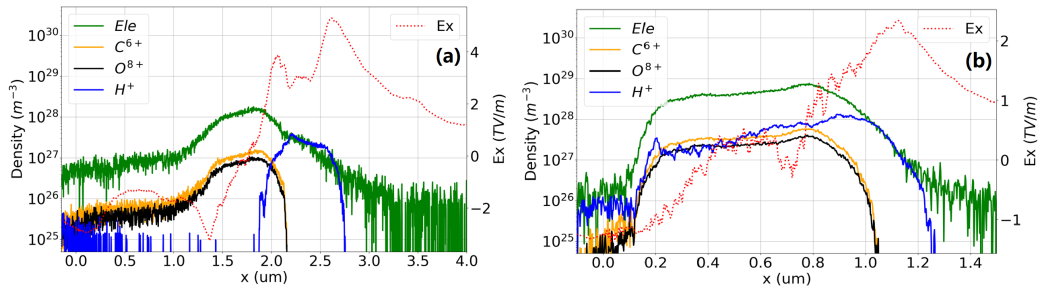


Fig. 5.9: Driving the laser light away from the interaction region ($T = 40.0$ fs). (a) is the 40 nm target, and (b) is the 90 nm target. The Ex-field peak is dominated by the local electrons and ions.

ions act as a buffer between the accelerating electric field and the proton beam. The formation of the bunching field ensures stable acceleration of the monoenergetic proton beam. The simulation results show that it is very important whether protons can be separated from heavy ions in the early stage of acceleration. Because the bunched proton beam is not affected by RT due to the buffering effect of heavy ions, and can be stably accelerated and form a monoenergetic proton beam finally. This conclusion is consistent with related simulation studies[131, 133, 134, 135]. However, in the case of a thick target, protons and heavy ions are mixed in space, and the debunching field will seriously disturb the proton beam, resulting in the inability to form a stable proton beam. In the later stage of proton acceleration, the heavy ions are behind the high-energy protons, and due to the Coulomb repulsion, the high-energy protons can be further accelerated.

5.3.3 Divergence of Protons

The divergence angle of outgoing protons is a crucial parameter, as shown in Fig.5.10. Specifically, (a), (b), and (c) demonstrate the proton divergence of the 40 nm target at different moments, while (d), (e), and (f) describe the same for the 90 nm target. When the laser's leading edge interacts with the targets at $T = -20$ fs, as shown in (a) and (d) for the 40 nm and 90 nm targets, respectively, the proton beams have better collimation along the laser propagation direction, with a FWHM of around 2.5° and 5° for the 40 nm and 90 nm targets, respectively. The above acceleration mechanism is mainly dominated by HB-RPA. At $T = 0$ fs, the main peak directly accelerates the proton. In the case of the 40 nm target, nearly all protons in the focal

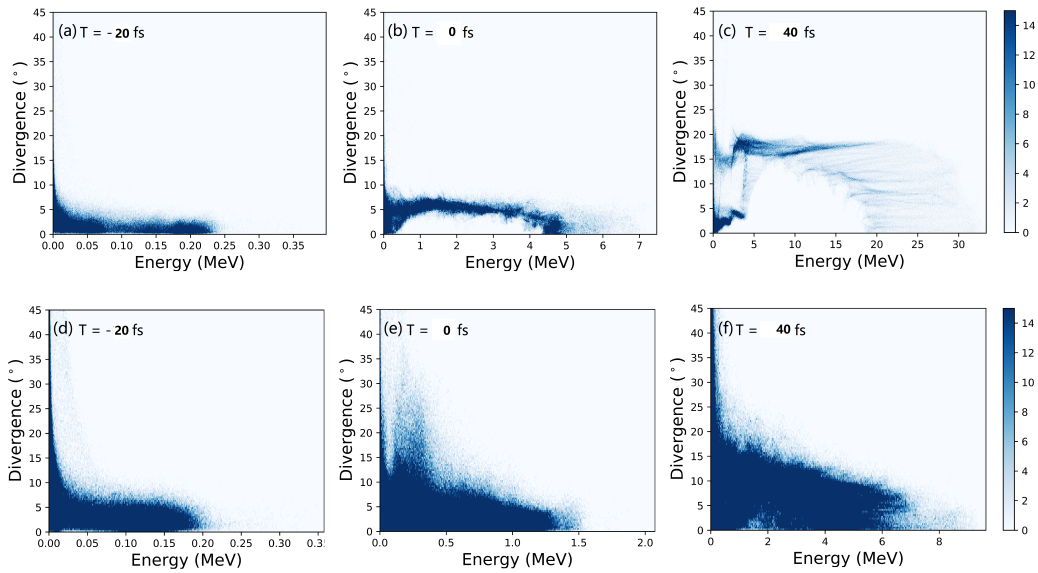


Fig. 5.10: The divergence angle distributions of the 40 nm and 90 nm target proton beams at different times are shown respectively. (a) - (c) and (d) - (f) correspond to the results for 40 nm and 90 nm targets, respectively.

spot are rapidly accelerated to 4.5 MeV. Low-energy protons are produced around the focus, and almost all protons are pushed aside due to the geometry of the focal point, with the larger divergence angle. Conversely, for the 90 nm target, the proton beam cannot be effectively separated from the background heavy ions, unable to form a monoenergetic proton beam along the direction of laser propagation. When the driving laser is away from the interaction region, $T = 40$ fs, the divergence angle of the middle and low energy protons is further increased due to the repulsion force between protons and background heavy ions, but the high energy protons maintain good collimation.

5.3.4 Phase Space Distribution of Protons

Fig. 5.11 illustrates the phase space evolution of the protons. Here, the collection angle of the protons is limited to 5° to study the acceleration behavior near the paraxial. Fig. (a) to (c) show the proton phase space distribution in the 40 nm target. When the time is -20 fs, the protons on the target front surface feel the HB-RPA, and the rear side protons feel TNSA. The front side high momentum protons pass through the plasma and overlap with the rear side low momentum protons in space.

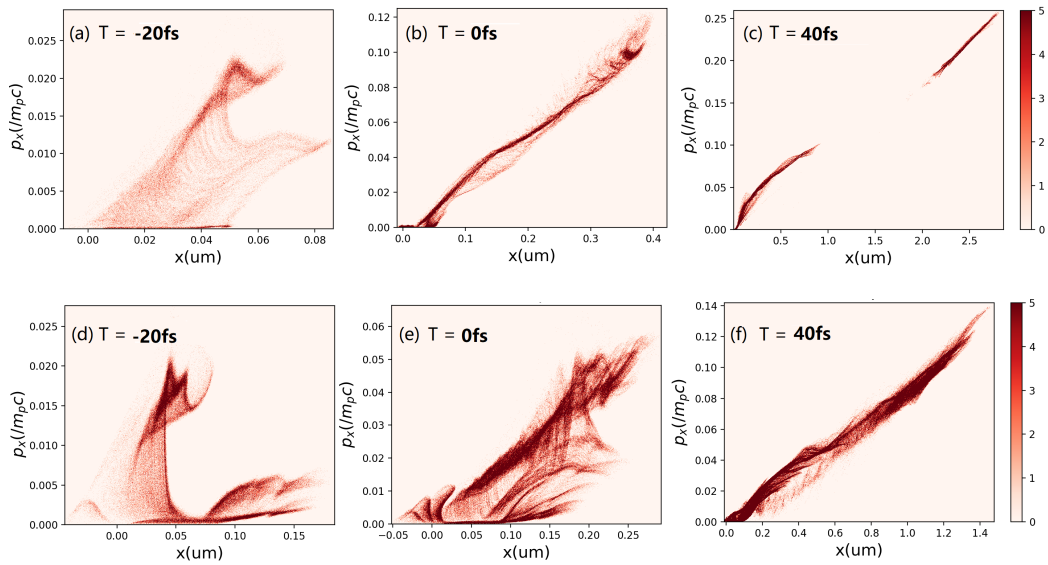


Fig. 5.11: The proton phase space density distribution at different times. Specifically, (a)-(c) represent the results for the 40 nm target, while (d)-(f) depict those for the 90 nm target.

Then, $T = 0$ fs, all protons are accelerated by LS-RPA and the high-energy protons form a bunch. Finally, middle-energy protons cannot be detected due to their large divergence angles. High-energy protons form monoenergetic proton beam. The results of the 90 nm target, (d) - (f), show a similar process, but when the main pulse arrives at the target, $T = 0$ fs, exhibits a highly chaotic phase space distribution between $0.1 \mu\text{m}$ and $0.22 \mu\text{m}$, due to the sharp variation in the accelerating electric field as shown in Fig.5.8 (b). Finally, no isolated proton beams are formed.

5.3.5 Proton Energy over Time

Fig. 5.12 shows the proton energy over time. The simulation results are presented for 40 nm and 90 nm targets, denoted by (a) and (b) respectively. Considering the practical conditions of the experiment, protons with a collection angle of 5° and located near the focal point are shown. Time $T = 0$ fs represents the moment when the main pulse peak reaches the target position at $x = 0 \mu\text{m}$.

For $T < -8$ fs, the energy increase of protons is low, indicated by a low slope. The dominant acceleration mechanisms during this phase are attributed to TNSA and

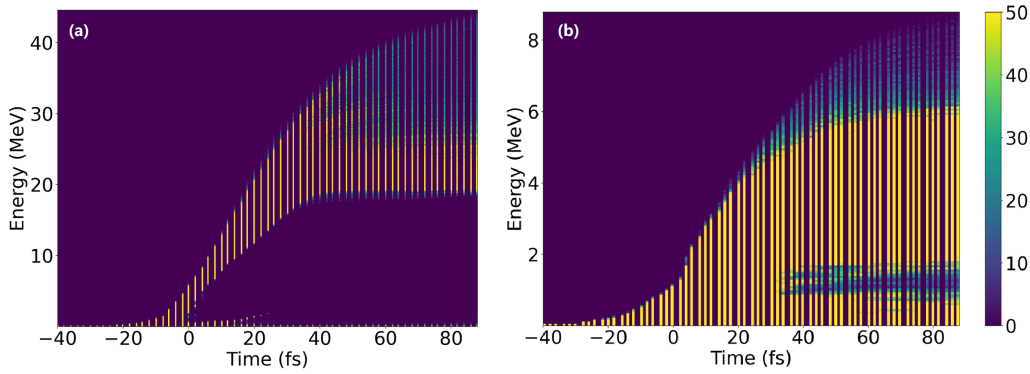


Fig. 5.12: Proton energy against time. (a) and (b) are 40 nm and 90 nm targets, respectively. Only the protons with a collection angle of 5° and located near the focal point are shown.

HB-RPA. When $-8 \text{ fs} < T < 30 \text{ fs}$, the proton energy increases rapidly, with the energy increase rate being approximately 0.52 MeV/fs for the 40 nm target and 0.11 MeV/fs for the 90 nm target. In the case of the 40 nm target, all protons in the focal spot are rapidly accelerated and separated from the heavy ions, forming a bunched beam. But the proton energy spread gradually increases over time. Due to the energy increase slope of high-energy protons is higher than that of low-energy protons. This phenomenon is attributed to the mixture of low-energy protons and heavy ions in space, where the driving force is primarily laser pressure. As the laser pressure gradually decreases, the low-energy protons' acceleration rate also decreases. High-energy protons, experience both laser pressure acceleration and Coulomb repulsion from the heavy ions behind them, resulting in stable and long-term acceleration. The acceleration mechanisms involved are Light-Sail RPA and Coulomb repulsion.

Notably, when $T > 30 \text{ fs}$, the driving laser is completely reflected and ceases to interact with the plasma. Consequently, the energy of low-energy protons ($\sim 20 \text{ MeV}$) does not increase further, while the acceleration time of high-energy protons exceeds 70 fs, reaching an energy of 40 MeV. During this period, the acceleration of high-energy protons is mainly attributed to Coulomb repulsion provided by the heavy ions behind them. The high-energy protons of the 90nm target have a similar acceleration process. However, due to the protons not being separated from the heavy ions during the initial acceleration stage, a proton bunch is not formed, resulting in the absence of a distinct monoenergetic proton beam.

5.4 Summary

In this chapter, the laser proton acceleration based on multi-species targets is systematically studied through experiment and simulation. The energy and spectral distribution of the protons were measured by varying the laser polarization and the target thickness. Experiments have demonstrated that when circularly polarized light illuminates a thin target with a thickness below 90 nm, monoenergetic proton beams can be generated. In the case of linearly polarized light, no monoenergetic proton beams were observed. The monoenergetic proton feature can be mainly attributed to the Hole-Boring RPA and Light-Sail RPA acceleration mechanisms. PIC simulation indicates that the protons pile up and separate from the background heavy ions during the early stage of the laser pulse and plasma interaction. Then, when the main laser peak reaches the target, the Light-Sail RPA acts as the dominant acceleration mechanism, forming a bunch acceleration field with background ions and electrons. The accelerating electric field is located behind the proton bunch, and the heavy ions are situated between the accelerating electric field and the proton bunch as a buffer, both providing a stable accelerating condition for the proton bunch. When the driving laser is completely reflected and ceases to interact with the plasma, Coulomb repulsion between the heavy ions and the high-energy protons provides an additional acceleration force to enhance the energy. The experiments successfully demonstrated many of the simulation-predicted results of high-contrast circularly polarized laser pulses that drive multi-species targets and efficiently generate monoenergetic ions. In the experiment, the energy conversion can reach $\sim 20\text{MeV/J}$ for the proton bunch.

Near-Critical Density Plasma Diagnosis

” *Imagination is more important than knowledge.*

— **Albert Einstein**

The evolution of pre-plasma induced by the pre-pulse has garnered significant attention due to its strong influence on the state of the plasma, subsequently impacting the interaction of the main pulse with the plasma. For example, the ion wave breaking acceleration (IWBA)[136, 137] needs the low-density plasma to trap and accelerate ions. The effects of pre-plasma on various experiments have been extensively reported. In this chapter, dense plasma is irradiated with multicolor probe light, and the transmittance of the probe light is measured. The Helmholtz equations for an electromagnetic wave are then induced to calculate the absorption coefficient and correct the transmission of the probe beam. The maximum plasma density evolution over time is qualitatively measured. Finally, the experimental results are compared with existing prediction models to validate their accuracy in predicting the plasma's evolution process.

6.1 Numerical Calculation of Probe Light Transmittance

6.1.1 Theory

In the past few decades, significant strides have been made in comprehending and modeling the absorption mechanisms of nanosecond laser pulses, which operate at intensities ranging from $10^{12}\text{W}/\text{cm}^2$ to $10^{16}\text{W}/\text{cm}^2$, both theoretically and experi-

mentally. The primary absorption mechanisms identified for these pulses are classical resonance absorption and collisional absorption (inverse bremsstrahlung), which mainly depend on the plasma density, plasma scale-length and laser intensity[138]. A crucial issue is that when ns-scale probe beams pass through near-critical density, inhomogeneous plasma, the plasma absorbs a fraction of the probe beam. To tackle this issue, Helmholtz equations for an electromagnetic wave are used to compute the absorption coefficient and correct the probe beam's transmission in the following section. The experiment employs probe beams of three different colors, with a total energy low enough ($< 10^{12}\text{W}/\text{cm}^2$) that they cannot ionize solid targets. The ultra-thin targets remain transparent to the probe laser before pre-pulse ionization. Once the pre-pulse ionizes the target, the thin target transforms rapidly into an overdense pre-plasma with low temperature. For the probe pulse, the dominant absorption mechanism is collisional absorption (inverse bremsstrahlung) due to the electron-ion collisions, whereas Landau damping of resonantly excited plasma waves can be ignored since the electron mean free path is much less than the density scale length[139]. This analysis focuses only on small field amplitudes and the non-relativistic fluid response of the pre-plasma. The electron motion equation in a non-relativistic electromagnetic field is given by the Lorentz equation, including collisional damping,

$$m_e \frac{d\mathbf{v}}{dt} = -e[\mathbf{E}(\mathbf{r}, t) + \frac{\mathbf{v}}{c} \times \mathbf{B}(\mathbf{r}, t)] - m\nu_{ei}\mathbf{v}, \quad (6.1)$$

where \mathbf{E} and \mathbf{B} are the electric and magnetic field intensities, respectively. ν_{ei} is the electron-ion collision frequency[138]. \mathbf{v} represents the velocity of the electron fluid. Electrons, being the lightest stable subatomic particles, are highly sensitive to laser fields, making them the primary medium for energy transfer between laser and matter. Initially, energy is coupled to electrons by the laser, which then transfers it to heavy ions through electron-ion collision processes. The electron-ion collision frequency, a key factor in this process, is given by [138]

$$\nu_{ei} = \frac{(32\pi)^{0.5}}{3} \frac{n_e Z e^4}{m^2 \nu_{te}^3} \ln \Lambda \simeq 2.91 \times 10^{-6} Z n_e T_e^{-3/2} \ln \Lambda \text{ s}^{-1}. \quad (6.2)$$

Here Z is the number of free electrons per atom, n_e is the electron density in cm^{-3} , T_e is the temperature in eV. $\ln\Lambda$ represents the Coulomb logarithm, defined as

$$\Lambda = \frac{b_{max}}{b_{min}} = \lambda_D \frac{k_B T_e}{Z e^2} = \frac{9 N_D}{Z}, \quad (6.3)$$

$$\lambda_D = \left(\frac{k_B T_e}{4\pi n_e e^2} \right)^{1/2} = \frac{\nu_{te}}{\omega_p}, \quad (6.4)$$

$$N_D = \frac{4\pi}{3} \lambda_D^3 n_e. \quad (6.5)$$

Here, they are determined by the classical distance of the closest approach and the integration over the whole range of scattering angles[138]. However, at high temperatures, quantum-mechanical corrections need to be considered. The impact parameter b is defined using characteristic lengths in the plasma, such as $b_{max} = \lambda_D$ and $b_{min} = l_a$ (the interatomic distance). N_D is the number of electrons in a Debye sphere.

The EM waves in the plasma can be obtained by combining the Ampère's circuital law and Maxwell – Faraday equation, Eqs.2.6 and 2.5 with the source terms of the EM waves on the right-hand sides as follows:

$$\begin{aligned} \nabla^2 \mathbf{B} - \frac{1}{c^2} \cdot \frac{\partial^2 \mathbf{B}}{\partial t^2} &= \mu_0 \cdot \nabla \times \mathbf{J}, \\ \nabla^2 \mathbf{E} - \frac{1}{c^2} \cdot \frac{\partial^2 \mathbf{E}}{\partial t^2} &= \mu_0 \cdot \frac{\partial \mathbf{J}}{\partial t} + \nabla(\nabla \cdot \mathbf{E}). \end{aligned} \quad (6.6)$$

Assuming that all field and fluid quantities have harmonic variation and making the following simplifications[19], to simplify these equations:

$$\mathbf{E} + \nu \times \mathbf{B} \rightarrow \mathbf{E}, \quad (6.7)$$

$$\frac{\partial}{\partial t} \rightarrow -i\omega, \quad (6.8)$$

$$n_e \rightarrow n_0 + n_1, \quad (6.9)$$

$$\mathbf{J} \rightarrow -en_0 \mathbf{v}. \quad (6.10)$$

Here, the plasma current density \mathbf{J} , can write as

$$\mathbf{J} = -en_0 \mathbf{v} = \sigma \cdot \mathbf{E}, \quad (6.11)$$

$$\sigma = i\varepsilon_0 \frac{\omega_p^2}{\omega_l + i\nu_{ei}}. \quad (6.12)$$

Where ω_p and ω_l are the plasma frequency and the laser frequency, respectively. Accounting for Ohm's law, the plasma complex conductivity is given by σ .

By assuming a planar laser electromagnetic field propagating through a uniform plasma and solving the Helmholtz wave equations as mentioned above. One can obtain the linear dispersion relation with collisions, given by

$$k^2 - \frac{\omega^2}{c^2} \left[1 - \frac{w_p^2}{w_l^2 (1 + i\nu_{ei}^*)} \right] = 0, \quad (6.13)$$

where the electron-ion collision frequency is normalized by the laser frequency, $\nu_{ei}^* = \nu_{ei}/w_l$, for convenience. Meanwhile, the complex refractive index of the plasma is given by

$$n^2 \equiv \epsilon \equiv \frac{k^2 c^2}{w_l^2} = 1 - \frac{w_p^2}{w_l^2 (1 + i\nu_{ei}^*)}. \quad (6.14)$$

In principle, for a non-uniform plasma, the collision frequency replaces by a local complex reflective index :

$$n^2(x) \equiv \epsilon(x) = 1 - \frac{n_0(x)/n_c}{1 + i\nu_{ei}^*(x)}, \quad (6.15)$$

where $n(x)$ is the local refractive index of plasma, n_0 is the equilibrium electron density and n_c is the plasma critical density of the EM wave.

To estimate the absorption fraction of the probe pulses in the plasma, one can solve the Helmholtz equations (6.6) numerically, accounting for a non-uniform plasma profile[19]. For a p-polarized wave with an incident angle of θ , the electric and magnetic field components are $\mathbf{E} = (E_x, E_y, 0)$ and $\mathbf{B} = (0, 0, B_z)e^{iky, \sin\theta}$, respectively. The wave equation is treated as[19]

$$\frac{\partial^2 B_z}{\partial x^2} - \frac{1}{\epsilon} \frac{\partial \epsilon}{\partial x} \frac{\partial B_z}{\partial x} + k^2 (\epsilon - \sin^2 \theta) B_z = 0, \quad (6.16)$$

and in s-polarized wave with the same incident geometry where the components of electric is $\mathbf{E} = (0, 0, E_z)e^{iky \sin\theta}$, the wave equation reduces to[19]

$$\frac{\partial^2 E_z}{\partial x^2} + k^2 (\epsilon - \sin^2 \theta) E_z = 0. \quad (6.17)$$

In the Helmholtz solver, the geometry of the laser incident on a non-uniform plasma density profile as shown in Fig.6.1. For the expanding plasma with nanometer thickness (<100 nm), the plasma is almost symmetrically distributed. The laser is incident on the plasma at a certain angle θ , and the plasma density along the path changes from low density to high density. When reaching the boundary, the laser light reflects and leaves the plasma, and the plasma density changes from high density to low density along the path. This simulates the movement path of the laser in the expanding plasma. When the plasma scale length is extremely short, the results of the Helmholtz equations should be close to that of the Fresnel equations. From this perspective, the accuracy of the Helmholtz solver can also be verified, a comparison can see Appendix: Helmholtz and Fresnel equations.

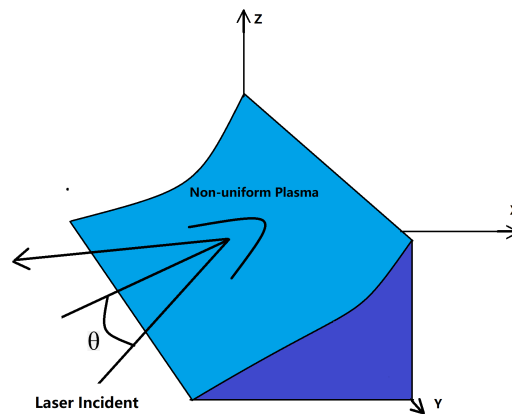


Fig. 6.1: Geometry of the laser incident on a non-uniform plasma at a certain angle θ .

6.1.2 Non-uniform Plasma Density Profile

Previously, it was noted that the primary factors impacting collision absorption are the plasma density scale length and density. In the Helmholtz solver, we assume an exponential density profile consistent with a one-dimensional model for isothermal plasma expansion and a density-dependent collision frequency. As an estimate, the scale length is determined by multifs[140] for different wavelength probe beams. Fig.6.2 and Fig.6.3 show the spatial distribution of plasmas with different maximum densities for the initial 30 nm and 90 nm targets, respectively. The pre-pulse intensity

is $5 \times 10^{13} \text{W/cm}^2$. (a) and (b) respectively correspond to the situations of 355 nm and 532 nm probe light in each figure.

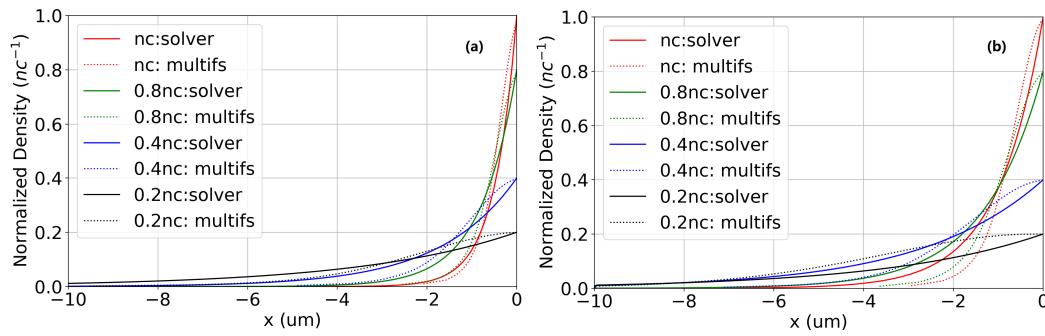


Fig. 6.2: Spatial distribution of plasmas with different maximum densities. Initial thickness is 30 nm, and the pre-pulse intensity is $5 \times 10^{13} \text{W/cm}^2$. (a) and (b) correspond to 355 nm and 532 nm probe light, and plasma densities are normalized by $n_{c355\text{nm}}$ and $n_{c532\text{nm}}$, respectively. “multifs” means the multifs outputs the plasma density profile and “solver” means the plasma density profile used in the solver.

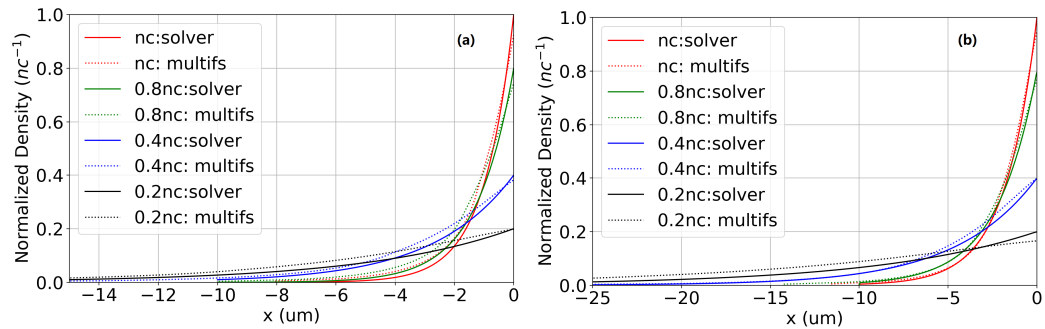


Fig. 6.3: Spatial distribution of plasmas with different maximum densities. Initial thickness is 90 nm, and the pre-pulse intensity is $5 \times 10^{13} \text{W/cm}^2$. (a) and (b) correspond to 355 nm and 532 nm probe light, and plasma densities are normalized by $n_{c355\text{nm}}$ and $n_{c532\text{nm}}$, respectively. “multifs” means the multifs outputs the plasma density profile and “solver” means the plasma density profile used in the solver.

6.1.3 Probing Light Transmission in Near Critical Density Plasmas

When a low-intensity laser light is incident on over-dense plasma, it will be reflected. Conversely, if the plasma density is low enough, the laser beam will almost completely

penetrate the plasma. However, if the probe beam hits a near-critical density plasma, absorption becomes more complex. Depending on the probe laser intensity and plasma conditions, absorption can be categorized into collisional or collisionless. In our experiment, the low-intensity laser light ($< 10^{12} \text{W/cm}^2$) is incident on a non-relativistic, strong collision plasma (plasma density $< n_c$), making reflection negligible. Because the probe light absorption mechanism is the collision absorption and the light has multiple reflection events within the near-critical density plasma due to the plasma density gradient, the light transfers its energy to electrons, leading to a strong absorption of the light. Finally, the escaping reflected light from the plasma could be ignored [141], namely

$$I_{total} \approx T + A. \quad (6.18)$$

Here, I_{total} represents the incident beam, T represents the transmitted beam (or detected beam), and A represents the beam absorbed by the near-critical density plasma. Strong absorption requires the calculation of absorption rate, which helps in inferring the plasma density from the transmitted light. The plasma density n and laser frequency ω_{laser} can be defined as:

$$n = \frac{\varepsilon_0 m_e}{e^2} \omega_{pe}^2, \quad (6.19)$$

$$\text{and} \quad (6.20)$$

$$\omega_{laser} = 2\pi \frac{c}{\lambda}. \quad (6.21)$$

When the plasma angular frequency is lower than the laser angular frequency, the plasma is transparent to the laser. On the contrary, the laser reflects from the over-dense plasma when the plasma angular frequency is higher than the laser angular frequency. Combining the above two formulas, one can get

$$nc = 4\pi^2 \frac{\varepsilon_0 m_e c^2}{e^2} \frac{1}{\lambda^2}, \quad (6.22)$$

where n_c is the critical plasma density corresponding to a specific wavelength of light λ . Plasma critical density is inversely proportional to the square of the light wavelength. Different wavelengths of probe light correspond to different critical

densities, and probe beams with short wavelengths correspond to higher critical plasma densities,

$$n_{1064} \approx 0.98 \times 10^{27} m^{-3}, \quad (6.23)$$

$$n_{532} \approx 3.94 \times 10^{27} m^{-3}, \quad (6.24)$$

$$\text{and} \quad (6.25)$$

$$n_{355} \approx 8.85 \times 10^{27} m^{-3}. \quad (6.26)$$

Fig. 6.4 shows the transmitted probe light as a function of plasma density. Here the initial target thickness is 30 nm, and the critical plasma density of 800 nm normalizes each plasma density. (a) and (b) respectively show the probe light transmittance triggered by different intensity pre-pulses. When the plasma density

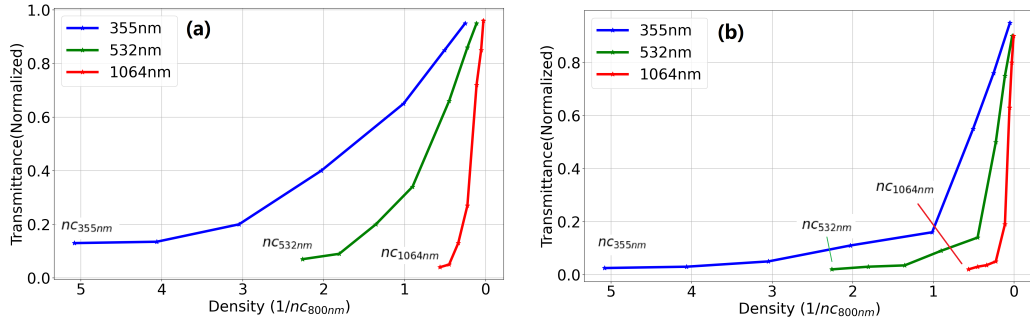


Fig. 6.4: Numerical calculation results of probe light transmittance as a function of peak plasma densities. The initial target is 30 nm. (a) The pre-pulse intensity is $5 \times 10^{13} \text{W/cm}^2$, and (b) The pre-pulse intensity is $3 \times 10^{15} \text{W/cm}^2$. The plasma density has been normalized by $n_{C800\text{nm}}$.

falls below the critical density of the corresponding wavelength of light, the decrease in plasma density does not lead to a linear increase in transmitted light. Instead, the transmitted probe light remains nearly constant over a range of plasma densities before rapidly increasing. This is because the absorption rate of plasma is influenced by its scale length and density at the same time. While the maximum density decreases, the scale length of the plasma increases, leading to a nearly constant absorption rate of probe light within a certain range. This phenomenon is also evident in numerical calculations for the 90 nm target, as shown in Fig. 6.5.

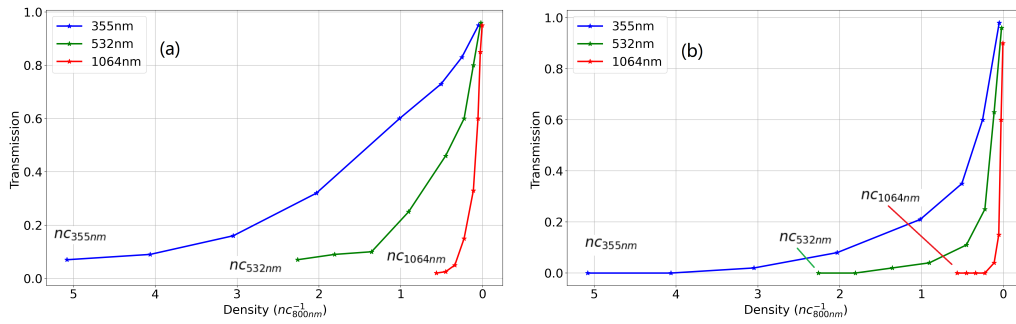


Fig. 6.5: Numerical calculation results of probe light transmittance as a function of peak plasma densities. The initial target is 90 nm. (a) The pre-pulse intensity is $5 \times 10^{13} \text{W/cm}^2$, and (b) The pre-pulse intensity is $3 \times 10^{15} \text{W/cm}^2$. The plasma density has been normalized by n_{C800nm} .

6.2 Experiment

6.2.1 Experimental Setup

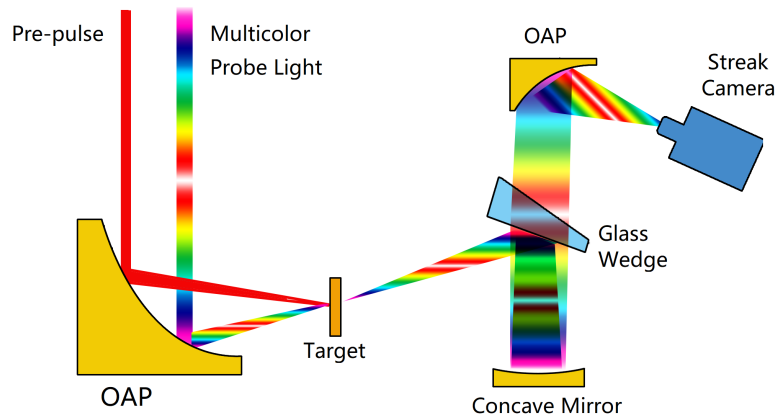


Fig. 6.6: Schematic of experimental apparatus and diagnostic layout. The pre-pulse and multicolour probe lights are focused on the target by the same OAP. The multicolour probe lights pass through the target and are reflected on a concave mirror by a glass wedge. The concave mirror collimates the probe beams. Finally, the collimated beams are focused on the streak camera by the second OAP out of the chamber. The streak camera simultaneously records the transmitted light of the different probe lights.

The experimental setup, similar to that used in the proton acceleration experiment, was also conducted with the JETi200 laser system, as shown in Fig.6.6. The pre-pulse and probe beams are simultaneously focused on the target using an 18 cm focal

length OAP. The multicolor probe beam is produced by Q-smart laser system. The first surface of a glass wedge reflects the probe beams to the collimation mirror, and the collimated light passes through the same wedge before being refocused onto the streak camera by another OAP. The glass wedge separates light of varying wavelengths, with 1064 nm, 532 nm, and 355 nm probe beams being used to detect plasma density. The probe beam duration is 5 ns and has an intensity of $5 \times 10^{11} \text{W/cm}^2$, which is below the formvar foil's laser-induced damage threshold. The probe light's initial diameter is 6.5 mm, and an expander system magnifies the beam size to achieve a smaller focus on the target plane, resulting in focus sizes with FWHM diameters of $7 \mu\text{m}$ (1064 nm), $5.4 \mu\text{m}$ (532 nm), and $4 \mu\text{m}$ (355 nm). The spatial overlap of the three-color probe lights is confirmed by separately irradiating the same needle, as shown in Fig.6.7. The pre-pulse focus has a diameter of approximately $20 \mu\text{m}$ FWHM and an intensity of $5 \times 10^{13} \text{W/cm}^2$ or $3 \times 10^{15} \text{W/cm}^2$ in the experiment.

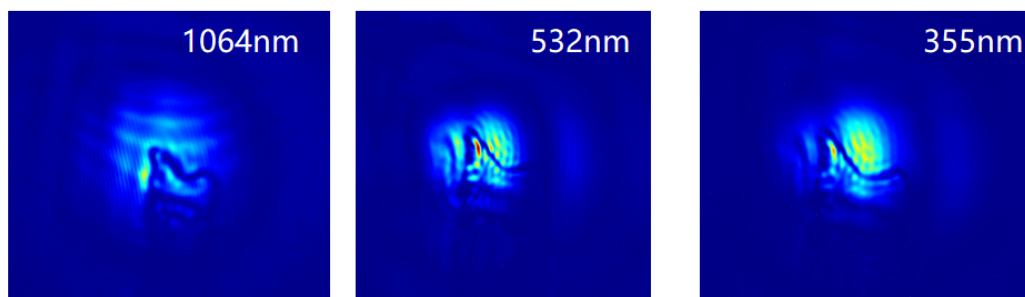


Fig. 6.7: A glass needle is placed at the focus of the pre-pulse, and probe lights are used to illuminate the needle separately. Ensure that the spatial focus of the probe lights overlaps with the pre-pulse focus.

6.2.2 Experimental Results

1. 30 nm Target

Fig.6.8 shows the raw images obtained by the streak camera, with a sweeping time of 1 ns, when the 30 nm target is irradiated with a pre-pulse of $3 \times 10^{15} \text{W/cm}^2$. The glass wedge disperses the probe beams by different wavelengths, with 1064 nm, 532 nm, and 355 nm shown from left to right. The 800 nm pre-pulse appears between the 1064 nm and 532 nm beams. In each figure, three distinct plasma shutter-

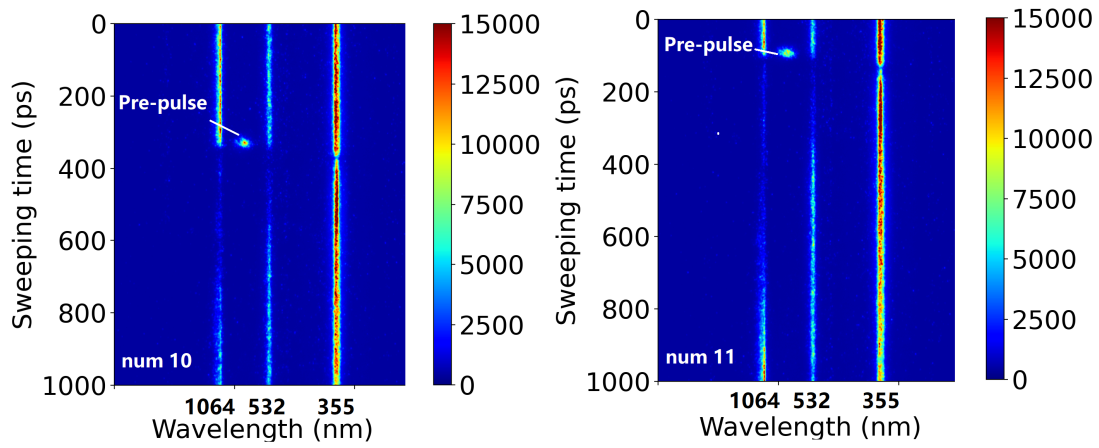


Fig. 6.8: Two raw images were recorded by the streak camera. Target thicknesses are 30 nm and pre-pulse intensity is $3 \times 10^{15} \text{W}/\text{cm}^2$. From left to right are 1064 nm, 532 nm, and 355 nm probe beams, respectively. The pre-pulses with an 800 nm wavelength are marked. The pre-pulse creates the overdense plasma and blocks the probe beams. Then, the plasma density gradually decreases with time, and the probe lights of different wavelengths pass through the plasma sequentially.

times can be observed, caused by the overdense plasma triggered by the pre-pulse. As the plasma density gradually decreases over time, the probe light of different wavelengths penetrates their respective critical density plasma sequentially.

Fig.6.9 illustrates the temporal evolution of plasma density and transmittance of the probe beams, where the plasma density takes into account the numerical absorption correction discussed in the previous section. Time $T = 0$ ps corresponds to the overdense plasma triggering moment. It blocks all of the probe beams. Then, the probe beam with 355 nm wavelength first penetrates the plasma due to its shorter wavelength, which allows it to penetrate the relatively high-density plasma. The first obvious feature is that the 355 nm probe beam takes tens of picoseconds to fully penetrate the plasma, while the 532 nm and 1064 nm probe light take longer to penetrate the plasma. This indicates a non-constant plasma expansion speed during the expansion process. During the initial stage of overdense plasma formation, the dense plasma contains a higher number of particles per unit volume. As a result, collisions between particles in the dense plasma are more frequent and energetic. Additionally, the higher particle density in the dense plasma leads to a stronger mutual repulsion between particles, contributing to its faster expansion[142]. As the plasma expands, the thermal electrons gradually transfer kinetic energy to the

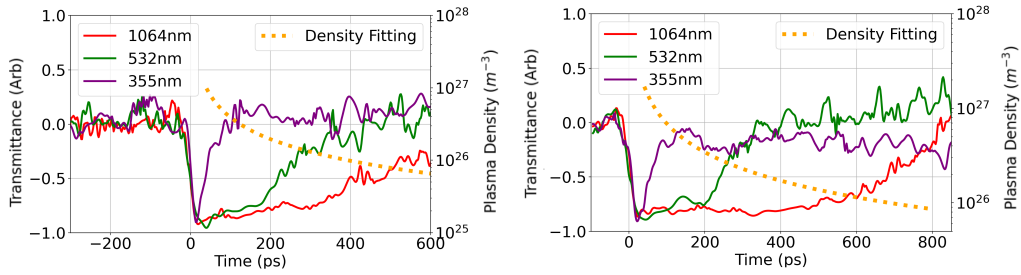


Fig. 6.9: Transmittance and the plasma density against the time. The sweeping time is 1 ns with a 22 ps resolution, as shown in Fig.3.6. The plasma density is calculated from the transmittance of the probe light in section 6.1.3. Pre-pulse produces the overdense plasma, and the probe beams are blocked at $T = 0$ ps, forming plasma shutter-times. With decreasing plasma density, the probe beams penetrate the plasma sequentially. Different wavelengths of probe light correspond to different penetration times (from no light to light transmission), which proves that the expansion speed of plasma slows down gradually.

ions, reaching a quasi-equilibrium, and the expansion speed decreases. The second obvious feature is that the transmittance of the 532 nm probe beam does not increase linearly after penetrating the plasma, instead remaining unchanged or gradually increasing between 80 ps - 200 ps, followed by rapid increase between 200 ps - 300 ps before full penetration. This phenomenon confirms previous numerical calculations in section 6.1.3 that show the collisional absorption of probe light is affected by both plasma density and scale length.

2. 90 nm Target

The 90 nm target is irradiated with a pre-pulse of $5 \times 10^{13} \text{W}/\text{cm}^2$, and the evolution of plasma density with time is shown in Fig.6.10. The sweeping times for num 82 and num 87 are 2 ns and 5 ns, respectively, with time resolutions of 26 ps and 53 ps. In Figure num 82, during the process of the 355nm probe light penetrating the plasma, specifically from $T = 100$ ps to $T = 600$ ps, the slope of the transmitted light gradually slows down. Similarly, this phenomenon demonstrates that the expansion speed of the plasma slows down with the increasing of the time.

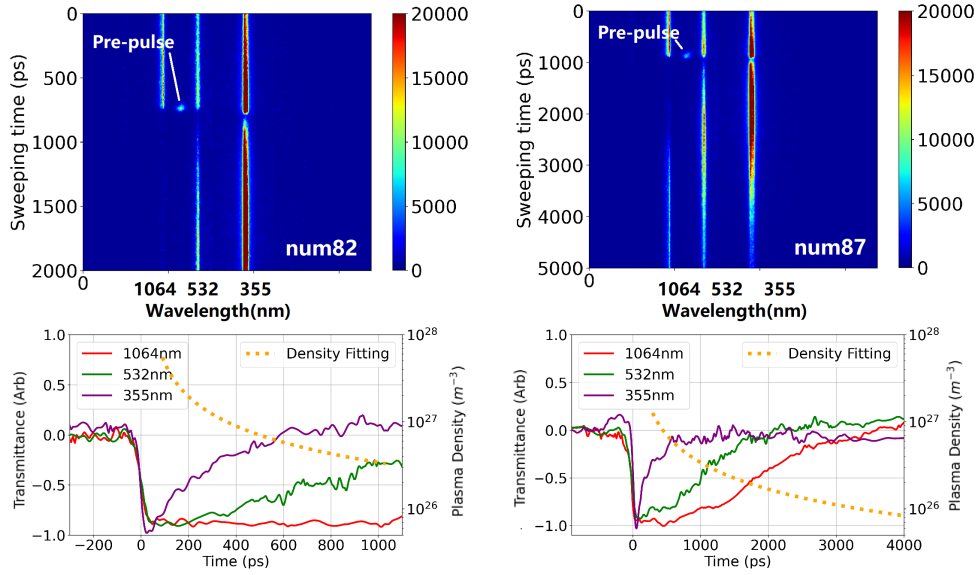


Fig. 6.10: The 90 nm target is irradiated with a pre-pulse of $5 \times 10^{13} \text{W}/\text{cm}^2$. The sweeping times of num 82 and num 87 are 2 ns and 5 ns respectively. The upper part shows the raw image, while the lower part shows the corresponding transmittance and plasma density evolution over time. The plasma density is calculated from the transmittance of the probe light in section 6.1.3.

6.2.3 Comparison of Experimental Results with Numerical Model

The previous evolution of the pre-plasma was to study the effect of femtosecond short pre-pulses on the expansion of thin foils by simulation, and developed a numerical model to describe the evolution of the foil as a function of intensity and time [143]. The numerical model can be described as

$$n(t) = \frac{n_0 d_0}{\sqrt{\frac{\pi}{4 \ln 2} \omega}} = \frac{n_0 d_0}{\sqrt{\frac{\pi}{4 \ln 2} v_{exp} t}}, \quad (6.27)$$

where $n(t)$ is the electron density as a function of time, n_0 is the electron density of the target and d_0 is the initial plasma thickness. v_{exp} is the plasma expansion velocity. According to the various pre-pulse intensities, the plasma expansion velocity, v_{exp} , can be well represented by

$$v_{exp} = 4.4 \mu\text{m}/\text{ps} \text{ when } I_0 \leq 10^{12} \text{W}/\text{cm}^2, \quad (6.28)$$

$$v_{exp} = A \times I_0^{1/2} + B \text{ when } I_0 > 10^{12} \text{W}/\text{cm}^2, \quad (6.29)$$

where I_0 is laser intensity. A and B are fitting parameters, $A = 2 \times 10^{-9} \frac{\mu\text{m}/\text{ps}}{\sqrt{\text{W}/\text{cm}^2}}$ and $B = 0.0024 \mu\text{m}/\text{ps}$, respectively.

In the experiment, the pre-pulse intensity $5 \times 10^{13} \text{W}/\text{cm}^2$ and $3 \times 10^{15} \text{W}/\text{cm}^2$ are insufficient to fully ionize the targets. As an approximation, the electron density of the target n_0 is replaced by the initial plasma density n_{ionized} . n_{ionized} is the plasma density after the pre-pulse ionization. When the $5 \times 10^{13} \text{W}/\text{cm}^2$ pre-pulse creates the pre-plasma, the ionization mechanism is Above-threshold ionization. The final kinetic energy of the electron can be expressed as

$$E_{kin} = (n + m)\hbar\omega - E_{ion}. \quad (6.30)$$

Here, E_{kin} is the final kinetic energy of the electron, n is the minimum number of photons required to overcome the binding energy, m is the excess absorbed, and E_{ion} is the ionization energy. The energy of a single photon with a wavelength of 800 nm is 1.55 eV, and the first ionization energies of hydrogen, oxygen, and carbon atoms are 13.6 eV, 11.2 eV, and 13.6 eV, respectively. As a rule of thumb, it takes about 9 photons to ionize a single atom. Assuming 50% of the atoms in the focal point are ionized, the initial density after the pre-pulse ionization is approximately $n_{\text{ionized}} \approx 30n_{c800\text{nm}}$.

When the pre-pulse of $3 \times 10^{15} \text{W}/\text{cm}^2$ creates the pre-plasma, the ionization mechanism is dominated by Tunneling ionization due to the Keldysh parameter, $\gamma < 1$ [17, 15]. Based on previous experiments [144], it has been observed that nitrogen gas molecules undergo ionization when exposed to a laser with an intensity of $2 \times 10^{15} \text{W}/\text{cm}^2$, resulting in the formation of the highest valence state as N^{3+} . The ionization energy corresponding to the N^{3+} is 47.4 eV. Assume that for the formvar target, as long as the ionization energy of the element is lower than 47.4 eV, electrons can be completely ionized. The maximum plasma density is $n_{\text{ionized}} \approx 100n_{c800\text{nm}}$.

Experimental results for 30 nm and 90 nm Formvar targets are presented in Fig. 6.11 and Fig. 6.12, respectively, with plasma density normalized to the critical plasma density at a wavelength of 800 nm $n_{c800\text{nm}}$. Purple areas in the figures represent different initial densities. The experimental results show good agreement with the

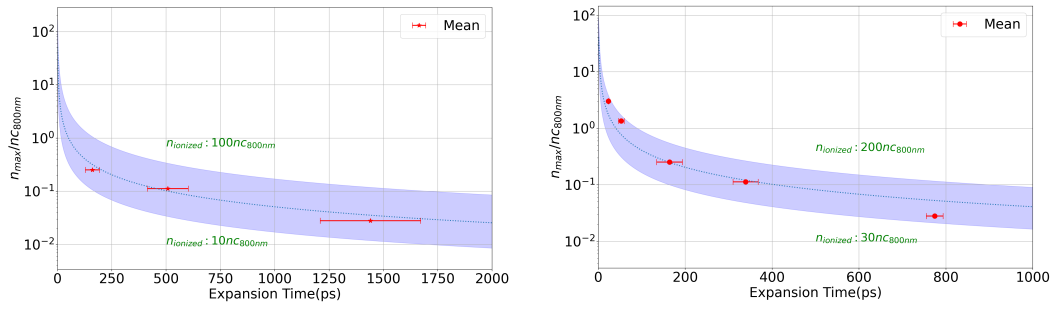


Fig. 6.11: Experimental results of maximum electron densities as a function of expansion time. The target thickness is 30 nm. (a) pre-pulse intensity is $5 \times 10^{13} \text{W/cm}^2$ and the dotted line represents the model[143] with an initial density of $n_{\text{ionized}} = 30 \text{n}_{\text{c}800\text{nm}}$. (b) pre-pulse intensity is $3 \times 10^{15} \text{W/cm}^2$ and the dotted line represents the model with an initial density of $n_{\text{ionized}} = 100 \text{n}_{\text{c}800\text{nm}}$. For reference, the purple areas represent different initial densities.

model when the electron density of the target n_0 is replaced by the initial plasma density n_{ionized} in the model. Both experimental data and models show that the plasma density decreases drastically during the initial period of plasma generation. The rapid expansion of the dense plasma generated by the pre-pulse results in a rapid decrease in plasma density due to the high temperature and pressure. Subsequently, the plasma expands more slowly and reaches a stable state, resulting in a slighter decrease in plasma density over time.

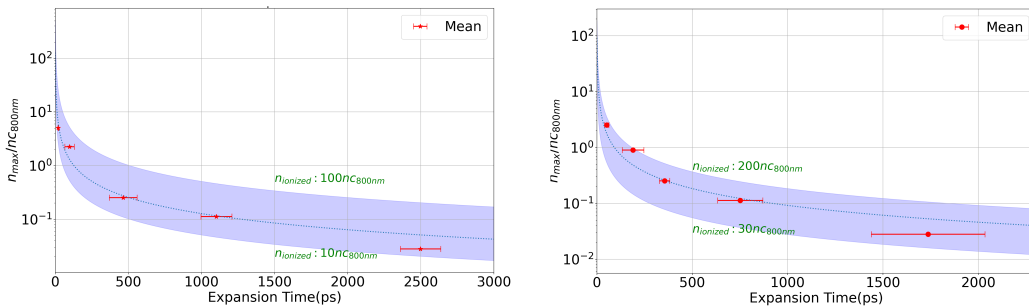


Fig. 6.12: Experimental results of maximum electron densities as a function of expansion time. The target thickness is 90 nm. (a) pre-pulse intensity is $5 \times 10^{13} \text{W/cm}^2$ and the dotted line represents the model with an initial density of $n_{\text{ionized}} = 30 \text{n}_{\text{c}800\text{nm}}$. (b) pre-pulse intensity is $3 \times 10^{15} \text{W/cm}^2$ and the dotted line represents the model with an initial density of $n_{\text{ionized}} = 100 \text{n}_{\text{c}800\text{nm}}$. For reference, the purple areas represent different initial densities.

6.3 Summary

This chapter presents a quantitative study on the evolution of plasma maximum density over time. Multicolor probe light is used to irradiate dense plasma, and its transmittance is measured by streak camera. By numerically solving the Helmholtz equation, the absorption rate of the probe light by critical plasma is calculated, providing an explanation for the observed experimental phenomenon. The results indicate that both the maximum density and scale length of the plasma significantly affect the absorption rate of the laser. Furthermore, by comparing the experimental findings with a previous numerical model, it is demonstrated that the previous model accurately predicts the evolution process of dense plasma. Potential application in the future to create near critical density plasmas for ion wave breaking acceleration (IWBA)[[136](#), [137](#)].

Summary Outlook

7.1 Summary

In this dissertation, laser-driven proton acceleration from the solid target was investigated. Based on the excellent high-contrast laser system, the pre-pulse and spontaneous radiation of the laser itself are effectively suppressed. Combined with the back-end plasma mirror system, it creates excellent experimental conditions for the nanometer scale target proton acceleration. Experimental results show that, based on a high-contrast laser and using a circularly polarized laser, monoenergetic proton beams can be generated when the thickness of the target is less than 90 nm. The highest energy achieved is up to 35 MeV, generated from a 40 nm planar target. The phenomenon of a monoenergetic proton beam disappears when the same solid target is driven with a linearly polarized laser. The research on the energy scale of protons shows that when circularly polarized lasers are used to drive 40 nm targets and 90 nm targets, the energy of protons is proportional to I and $I^{0.5}$, respectively. The results prove that the mechanism for accelerating the 40 nm target is mainly Light-Sail RPA, while the mechanism for driving the 90 nm target is mainly TNSA. Through the PIC 2D simulation of the experiment, the subtle differences in the acceleration process of thin targets with different thicknesses were explored. Due to the use of multi-component thin targets, namely oxygen, carbon and hydrogen, for a 40 nm target, protons are first accelerated and separated from heavy ions when they interact with the target at the leading edge of the laser. The heavy ions act as a buffer when the main pulse arrives. And modulate the accelerating electric field E_x . The protons in the focal spot range are accelerated as a whole. Isolated proton peaks are formed. For thick targets, isolated proton peaks cannot be formed when the protons interact with the target at the laser front. After being accelerated by laser light pressure, the high-energy proton, positioned at the front of the heavy ion, experiences an increase in energy due to the Coulomb repulsion between the

proton and the heavy ion. This repulsion further extends the acceleration time for the high-energy proton.

For the second experiment, near critical density plasma diagnosis, the multicolour probe lights were focused on the non-relativistic plasma, and the evolution process of the maximum density of the non-relativistic plasma with time was explored by detecting the transmitted light. The nanometer-thick thin target used in the experiment is widely used in laser particle acceleration experiments. Due to the inevitable pre-pulse in the high-energy laser, the pre-expansion process of the thin target will seriously affect the acceleration process of the main pulse to the plasma. And it also has certain challenges for the detection of dense plasma on the micron scale. Previous studies of this process were mainly based on numerical fluid models. The evolution process of the dense plasma is quantitatively measured through experiments, and combined with numerical calculations, the experimental phenomena are explained. The experimental results indicate that both the maximum density and scale length of the plasma significantly affect probe light absorption. Furthermore, compare experimental results with a previous numerical model, proving that the model can better predict the evolution process of dense plasma.

7.2 Outlook

Laser particle acceleration is a rapidly developing field, greatly spurred by the success of Lawrence Livermore National Laboratory's laser nuclear fusion ignition. This achievement has injected strong impetus into the field, which has the potential to revolutionize energy production, medical treatments, and fundamental scientific research. While impressive results have already been achieved, researchers have identified several methods to further enhance ion energy. These include increasing laser intensity, optimizing target geometries, employing multiple laser pulses, and exploring new target materials. By refining and advancing these techniques, we can unlock the full potential of laser ion acceleration across various applications. As the field matures, we anticipate increased collaboration among interdisciplinary researchers and institutions, as well as heightened industry involvement. This collaborative effort holds the promise of developing unimaginable applications and technologies. Although the outlook for laser ion acceleration is promising, significant challenges must be overcome through sustained investment and collaboration to fully realize the potential of this exciting technology.

Bibliography

- [1] Wentao Wang, Ke Feng, Lintong Ke, Changhai Yu, Yi Xu, Rong Qi, Yu Chen, Zhiyong Qin, Zhijun Zhang, Ming Fang, et al. Free-electron lasing at 27 nanometres based on a laser wakefield accelerator. *Nature*, 595(7868):516–520, 2021.
- [2] M Borghesi, AJ Mackinnon, D Hv Campbell, DG Hicks, S Kar, Pv K Patel, D Price, L Romagnani, A Schiavi, and O Willi. Multi-mev proton source investigations in ultraintense laser-foil interactions. *Physical Review Letters*, 92(5):055003, 2004.
- [3] TE Cowan, J Fuchs, H Ruhl, A Kemp, P Audebert, M Roth, R Stephens, I Barton, A Blazevic, E Brambrink, et al. Ultralow emittance, multi-mev proton beams from a laser virtual-cathode plasma accelerator. *Physical review letters*, 92(20):204801, 2004.
- [4] PK Patel, AJ Mackinnon, MH Key, TE Cowan, ME Foord, M Allen, DF Price, H Ruhl, PT Springer, and R Stephens. Isochoric heating of solid-density matter with an ultrafast proton beam. *Physical review letters*, 91(12):125004, 2003.
- [5] JA Cobble, RP Johnson, TE Cowan, N Renard-Le Galloudec, and M Allen. High resolution laser-driven proton radiography. *Journal of applied physics*, 92(4):1775–1779, 2002.

- [6] Valentin Fedosseev, Katerina Chrysalidis, Thomas Day Goodacre, Bruce Marsh, Sebastian Rothe, Christoph Seiffert, and Klaus Wendt. Ion beam production and study of radioactive isotopes with the laser ion source at isolde. *Journal of Physics G: Nuclear and Particle Physics*, 44(8):084006, 2017.
- [7] C Bamber, SJ Boege, T Koffas, T Kotseroglou, AC Melissinos, DD Meyerhofer, DA Reis, W Ragg, C Bula, KT McDonald, et al. Studies of nonlinear qed in collisions of 46.6 gev electrons with intense laser pulses. *Physical Review D*, 60(9):092004, 1999.
- [8] Thomas Heinzl and Anton Ilderton. A lorentz and gauge invariant measure of laser intensity. *Optics communications*, 282(9):1879–1883, 2009.
- [9] Maria Göppert-Mayer. Über elementarakte mit zwei quantensprüngen. *Annalen der Physik*, 401(3):273–294, 1931.
- [10] P Agostini, G Barjot, J Bonnal, G Mainfray, C Manus, and J Morellec. Multiphoton ionization of hydrogen and rare gases. *IEEE Journal of Quantum Electronics*, 4(10):667–669, 1968.
- [11] Warner L Peticolas, John P Goldsborough, and KE Rieckhoff. Double photon excitation in organic crystals. *Physical Review Letters*, 10(2):43, 1963.
- [12] Pierre Agostini, F Fabre, Gérard Mainfray, Guillaume Petite, and N Ko Rahman. Free-free transitions following six-photon ionization of xenon atoms. *Physical Review Letters*, 42(17):1127, 1979.
- [13] Y Gontier and M Trahin. Energetic electron generation by multiphoton absorption. *Journal of Physics B: Atomic and Molecular Physics*, 13(22):4383, 1980.
- [14] P Kruit, J Kimman, Harm G Muller, and MJ Van der Wiel. Electron spectra from multiphoton ionization of xenon at 1064, 532, and 355 nm. *Physical Review A*, 28(1):248, 1983.

- [15] LV Keldysh et al. Ionization in the field of a strong electromagnetic wave. *Sov. Phys. JETP*, 20(5):1307–1314, 1965.
- [16] AM Perelomov, VS Popov, and MV Terent'ev. Ionization of atoms in an alternating electric field. *Sov. Phys. JETP*, 23(5):924–934, 1966.
- [17] Leonid V Keldysh. Ionization in the field of a strong electromagnetic wave. *Zh. Eksperim. i Teor. Fiz.*, 47, 1964.
- [18] Andrea Macchi. *A superintense laser-plasma interaction theory primer*. Springer Science & Business Media, 2013.
- [19] Paul Gibbon. *Short pulse laser interactions with matter: an introduction*. World Scientific, 2005.
- [20] Hao-Ming Shen. Plasma waveguide: A concept to transfer electromagnetic energy in space. *Journal of applied physics*, 69(10):6827–6835, 1991.
- [21] Stephan Reuter, Joao Santos Sousa, Gabi Daniel Stancu, and Jean-Pierre Hubertus van Helden. Review on vuv to mir absorption spectroscopy of atmospheric pressure plasma jets. *Plasma Sources Science and Technology*, 24(5):054001, 2015.
- [22] JP Geindre, P Audebert, A Rousse, F Fallies, JC Gauthier, A Mysyrowicz, A Dos Santos, G Hamoniaux, and A Antonetti. Frequency-domain interferometer for measuring the phase and amplitude of a femtosecond pulse probing a laser-produced plasma. *Optics letters*, 19(23):1997–1999, 1994.
- [23] AA Ovsyannikov and Mikhail Fedorovich Zhukov. *Plasma diagnostics*. Cambridge Int Science Publishing, 2000.
- [24] A Sävert, SPD Mangles, M Schnell, E Siminos, JM Cole, M Leier, M Reuter, MB Schwab, M Möller, K Poder, et al. Direct observation of the injection dy-

namics of a laser wakefield accelerator using few-femtosecond shadowgraphy. *Physical review letters*, 115(5):055002, 2015.

- [25] M Tatarakis, JR Davies, P Lee, PA Norreys, NG Kassapakis, FN Beg, AR Bell, MG Haines, and AE Dangor. Plasma formation on the front and rear of plastic targets due to high-intensity laser-generated fast electrons. *Physical review letters*, 81(5):999, 1998.

- [26] Matthew Zepf, EL Clark, K Krushelnick, FN Beg, C Escoda, AE Dangor, MIK Santala, M Tatarakis, IF Watts, PA Norreys, et al. Fast particle generation and energy transport in laser-solid interactions. *Physics of Plasmas*, 8(5):2323–2330, 2001.

- [27] Stephen P Hatchett, Curtis G Brown, Thomas E Cowan, Eugene A Henry, Joy S Johnson, Michael H Key, Jeffrey A Koch, A Bruce Langdon, Barbara F Lasinski, Richard W Lee, et al. Electron, photon, and ion beams from the relativistic interaction of petawatt laser pulses with solid targets. *Physics of Plasmas*, 7(5):2076–2082, 2000.

- [28] SC Wilks, AB Langdon, TE Cowan, M Roth, M Singh, S Hatchett, MH Key, D Pennington, A MacKinnon, and RA Snavely. Energetic proton generation in ultra-intense laser–solid interactions. *Physics of plasmas*, 8(2):542–549, 2001.

- [29] Patrick Mora. Plasma expansion into a vacuum. *Physical Review Letters*, 90(18):185002, 2003.

- [30] Patrick Mora and R Pellat. Self-similar expansion of a plasma into a vacuum. *The Physics of Fluids*, 22(12):2300–2304, 1979.

- [31] SC Wilks, WL Kruer, M Tabak, and AB Langdon. Absorption of ultra-intense laser pulses. *Physical review letters*, 69(9):1383, 1992.

- [32] Malte Kaluza, Jörg Schreiber, Marko IK Santala, George D Tsakiris, Klaus Eidmann, Jürgen Meyer-ter Vehn, and Klaus J Witte. Influence of the laser prepulse on proton acceleration in thin-foil experiments. *Physical review letters*, 93(4):045003, 2004.
- [33] J Fuchs, TE Cowan, P Audebert, H Ruhl, L Gremillet, A Kemp, M Allen, A Blazevic, J-C Gauthier, M Geissel, et al. Spatial uniformity of laser-accelerated ultrahigh-current mev electron propagation in metals and insulators. *Physical review letters*, 91(25):255002, 2003.
- [34] J Fuchs, P Antici, E d’Humières, E Lefebvre, Marco Borghesi, E Brambrink, CA Cecchetti, Malte Kaluza, Victor Malka, M Manclossi, et al. Laser-driven proton scaling laws and new paths towards energy increase. *Nature physics*, 2(1):48–54, 2006.
- [35] Hiroyuki Daido, Mamiko Nishiuchi, and Alexander S Pirozhkov. Review of laser-driven ion sources and their applications. *Reports on progress in physics*, 75(5):056401, 2012.
- [36] Björn Manuel Hegelich, BJ Albright, J Cobble, K Flippo, S Letzring, M Paffett, H Ruhl, Jörg Schreiber, RK Schulze, and JC Fernández. Laser acceleration of quasi-monoenergetic mev ion beams. *Nature*, 439(7075):441–444, 2006.
- [37] H Schwoerer, S Pfotenhauer, O Jäckel, K-U Amthor, B Liesfeld, W Ziegler, R Sauerbrey, KWD Ledingham, and T Esirkepov. Laser-plasma acceleration of quasi-monoenergetic protons from microstructured targets. *Nature*, 439(7075):445–448, 2006.
- [38] A Noda, S Nakamura, Y Iwashita, S Sakabe, M Hashida, T Shirai, S Shimizu, H Tongu, H Ito, H Souda, et al. Phase rotation scheme of laser-produced ions for reduction of the energy spread. *Laser Physics*, 16(4):647–653, 2006.
- [39] Masahiro Ikegami, Shu Nakamura, Yoshihisa Iwashita, Toshiyuki Shirai, Hikaru Souda, Yujiro Tajima, Mikio Tanabe, Hiromu Tongu, Hiroyuki Itoh,

Hiroki Shintaku, et al. Radial focusing and energy compression of a laser-produced proton beam by a synchronous rf field. *Physical Review Special Topics-Accelerators and Beams*, 12(6):063501, 2009.

- [40] Toma Toncian, Marco Borghesi, Julien Fuchs, Emmanuel d’Humières, Patrizio Antici, Patrick Audebert, Erik Brambrink, Carlo Alberto Cecchetti, Ariane Pipahl, Lorenzo Romagnani, et al. Ultrafast laser-driven microlens to focus and energy-select mega-electron volt protons. *Science*, 312(5772):410–413, 2006.
- [41] M Nishiuchi, I Daito, M Ikegami, H Daido, M Mori, S Orimo, K Ogura, A Sagisaka, A Yogo, AS Pirozhkov, et al. Focusing and spectral enhancement of a repetition-rated, laser-driven, divergent multi-mev proton beam using permanent quadrupole magnets. *Applied Physics Letters*, 94(6):061107, 2009.
- [42] M Hildred Blewett. Cern symposium on high-energy accelerators and pion physics. *Physics Today*, 9(11):18, 1956.
- [43] Wll Kruer and Kent Estabrook. $J \times b$ heating by very intense laser light. *The Physics of fluids*, 28(1):430–432, 1985.
- [44] Andrea Macchi, Federica Cattani, Tatiana V. Liseykina, and Fulvio Cornolti. Laser acceleration of ion bunches at the front surface of overdense plasmas. *Phys. Rev. Lett.*, 94:165003, Apr 2005.
- [45] A. P. L. Robinson. Production of high energy protons with hole-boring radiation pressure acceleration. *Physics of Plasmas*, 18(5):056701, 2011.
- [46] A P L Robinson, P Gibbon, M Zepf, S Kar, R G Evans, and C Bellei. Relativistically correct hole-boring and ion acceleration by circularly polarized laser pulses. *Plasma Physics and Controlled Fusion*, 51(2):024004, jan 2009.
- [47] T. Esirkepov, M. Borghesi, S. V. Bulanov, G. Mourou, and T. Tajima. Highly efficient relativistic-ion generation in the laser-piston regime. *Phys. Rev. Lett.*,

92:175003, Apr 2004.

- [48] Andrea Macchi, Silvia Veghini, and Francesco Pegoraro. “light sail” acceleration reexamined. *Phys. Rev. Lett.*, 103:085003, Aug 2009.
- [49] N Naumova, T Schlegel, VT Tikhonchuk, C Labaune, IV Sokolov, and G Mourou. Hole boring in a dt pellet and fast-ion ignition with ultraintense laser pulses. *Physical Review Letters*, 102(2):025002, 2009.
- [50] Y Ping, AJ Kemp, L Divol, MH Key, PK Patel, KU Akli, FN Beg, S Chawla, CD Chen, RR Freeman, et al. Dynamics of relativistic laser-plasma interaction on solid targets. *Physical review letters*, 109(14):145006, 2012.
- [51] Natsumi Iwata, Sadaoki Kojima, Yasuhiko Sentoku, Masayasu Hata, and Kunioki Mima. Plasma density limits for hole boring by intense laser pulses. *Nature communications*, 9(1):1–7, 2018.
- [52] XQ Yan, C Lin, Zheng-Ming Sheng, ZY Guo, BC Liu, YR Lu, JX Fang, JE Chen, et al. Generating high-current monoenergetic proton beams by a circularly-polarized laser pulse in the phase-stableacceleration regime. *Physical review letters*, 100(13):135003, 2008.
- [53] Andrea Macchi, Silvia Veghini, and Francesco Pegoraro. “light sail” acceleration reexamined. *Physical review letters*, 103(8):085003, 2009.
- [54] Bin Qiao, Matthew Zepf, Marco Borghesi, and Michael Geissler. Stable gev ion-beam acceleration from thin foils by circularly polarized laser pulses. *Physical review letters*, 102(14):145002, 2009.
- [55] O Klimo, J Psikal, J Limpouch, and VT Tikhonchuk. Monoenergetic ion beams from ultrathin foils irradiated by ultrahigh-contrast circularly polarized laser pulses. *Physical Review Special Topics-Accelerators and Beams*, 11(3):031301, 2008.

- [56] Eric Esarey, CB Schroeder, and WP Leemans. Physics of laser-driven plasma-based electron accelerators. *Reviews of modern physics*, 81(3):1229, 2009.
- [57] S. S. Bulanov, E. Esarey, C. B. Schroeder, S. V. Bulanov, T. Zh. Esirkepov, M. Kando, F. Pegoraro, and W. P. Leemans. Enhancement of maximum attainable ion energy in the radiation pressure acceleration regime using a guiding structure. *Phys. Rev. Lett.*, 114:105003, Mar 2015.
- [58] SV Bulanov, T Zh Esirkepov, M Kando, F Pegoraro, SS Bulanov, CGR Geddes, CB Schroeder, E Esarey, and WP Leemans. Ion acceleration from thin foil and extended plasma targets by slow electromagnetic wave and related ion-ion beam instability. *Physics of Plasmas*, 19(10):103105, 2012.
- [59] Albert Einstein. Zur elektrodynamik bewegter körper. *Annalen der physik*, 4, 1905.
- [60] Konstantinos Kifonidis, T Plewa, H-Th Janka, and E Müller. Non-spherical core collapse supernovae-i. neutrino-driven convection, rayleigh-taylor instabilities, and the formation and propagation of metal clumps. *Astronomy & Astrophysics*, 408(2):621–649, 2003.
- [61] Francesco Pegoraro and SV Bulanov. Photon bubbles and ion acceleration in a plasma dominated by the radiation pressure of an electromagnetic pulse. *Physical review letters*, 99(6):065002, 2007.
- [62] Lin Yin, BJ Albright, BM Hegelich, and JC Fernández. Gev laser ion acceleration from ultrathin targets: The laser break-out afterburner. *Laser and Particle Beams*, 24(2):291–298, 2006.
- [63] L Yin, BJ Albright, KJ Bowers, D Jung, JC Fernández, and BM Hegelich. Three-dimensional dynamics of breakout afterburner ion acceleration using high-contrast short-pulse laser and nanoscale targets. *Physical review letters*, 107(4):045003, 2011.

- [64] L Yin, BJ Albright, BM Hegelich, Kevin J Bowers, KA Flippo, TJT Kwan, and JC Fernández. Monoenergetic and gev ion acceleration from the laser breakout afterburner using ultrathin targets. *Physics of plasmas*, 14(5):056706, 2007.
- [65] Andreas Henig, Daniel Kiefer, K Markey, DC Gautier, KA Flippo, S Letzring, RP Johnson, T Shimada, L Yin, BJ Albright, et al. Enhanced laser-driven ion acceleration in the relativistic transparency regime. *Physical review letters*, 103(4):045002, 2009.
- [66] L Yin, BJ Albright, D Jung, RC Shah, S Palaniyappan, KJ Bowers, Andreas Henig, JC Fernández, and Björn M Hegelich. Break-out afterburner ion acceleration in the longer laser pulse length regime. *Physics of Plasmas*, 18(6):063103, 2011.
- [67] BM Hegelich, I Pomerantz, L Yin, HC Wu, Daniel Jung, BJ Albright, DC Gautier, S Letzring, S Palaniyappan, R Shah, et al. Laser-driven ion acceleration from relativistically transparent nanotargets. *New Journal of Physics*, 15(8):085015, 2013.
- [68] T Zh Esirkepov, SV Bulanov, K Nishihara, T Tajima, Francesco Pegoraro, VS Khoroshkov, K Mima, H Daido, Y Kato, Y Kitagawa, et al. Proposed double-layer target for the generation of high-quality laser-accelerated ion beams. *Physical review letters*, 89(17):175003, 2002.
- [69] T Esirkepov, M Yamagiwa, and T Tajima. Laser ion-acceleration scaling laws seen in multiparametric particle-in-cell simulations. *Physical review letters*, 96(10):105001, 2006.
- [70] T Esirkepov, R Bingham, S Bulanov, T Honda, K Nishihara, and Francesco Pegoraro. Coulomb explosion of a cluster irradiated by a high intensity laser pulse. *Laser and Particle Beams*, 18(3):503–506, 2000.
- [71] K Nishihara, H Amitani, M Murakami, SV Bulanov, and T Zh Esirkepov. High energy ions generated by laser driven coulomb explosion of cluster.

Nuclear Instruments and Methods in Physics Research Section A: Accelerators, Spectrometers, Detectors and Associated Equipment, 464(1-3):98–102, 2001.

- [72] V Yu Bychenkov and VF Kovalev. Coulomb explosion in a cluster plasma. *Plasma physics reports*, 31(2):178–183, 2005.
- [73] VF Kovalev, KI Popov, V Yu Bychenkov, and W Rozmus. Laser triggered coulomb explosion of nanoscale symmetric targets. *Physics of plasmas*, 14(5):053103, 2007.
- [74] Matthew R. Edwards and Pierre Michel. Plasma transmission gratings for compression of high-intensity laser pulses. *Phys. Rev. Applied*, 18:024026, Aug 2022.
- [75] RK Kirkwood, PL Poole, DH Kalantar, TD Chapman, SC Wilks, MR Edwards, DP Turnbull, P Michel, L Divol, NJ Fisch, et al. Production of high fluence laser beams using ion wave plasma optics. *Applied Physics Letters*, 120(20):200501, 2022.
- [76] M. R. Edwards, V. R. Munirov, A. Singh, N. M. Fasano, E. Kur, N. Lemos, J. M. Mikhailova, J. S. Wurtele, and P. Michel. Holographic plasma lenses. *Phys. Rev. Lett.*, 128:065003, Feb 2022.
- [77] H Peng, J-R Marquès, L Lancia, François Amiranoff, RL Berger, S Weber, and C Riconda. Plasma optics in the context of high intensity lasers. *Matter and Radiation at Extremes*, 4(6):065401, 2019.
- [78] B Dromey, S Kar, M Zepf, and P Foster. The plasma mirror—a subpicosecond optical switch for ultrahigh power lasers. *Review of Scientific Instruments*, 75(3):645–649, 2004.
- [79] Cédric Thauray, Fabien Quere, J-P Geindre, Anna Levy, Tiberio Ceccotti, P Monot, Michel Bougeard, F Réau, P d’Oliveira, Patrick Audebert, et al.

Plasma mirrors for ultrahigh-intensity optics. *Nature Physics*, 3(6):424–429, 2007.

- [80] F Dollar, T Matsuoka, GM Petrov, AGR Thomas, SS Bulanov, V Chvykov, J Davis, G Kalinchenko, C McGuffey, L Willingale, et al. Control of energy spread and dark current in proton and ion beams generated in high-contrast laser solid interactions. *Physical Review Letters*, 107(6):065003, 2011.
- [81] Leonida A Gizzi, Elisabetta Boella, Luca Labate, Federica Baffigi, Pablo J Bilbao, Fernando Brandi, Gabriele Cristoforetti, Alberto Fazzi, Lorenzo Fulgentini, Dario Giove, et al. Enhanced laser-driven proton acceleration via improved fast electron heating in a controlled pre-plasma. *Scientific Reports*, 11(1):1–9, 2021.
- [82] RX Bai, CT Zhou, TW Huang, K Jiang, LB Ju, R Li, H Peng, MY Yu, B Qiao, SC Ruan, et al. Enhanced proton acceleration using split intense femtosecond laser pulses. *Plasma Physics and Controlled Fusion*, 63(8):085007, 2021.
- [83] K Markey, P McKenna, CM Brenner, DC Carroll, MM Günther, K Harres, S Kar, K Lancaster, F Nürnberg, MN Quinn, et al. Spectral enhancement in the double pulse regime of laser proton acceleration. *Physical review letters*, 105(19):195008, 2010.
- [84] KA Flippo, E d’Humières, SA Gaillard, J Rassuchine, DC Gautier, M Schollmeier, F Nürnberg, JL Kline, J Adams, B Albright, et al. Increased efficiency of short-pulse laser-generated proton beams from novel flat-top cone targets. *Physics of Plasmas*, 15(5):056709, 2008.
- [85] WJ Ma, I Jong Kim, JQ Yu, Il Woo Choi, PK Singh, Hwang Woon Lee, Jae Hee Sung, Seong Ku Lee, C Lin, Q Liao, et al. Laser acceleration of highly energetic carbon ions using a double-layer target composed of slightly underdense plasma and ultrathin foil. *Physical review letters*, 122(1):014803, 2019.

- [86] Peter Hilz, TM Ostermayr, A Huebl, V Bagnoud, B Borm, M Bussmann, M Gallei, J Gebhard, D Haffa, J Hartmann, et al. Isolated proton bunch acceleration by a petawatt laser pulse. *Nature communications*, 9(1):1–9, 2018.
- [87] Simon Vallières, Martina Salvadori, Alexander Permogorov, Giada Cantono, Kristoffer Svendsen, Z Chen, S Sun, Fabrizio Consoli, E d’Humières, C-G Wahlström, et al. Enhanced laser-driven proton acceleration using nanowire targets. *Scientific Reports*, 11(1):1–11, 2021.
- [88] S Buffechoux, J Psikal, M Nakatsutsumi, L Romagnani, A Andreev, K Zeil, M Amin, P Antici, T Burris-Mog, A Compant-La-Fontaine, et al. Hot electrons transverse refluxing in ultraintense laser-solid interactions. *Physical review letters*, 105(1):015005, 2010.
- [89] O Tresca, DC Carroll, XH Yuan, B Aurand, V Bagnoud, CM Brenner, M Coury, J Fils, RJ Gray, T Kühl, et al. Controlling the properties of ultraintense laser–proton sources using transverse refluxing of hot electrons in shaped mass-limited targets. *Plasma physics and controlled fusion*, 53(10):105008, 2011.
- [90] Joseph Snyder, LL Ji, and KU Akli. Enhancement of laser intensity and proton acceleration using micro-tube plasma lens targets. *Physics of plasmas*, 23(12):123122, 2016.
- [91] Yue Chao, Lihua Cao, Chunyang Zheng, Zhanjun Liu, and Xiantu He. Enhanced proton acceleration from laser interaction with a tailored nanowire target. *Applied Sciences*, 12(3):1153, 2022.
- [92] Min Chen, Alexander Pukhov, TP Yu, and ZM Sheng. Enhanced collimated gev monoenergetic ion acceleration from a shaped foil target irradiated by a circularly polarized laser pulse. *Physical review letters*, 103(2):024801, 2009.

- [93] D Neely, P Foster, A Robinson, Filip Lindau, Olle Lundh, Anders Persson, C-G Wahlström, and P McKenna. Enhanced proton beams from ultrathin targets driven by high contrast laser pulses. *Applied Physics Letters*, 89(2):021502, 2006.
- [94] J Itatani, J Faure, M Nantel, G Mourou, and S Watanabe. Suppression of the amplified spontaneous emission in chirped-pulse-amplification lasers by clean high-energy seed-pulse injection. *Optics Communications*, 148(1-3):70–74, 1998.
- [95] Chris Hooker, Yunxin Tang, Oleg Chekhlov, John Collier, Edwin Divall, Klaus Ertel, Steve Hawkes, Bryn Parry, and PP Rajeev. Improving coherent contrast of petawatt laser pulses. *Optics express*, 19(3):2193–2203, 2011.
- [96] Jin Woo Yoon, Cheonha Jeon, Junghoon Shin, Seong Ku Lee, Hwang Woon Lee, Il Woo Choi, Hyung Taek Kim, Jae Hee Sung, and Chang Hee Nam. Achieving the laser intensity of 5.5×10^{22} w/cm² with a wavefront-corrected multi-pw laser. *Optics express*, 27(15):20412–20420, 2019.
- [97] LP Ramirez, Dimitris N Papadopoulos, A Pellegrina, Patrick Georges, Frédéric Druon, P Monot, A Ricci, A Jullien, X Chen, Jean-Philippe Rousseau, et al. Efficient cross polarized wave generation for compact, energy-scalable, ultrashort laser sources. *Optics express*, 19(1):93–98, 2011.
- [98] U Griebner, S Rivier, V Petrov, M Zorn, G Erbert, M Weyers, X Mateos, M Aguiló, J Massons, and F Díaz. Passively mode-locked yb: Klu (wo 4) 2 oscillators. *Optics Express*, 13(9):3465–3470, 2005.
- [99] C Rödel, M Heyer, M Behmke, M Kübel, O Jäckel, W Ziegler, D Ehrt, MC Kaluza, and GG Paulus. High repetition rate plasma mirror for temporal contrast enhancement of terawatt femtosecond laser pulses by three orders of magnitude. *Applied Physics B*, 103(2):295–302, 2011.

- [100] Anna Lévy, Tiberio Ceccotti, Pascal D'Oliveira, Fabrice Réau, Michel Perdrix, Fabien Quéré, Pascal Monot, Michel Bougeard, Hervé Lagadec, Philippe Martin, et al. Double plasma mirror for ultrahigh temporal contrast ultraintense laser pulses. *Optics letters*, 32(3):310–312, 2007.
- [101] Gunther Horst Kassier, K Haupt, N Erasmus, EG Rohwer, HM Von Bergmann, H Schwoerer, Sergio MM Coelho, and Francois Danie Auret. A compact streak camera for 150 fs time resolved measurement of bright pulses in ultrafast electron diffraction. *Review of Scientific Instruments*, 81(10):105103, 2010.
- [102] Peng Wang, Jinyang Liang, and Lihong V Wang. Single-shot ultrafast imaging attaining 70 trillion frames per second. *Nature communications*, 11(1):1–9, 2020.
- [103] Bao-Liang Qian and Hani E Elsayed-Ali. Electron pulse broadening due to space charge effects in a photoelectron gun for electron diffraction and streak camera systems. *Journal of applied physics*, 91(1):462–468, 2002.
- [104] Jerome M. Auerbach and Victor P. Karpenko. Serrated-aperture apodizers for high-energy laser systems. *Appl. Opt.*, 33(15):3179–3183, May 1994.
- [105] DM Pennington, CG Brown, TE Cowan, SP Hatchett, E Henry, S Herman, M Kartz, M Key, J Koch, AJ MacKinnon, et al. Petawatt laser system and experiments. *IEEE Journal of Selected Topics in Quantum Electronics*, 6(4):676–688, 2000.
- [106] Patrick K Rambo, Ian C Smith, John L Porter, Michael J Hurst, C Shane Speas, Richard G Adams, Antonio J Garcia, Ellis Dawson, Benjamin D Thurston, Colleen Wakefield, et al. Z-beamlet: a multikilojoule, terawatt-class laser system. *Applied optics*, 44(12):2421–2430, 2005.
- [107] Irina Sizova, Timofey Moskalev, and Leonid Mikheev. Laser beam shaping with circular serrated apertures. i. spatial filtering. *Applied optics*, 58(18):4905–4909, 2019.

- [108] YX Zhang, S Rykovanov, Mingyuan Shi, CL Zhong, XT He, B Qiao, and M Zepf. Giant isolated attosecond pulses from two-color laser-plasma interactions. *Physical Review Letters*, 124(11):114802, 2020.
- [109] J Szerypo, W Ma, G Bothmann, D Hahner, M Haug, P Hilz, Ch Kreuzer, R Lange, S Seufferling, M Speicher, et al. Target fabrication for laser-ion acceleration research at the technological laboratory of the lmu munich. *Matter and Radiation at Extremes*, 4(3):035201, 2019.
- [110] Wenjun Ma, V Kh Liechtenstein, J Szerypo, D Jung, P Hilz, BM Hegelich, HJ Maier, Jörg Schreiber, and Dietrich Habs. Preparation of self-supporting diamond-like carbon nanofoils with thickness less than 5 nm for laser-driven ion acceleration. *Nuclear Instruments and Methods in Physics Research Section A: Accelerators, Spectrometers, Detectors and Associated Equipment*, 655(1):53–56, 2011.
- [111] Edwin Davison and William Colquhoun. Ultrathin formvar support films for transmission electron microscopy. *Journal of electron microscopy technique*, 2(1):35–43, 1985.
- [112] Bastian Aurand, Bentsian Elkin, Lars-Oliver Heim, Bettina Lommel, Birgit Kindler, Marilena Tomut, Christian Rödel, Stephan Kuschel, Oliver Jäckel, Jakob Barz, et al. Preparation and characterization of nanometer-thin free-standing polymer foils for laser-ion acceleration. *Journal of Polymer Science Part B: Polymer Physics*, 51(18):1355–1360, 2013.
- [113] Eric Auchter, Justin Marquez, Garrison Stevens, Rebecca Silva, Quinn McCulloch, Quintessa Guengerich, Andrew Blair, Sebastian Litchfield, Nan Li, Chris Sheehan, et al. Ultra-thin and strong formvar-based membranes with controlled porosity for micro-and nano-scale systems. *Nanotechnology*, 29(21):215712, 2018.
- [114] Alan D McNaught, Andrew Wilkinson, et al. *Compendium of chemical terminology*, volume 1669. Blackwell Science Oxford, 1997.

- [115] RM Wood. Laser induced damage thresholds and laser safety levels. do the units of measurement matter? *Optics & Laser Technology*, 29(8):517–522, 1998.
- [116] Roger M Wood. *Laser-induced damage of optical materials*. CRC Press, 2003.
- [117] D Vouagner, Cs Beleznai, JP Girardeau-Montaut, C Templier, and H Gonnord. A new method to determine laser damage threshold for thin diamond-like carbon films on silicon. *Diamond and related materials*, 9(3-6):786–791, 2000.
- [118] Dahui Wang, Wenjun Ma, Jianhui Bin, Klaus Alinger, Yinren Shou, Pengjie Wang, Jianbo Liu, Jungao Zhu, Zhengxuan Cao, Zhusong Mei, et al. Single-shot laser-induced damage threshold of free-standing nanometer-thin diamond-like carbon foils. *Nuclear Instruments and Methods in Physics Research Section B: Beam Interactions with Materials and Atoms*, 436:18–21, 2018.
- [119] APL Robinson, M Zepf, S Kar, RG Evans, and C Bellei. Radiation pressure acceleration of thin foils with circularly polarized laser pulses. *New journal of Physics*, 10(1):013021, 2008.
- [120] T Esirkepov, Marco Borghesi, SV Bulanov, G Mourou, and T Tajima. Highly efficient relativistic-ion generation in the laser-piston regime. *Physical review letters*, 92(17):175003, 2004.
- [121] Y Sentoku, TE Cowan, A Kemp, and H Ruhl. High energy proton acceleration in interaction of short laser pulse with dense plasma target. *Physics of plasmas*, 10(5):2009–2015, 2003.
- [122] Natsumi Iwata, Kunioki Mima, Yasuhiko Sentoku, Akifumi Yogo, Hideo Nagatomo, Hiroaki Nishimura, and Hiroshi Azechi. Fast ion acceleration in a foil plasma heated by a multi-picosecond high intensity laser. *Physics of Plasmas*, 24(7):073111, 2017.

- [123] F Dollar, C Zulick, AGR Thomas, V Chvykov, J Davis, G Kalinchenko, T Matsuoka, C McGuffey, GM Petrov, L Willingale, et al. Finite spot effects on radiation pressure acceleration from intense high-contrast laser interactions with thin targets. *Physical review letters*, 108(17):175005, 2012.
- [124] Dong Wu, B Qiao, C McGuffey, XT He, and FN Beg. Generation of high-energy mono-energetic heavy ion beams by radiation pressure acceleration of ultra-intense laser pulses. *Physics of Plasmas*, 21(12):123118, 2014.
- [125] KWD Ledingham, P McKenna, T McCanny, S Shimizu, JM Yang, L Robson, Jamal Zweit, James M Gillies, J Bailey, GN Chimon, et al. High power laser production of short-lived isotopes for positron emission tomography. *Journal of Physics D: Applied Physics*, 37(16):2341, 2004.
- [126] P McKenna, KWD Ledingham, I Spencer, T McCany, RP Singhal, C Ziener, PS Foster, EJ Divall, CJ Hooker, D Neely, et al. Characterization of multi-terawatt laser-solid interactions for proton acceleration. *Review of scientific instruments*, 73(12):4176–4184, 2002.
- [127] Y Oishi, T Nayuki, T Fujii, Y Takizawa, X Wang, T Yamazaki, K Nemoto, T Kayoiji, T Sekiya, K Horioka, et al. Dependence on laser intensity and pulse duration in proton acceleration by irradiation of ultrashort laser pulses on a cu foil target. *Physics of plasmas*, 12(7):073102, 2005.
- [128] N. P. Dover, M. Nishiuchi, H. Sakaki, Ko. Kondo, M. A. Alkhimova, A. Ya. Faenov, M. Hata, N. Iwata, H. Kiriya, J. K. Koga, T. Miyahara, T. A. Pikuz, A. S. Pirozhkov, A. Sagisaka, Y. Sentoku, Y. Watanabe, M. Kando, and K. Kondo. Effect of small focus on electron heating and proton acceleration in ultrarelativistic laser-solid interactions. *Phys. Rev. Lett.*, 124:084802, Feb 2020.
- [129] K Zeil, SD Kraft, S Bock, M Bussmann, TE Cowan, T Kluge, J Metzkes, T Richter, R Sauerbrey, and U Schramm. The scaling of proton ener-

gies in ultrashort pulse laser plasma acceleration. *New Journal of Physics*, 12(4):045015, 2010.

- [130] T D Arber, K Bennett, C S Brady, A Lawrence-Douglas, M G Ramsay, N J Sircombe, P Gillies, R G Evans, H Schmitz, A R Bell, and C P Ridgers. Contemporary particle-in-cell approach to laser-plasma modelling. *Plasma Physics and Controlled Fusion*, 57(11):1–26, November 2015.
- [131] Tong-Pu Yu, Alexander Pukhov, Gennady Shvets, and Min Chen. Stable laser -driven proton beam acceleration from a two-ion-species ultrathin foil. *Physical review letters*, 105(6):065002, 2010.
- [132] APL Robinson, DH Kwon, and K Lancaster. Hole-boring radiation pressure acceleration with two ion species. *Plasma Physics and Controlled Fusion*, 51(9):095006, 2009.
- [133] Qingcao Liu, Meng Liu, Tongpu Yu, Pengji Ding, Zuoye Liu, Shaohua Sun, Xiaoliang Liu, Xing Lu, Zeqin Guo, and Bitao Hu. Effect of target composition on proton acceleration in ultraintense laser-thin foil interaction. *Physics of Plasmas*, 19(9):093108, 2012.
- [134] Tung-Chang Liu, Xi Shao, Chuan-Sheng Liu, Minqing He, Bengt Eliasson, Vipin Tripathi, Jao-Jang Su, Jyhpyng Wang, and Shih-Hung Chen. Generation of quasi-monoenergetic protons from thin multi-ion foils by a combination of laser radiation pressure acceleration and shielded coulomb repulsion. *New Journal of Physics*, 15(2):025026, 2013.
- [135] Xue-Ren Hong, Bai-Song Xie, Shan Zhang, Hai-Cheng Wu, Aimierding Aimidula, Xue-Yan Zhao, and Ming-Ping Liu. High quality ion acceleration from a double-layer target dominated by the radiation pressure of a transversely gaussian laser pulse. *Physics of Plasmas*, 17(10):103107, 2010.
- [136] B Liu, Jürgen Meyer-ter Vehn, KU Bamberg, WJ Ma, J Liu, XT He, XQ Yan, and H Ruhl. Ion wave breaking acceleration. *Physical Review Accelerators and*

Beams, 19(7):073401, 2016.

- [137] B Liu, Jürgen Meyer-ter Vehn, and H Ruhl. Self-trapping and acceleration of ions in laser-driven relativistically transparent plasma. *Physics of Plasmas*, 25(10):103117, 2018.
- [138] William Kruer. *The physics of laser plasma interactions*. CRC Press, 2019.
- [139] OL Landen, DG Stearns, and EM Campbell. Measurement of the expansion of picosecond laser-produced plasmas using resonance absorption profile spectroscopy. *Physical review letters*, 63(14):1475, 1989.
- [140] R Ramis, K Eidmann, J Meyer-ter Vehn, and S Hüller. Multi-fs—a computer code for laser–plasma interaction in the femtosecond regime. *Computer Physics Communications*, 183(3):637–655, 2012.
- [141] Je Hoi Mun, Cheonha Jeon, and Chang-Mo Ryu. Path integral formulation of light propagation in a static collisionless plasma, and its application to dynamic plasma. *Optics Express*, 28(5):6417–6432, 2020.
- [142] M Capitelli, A Casavola, G Colonna, and A De Giacomo. Laser-induced plasma expansion: theoretical and experimental aspects. *Spectrochimica Acta Part B: Atomic Spectroscopy*, 59(3):271–289, 2004.
- [143] ML Zhou, JH Bin, D Haffa, XQ Yan, and J Schreiber. The impact of femtosecond pre-pulses on nanometer thin foils for laser-ion acceleration. *Plasma Physics and Controlled Fusion*, 59(5):055020, 2017.
- [144] Mingyuan Shi, Shaochuan Huang, Wei Xi, Zuoye Liu, Hongchuan Du, Baowei Ding, and Bitao Hu. High resolution coulomb explosion spectra and angular distributions of fragment ions of $n = 2$ in a femtosecond laser field. *Applied Physics B*, 123:1–7, 2017.

Appendix: Multi-stage Al Filter

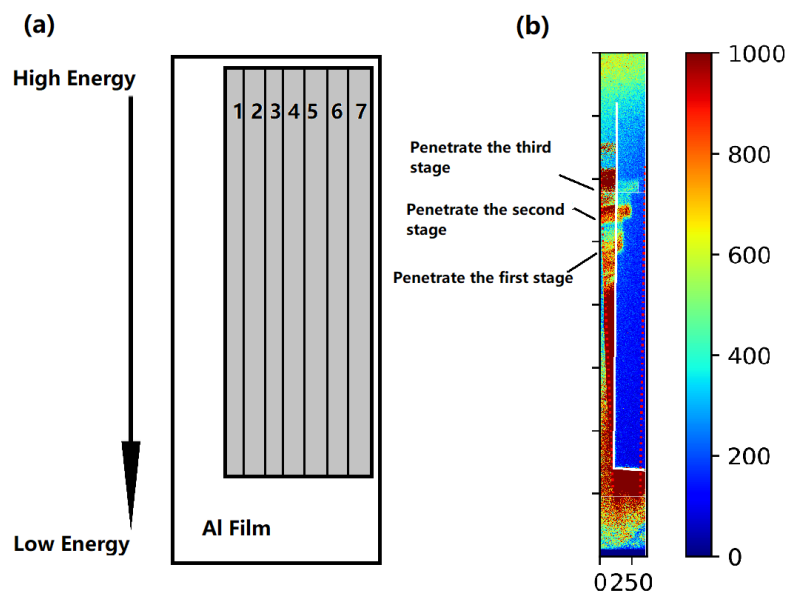


Fig. 1: (a) Multi-stage Al filter configuration, the numbers represent the number of stages, corresponding to different thicknesses of Al. (b) The actual effect in the experiment. The white line represents the edge of the multi-stage Al filter. In this case, the protons penetrate beyond the third stage, the cut-off energy is 19 MeV.

In the experiment, the IP is wrapped with a 30 μm thick Al film, and a multi-stage Al filter is placed in front of it to quickly diagnose the proton beam's energy and ensure that the proton signal is free from the interference of the heavy ions. The configuration of multi-stage filter is shown in Fig.1. (a) the multi-stage Al filter configuration, and (b) the actual effect in the experiment. The numbers represent the number of stages, corresponding to different thicknesses of Al. The thickness and corresponding proton energy are shown in the table below. Heavy ions and protons are simultaneously deflected by the magnets, but only protons pass through

the corresponding the multi-stage Al filter. Namely, the signal on the multi-stage Al filter is generated for protons. Only the places Al film covers are mixed with multiple ions.

Stage Number	Thickness (mm)	Proton Energy (MeV)
1	0.4	8
2	0.8	11.5
3	1.53	17
4	2.09	20
5	3.10	25
6	4.90	31
7	7.18	40

Tab. 1: The thickness corresponds to the number of multi-stage aluminum filters and the energy required for the proton beam to penetrate this thickness of aluminum.

Appendix: Raw Proton Spectrum

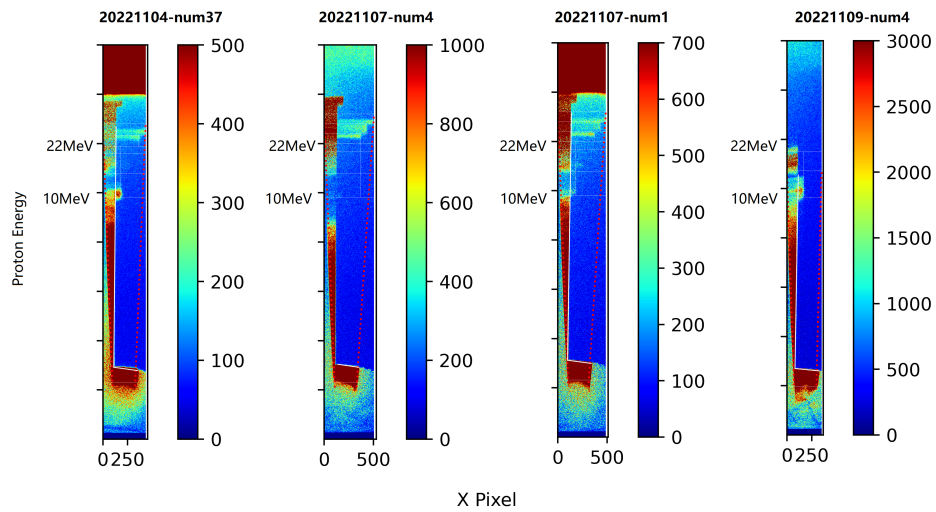


Fig. 1: The raw energy spectrum of circularly polarized light incident on the thin target. From the left to the right are 10 nm, 40 nm, 50 nm, and 90 nm thickness targets, respectively.

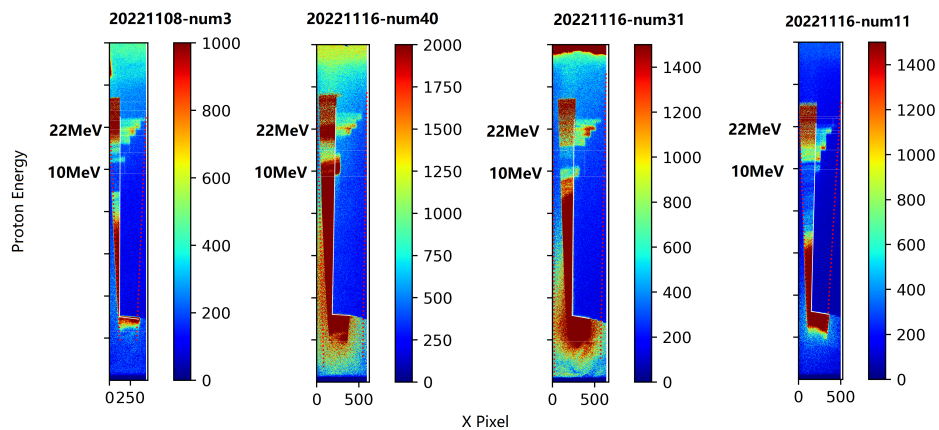


Fig. 2: The raw energy spectrum of circularly polarized light incident on the 40 nm target. The laser intensities are around num3: $2 \times 10^{21} \text{W/cm}^2$, num40: $1.7 \times 10^{21} \text{W/cm}^2$, num31: $1.4 \times 10^{21} \text{W/cm}^2$, and num11: $1.1 \times 10^{21} \text{W/cm}^2$, respectively.

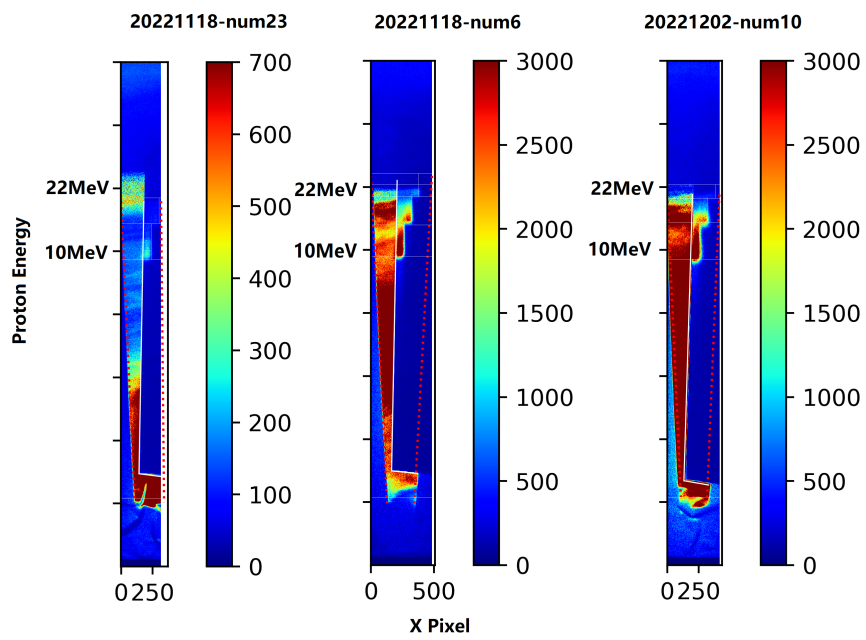


Fig. 3: Raw energy spectrum of linearly polarized light incident on the thin target. From the left to the right are 10 nm, 40 nm and 90 nm thickness targets, respectively.

Appendix: Helmholtz and Fresnel equations

In the extreme situation, the results of the Helmholtz equations should be close to that of the Fresnel equations when the plasma scale length is extremely short. From this perspective, the accuracy of the Helmholtz solver can also be verified. The Fresnel equations describe the reflection and transmission of electromagnetic radiation, which are associated with the polarization of the incident radiation. The Fresnel equations are determined by solving the wave equation across the dielectric media interface for the p- and s- components of the electromagnetic radiation independently, and they are usually written as:

$$R_s = \left| \frac{n_2 \cos \theta_i - n_1 \cos \theta_t}{n_2 \cos \theta_i + n_1 \cos \theta_t} \right|^2 \text{ and } R_p = \left| \frac{n_2 \cos \theta_t - n_1 \cos \theta_i}{n_2 \cos \theta_t + n_1 \cos \theta_i} \right|^2, \quad (1)$$

here the corresponding refractive indexes of media 1 and 2 are n_1 and n_2 , respectively. Considering the response of the light that passes through a medium (e.g., under critical density plasma), some part of it will always be attenuated. This can be conveniently taken into account by defining a complex refractive index,

$$\tilde{n} = n + i \cdot k, \quad (2)$$

where n and k are the real and the imaginary part of the complex refractive index, respectively. The real part n is the refractive index and indicates the phase velocity, while the imaginary part k is called the attenuation coefficient and expresses the

attenuation or damping of the light. Combining the formulas 1 and the complex refractive index 2, one can get the complex Fresnel equations,

$$R_s = \left| \frac{(n_2 + i \cdot k_2) \cos \theta_i - n_1 \cos \theta_t}{(n_2 + i \cdot k_2) \cos \theta_i + n_1 \cos \theta_t} \right|^2 \quad (3)$$

$$R_p = \left| \frac{(n_2 + i \cdot k_2) \cos \theta_t - n_1 \cos \theta_i}{(n_2 + i \cdot k_2) \cos \theta_t + n_1 \cos \theta_i} \right|^2 \quad (4)$$

Here, assuming the first medium is an ideal dielectric of refractive index n_1 (e.g., vacuum) and the second is a real medium with a complex refractive index. The Fresnel equations describe light's reflection and transmission behavior when incident on an interface between different optical media. However, in the limit, the plasma scale length closes to zero, and the plasma density is a perfect step function. In this case, the Fresnel equations of metal optics can be compared with the Helmholtz wave equations. After some algebra, separating the real part of the complex terms, one can evaluate the angular dependence of the absorbed fraction between the Fresnel equations and the Helmholtz equations as shown in Fig.1. On the contrary,

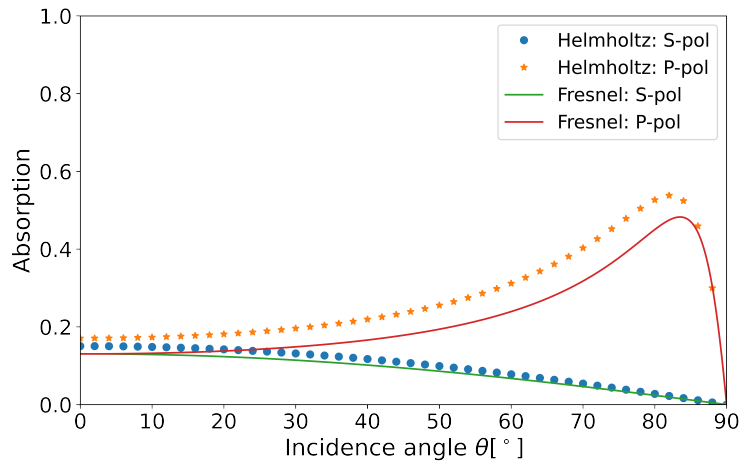


Fig. 1: Comparison of the angular dependence of the absorbed fraction between the Fresnel equations and the Helmholtz equations.

for a long and slowly varying plasma profile, the numerical results tend towards an analytic solution for resonance absorption. One can use Wentzel-Kramers-Brillouin (WKB) approximation for s-polarized light[138]. The absorption coefficient in this limit is written as[138]

$$\eta_{WKB} = 1 - \exp\left(\frac{-8\nu_{ei}L}{3c} \cos^3\theta\right) \quad (5)$$

where L is the density gradient of plasma and θ is incident angle.

Publications by the Author

1. B. Liu, **M. Shi**, M. Zepf, B. Lei, and D. Seipt. "Accelerating Ions by Crossing Two Ultraintense Lasers in a Near-Critical Relativistically Transparent Plasma." *Physical Review Letters* 129, no. 27 (2022): 274801.
2. B. Lei, D. Seipt, **M. Shi**, B. Liu, J. Wang, M. Zepf, and S. G. Rykovanov. "Relativistic modified Bessel-Gaussian beam generated from plasma-based beam braiding." *Physical Review A* 104, no. 2 (2021): L021501.
3. Y. Zhang, S. Rykovanov, **M. Shi**, C. Zhong, X. He, B. Qiao, and M. Zepf. "Giant isolated attosecond pulses from two-color laser-plasma interactions." *Physical Review Letters* 124, no. 11 (2020): 114802.

Acknowledgements

I would like to express my deep appreciation to everyone who has contributed to my doctoral stage.

First and foremost, I am deeply grateful to **Prof. Dr. Matt Zepf** for his unwavering guidance, support, and encouragement throughout my research journey. He not only gave me the opportunity to complete my doctoral degree in Germany but also left a lasting impression on my life. His expertise, insights, and constructive feedback were invaluable in shaping my research and helping me overcome numerous challenges in physics. Thanks for giving me the opportunity to do experiments in different large laboratories, which allowed me to expand my horizons and increase my experimental skills.

I want to express my sincere gratitude to my supervisor, **Prof. Dr. Malte C. Kaluza**, for invaluable support and guidance throughout my research project. His expertise and constructive feedback have been instrumental in shaping the direction and focus of my work. I am grateful for his willingness to share time and knowledge with me and for our insightful discussions.

I would like to thank the members of JETi200, **Dr. Alexander Sävert** and **Georg Schäfer**. Their excellent working ability ensures the stable operation of the laser, and their expertise and intellectual generosity have enriched my research and broadened my perspectives.

I would like to thank my colleagues in the experimental group, **Dr. Peter Hilz**, **Dr. Julia Braenzel** and **Israa Salaheldin**, for their camaraderie, support, and motivation. I have benefited a lot from the discussion together. The experience of working together has become my fondest memory. Thanks for your full support during the experiment.

I would like to thank, **Burgard Beleites** and **Falk Ronneberger**. Their profound expertise and generous knowledge-sharing have elevated my research and expanded my horizons. Thanks for your full support during the JETi40 experiment.

I want to thank my simulation group colleagues, **Dr. Bin Liu**, **Dr. Bifeng Lei** and **Dr. Daniel Seipt**, for helping me to answer PIC simulation problems and to predict the experimental results.

I am grateful to **Dr. Lu Li** for introducing me to the research field of High-order harmonic generation from solid targets and for his invaluable guidance and insightful discussions during experiments.

I want to thank **Dr. Yuxue Zhang** and **Dr. Sergey Rykovanov**, for helping me to me build the simulation platform and answer the simulation questions.

Many thanks go to all my former colleagues in Lanzhou University. I would like to acknowledge my supervisor **Prof. Dr. Bitao Hu**, who gave me important life advice and scientific research planning. I want to thank **Prof. Dr. Baowei Ding** for his great support during my PhD stage. I want to thank **Prof. Dr. Zuoye Liu** for his great support in the experiment.

Last but not least, thanks to my parents for their support from beginning to end. Everything will get better. The challenges posed by the Covid-19 pandemic, I am grateful for the unwavering trust and support of my girlfriend, **Dr. Qingyu Gao**, whom I haven't seen in four years. I want to express my heartfelt gratitude to her. Last but not least, thankful for my orange cat, **Lucky**, who greets me at the door every day.

As I stand at the end of my doctoral journey, reviewing my 25-year study path. I am struck by the overwhelming sense of awe that comes with infinite knowledge, humbled by my insignificance in the face of it all, and grieving the transience of life, knowing that "Flowers will bloom again, but people will never be young again". There are not many six years in one's life. Jena, Germany has already become my second hometown, "see you later!".

Mingyuan Shi

Jena, 6, June, 2023

Ehrenwörtliche Erklärung

Ich erkläre hiermit ehrenwörtlich, dass ich die vorliegende Arbeit selbständig, ohne unzulässige Hilfe Dritter und ohne Benutzung anderer als der angegebenen Hilfsmittel und Literatur angefertigt habe. Die aus anderen Quellen direkt oder indirekt übernommenen Daten und Konzepte sind unter Angabe der Quelle gekennzeichnet. Bei der Auswahl und Auswertung folgenden Materials haben mir die nachstehend aufgeführten Personen in der jeweils beschriebenen Weise unentgeltlich geholfen:

1. Diese Arbeit wurde bisher an keiner anderen Institution für einen Abschluss oder eine Prüfung eingereicht.
2. Diese Arbeiten wurden unter der Aufsicht des Supervisors durchgeführt und innerhalb der festgelegten Frist abgeschlossen.
3. Die in dieser Arbeit präsentierten Ergebnisse und Schlussfolgerungen sind meine eigenen und wurden von keiner externen Quelle beeinflusst.
4. Alle in dieser Arbeit verwendeten Quellen wurden im Text und im Literaturverzeichnis ordnungsgemäß angegeben und zitiert.
5. Ich habe keine Daten, Ergebnisse oder Ideen, die geistiges Eigentum einer anderen Person oder Institution sind, ohne deren ausdrückliche Genehmigung verwendet.
6. Ich habe keine in dieser Arbeit enthaltenen Daten oder Informationen gefälscht.
7. Mir ist bekannt, dass jeder Verstoß gegen die vorstehenden Erklärungen zur Annullierung meines Abschlusses und anderen rechtlichen Konsequenzen führen kann.

Weitere Personen waren an der inhaltlich-materiellen Erstellung der vorliegenden Arbeit nicht beteiligt. Insbesondere habe ich hierfür nicht die entgeltliche Hilfe von

Vermittlungsbzw. Beratungsdiensten (Promotionsberater oder andere Personen) in Anspruch genommen.

Niemand hat von mir unmittelbar oder mittelbar geldwerte Leistungen für Arbeiten erhalten, die im Zusammenhang mit dem Inhalt der vorgelegten Dissertation stehen.

Die Arbeit wurde bisher weder im In- noch im Ausland in gleicher oder ähnlicher Form einer anderen Prüfungsbehörde vorgelegt.

Die geltende Promotionsordnung der Physikalisch-Astronomischen Fakultät ist mir bekannt.

Ich versichere ehrenwörtlich, dass ich nach bestem Wissen die reine Wahrheit gesagt und nichts verschwiegen habe.

Mingyuan Shi

Jena, 6, June, 2023